The Dissertation Committee for Carl Joseph Siemon
certifies that this is the approved version of the following dissertation:

Interaction of Charged Particle Beams with Plasmas

Committee:

Herbert Berk, Supervisor

Swadesh Mahajan, Co-Supervisor

C. Wendell Horton, Jr.

Richard Fitzpatrick

Pawan Kumar

Interaction of Charged Particle Beams with Plasmas

by

Carl Joseph Siemon, B.S.

DISSERTATION

Presented to the Faculty of the Graduate School of

The University of Texas at Austin

in Partial Fulfillment

of the Requirements

for the Degree of

DOCTOR OF PHILOSOPHY

THE UNIVERSITY OF TEXAS AT AUSTIN

December 2014

Acknowledgments

This thesis is dedicated to my hometown, Woodbury. I would like to thank my fellow graduate students and close friends Dan and Sohaib for their emotional support and illuminating discussions about physics throughout my time here at UT. I wish to thank my parents for their support and everything they have provided for me, especially for forcing me to learn classical piano in my youth. Funding for this work was provided by the US Department of Energy, US Department of Defense, and the University of Texas Physics Department. Supercomputing resources were provided by the Texas Advanced Computing Center.

Interaction of Charged Particle Beams with Plasmas

Publication No. _____

Carl Joseph Siemon, Ph.D.
The University of Texas at Austin, 2014

Supervisors: Herbert Berk
Swadesh Mahajan

This thesis focuses on the propagation of charged particle beams in plasmas, and is divided into two main parts. In the second chapter, a novel theoretical model for underdense electron beam propagation during the nonlinear stage of the resistive Weibel instability (WI) is presented and is used to calculate the stopping time of the beam. The model and supporting simulation results lead to the conclusion that the WI initially enhances beam deceleration but then reduces it when compared to a filamentation-suppressed beam (without WI), so that the overall stopping time of the beam is essentially unaffected by the instability. Using the theoretical model, a criterion is derived that determines when deceleration is no longer enhanced by the instability. We also demonstrate that exotic plasma return current distributions can be obtained within and outside of beam filaments that sharply contrast those observed in collisionless systems. For example, the plasma return current is reversed in selected areas.

In the next chapter, a new method for initiating the modulation instability (MI) of a proton beam in a proton driver plasma wakefield accelerator using a short laser pulse preceding the beam is presented. A diffracting laser pulse is used to produce a plasma wave that provides a seeding modulation of the proton bunch with the period equal to that of the plasma wave. Using the envelope description of the proton beam, this method of seeding the MI is analytically compared with the earlier suggested seeding technique that involves an abrupt truncation of the proton bunch. The full kinetic simulation of a realistic proton bunch is used to validate the analytic results. It is further used to demonstrate that a plasma density ramp placed in the early stages of the laser-seeded MI leads to its stabilization, resulting in sustained accelerating electric fields (of order several hundred MV/m) over long propagation distances (100-1000 m). The final chapter describes a harmonic expansion formalism that attempts to explain the post-linear stage of the MI. The formalism is developed first, and then several crippling problems with it are identified.

Table of Contents

Chapter 1

Introduction

1.1 Outline

Charged particle beam propagation through a background plasma occurs in a variety of physical systems and has many applications. Some examples include electron beam generated gamma ray bursts in astrophysical scenarios [1, 2, 3], free electron lasers used to create x-rays and high frequency electromagnetic radiation [4], suprathermal electron beams propagating through the sun's corona [5], and inertial fusion driven by ion beams [6]. In this thesis, we focus on two topics. The first is relativistic electron beam (REB) propagation through a high density deuterium-tritium plasma in the context of inertial confinement fusion (ICF). We describe the evolution of the transverse electromagnetic Weibel Instability within the REB in the presence of background plasma resistivity (characterized by plasma electron-ion collisions), which is an anticipated prevalent collective instability, and determine the effect of the instability on beam stopping. The second topic is proton-driven plasma wakefield acceleration using the proton beams generated at CERN's (European Centre for Particle Physics) Large Hadron Collider (LHC). Here, we model the so-called modulation instability within the proton driver, which is relied

upon to produce large accelerating gradients that lead to high 'witness' electron bunch energies ($\sim$ TeV).

1.2 Fast ignition via laser-generated relativistic electron beams

Inertial confinement fusion (ICF) has been a topic of intense research over the past decades. Throughout the 1950s and 1960s, Kidder, Colgate, and Nuckolls independently described various methods that use high-power lasers to illuminate a spherical deuterium and tritium (D-T) fuel mix, or 'target', over the target's surface to implode and ignite it [7] . In the 'direct drive' ICF approach envisioned by Kidder, a spherically symmetric pulse of laser light is focused directly onto the target, while in the 'indirect drive' approach envisioned by Colgate and Nuckolls, lasers are focused onto a metal cylinder, or 'hohlraum', which then radiates x-rays that heat the target. The heat generated by the driver causes the outer layer of the the target to explode outward, which causes the remaining target material to implode according to Newton's third law. The target's implosion leads to high densities (in some cases, orders of magnitude greater than solid density, $\sim$ 1000 g/cm^3) and temperatures of order KeV. Under these conditions, energetic alpha particles are created by fusion reactions, which further thermalize the surrounding plasma, leading to a chain-reaction known as 'thermonuclear burn' that produces many times the input energy.

More recently, the chirped laser pulse amplification [8] technique, which

generates high laser powers (>Terawatt) and intensities ($> 10^{18}$ W/cm^2), has led to a promising approach to ICF known as 'fast-ignition' (FI) [9], which consists of two main stages: first, D-T fuel is imploded via either direct or indirect drive, leading to a high density configuration; second, a relativistic electron beam (REB) created by the ponderomotive force of a secondary high-power/intensity laser propagates from the critical density surface to the high-density core, where it deposits its energy and 'ignites' the target. Figure 1.1 [9] shows a schematic diagram of this. The originally envisioned, more conventional approach to ICF utilizes only the first part of this scheme, which requires that the implosion produce both sufficiently high densities and temperatures for the target to ignite. By separating the compression and heating phases, FI significantly reduces the total input energy needed in comparison to the single stage approach, making it an attractive scheme to accomplish fusion [9].

The secondary laser and corresponding REB parameters required to ignite the D-T target in the FI scheme are determined by the target's size, 'disassembly time' (the amount of time it takes for a target with temperature $\sim$ KeV to thermally expand and disassemble), and energy transfer rates between the laser, electron beam, and plasma [9]. The REB heats mostly the plasma electrons via collisions due to their small mass, and the laser duration cannot be much smaller than the plasma electron-ion thermal equilibrium rate-otherwise, the heated electrons will cause the target to expand before the ions can be heated to fusion temperatures. Also, if the laser pulse is longer than

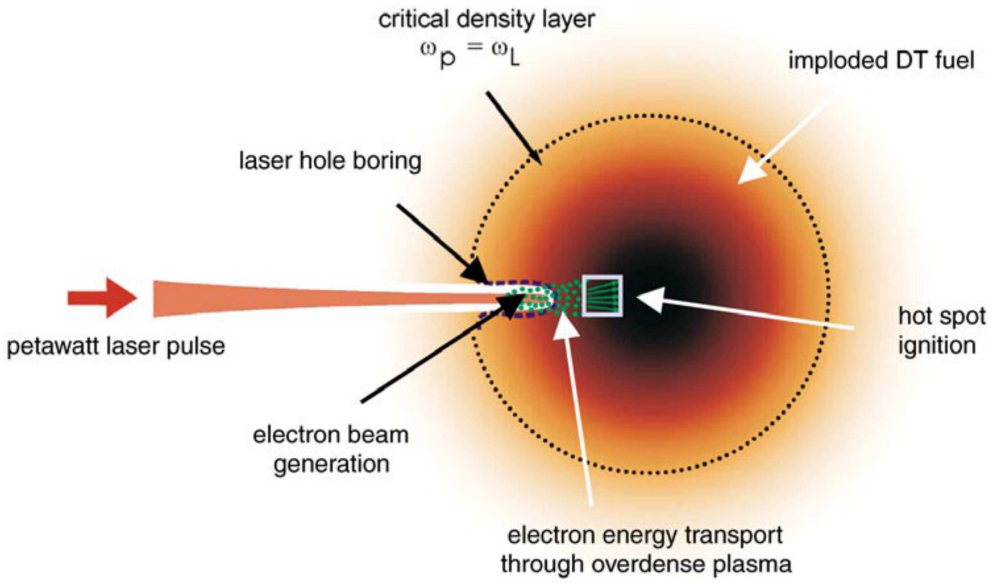

Figure 1.1: Schematic representation of fast ignition [9]. Fast ignition consists of two main stages: 1) D-T fuel is imploded via either direct or indirect drive, leading to a high density configuration; 2) a relativistic electron beam (REB) created by the ponderomotive force of a secondary high-power/intensity laser propagates from the critical density surface to the high-density core, where it deposits its energy and 'ignites' the target.

the disassembly time, then the target will break apart before the laser's energy can be deposited. To satisfy these conditions and heat a target with density $\rho = 300$ g/cm^3, radius $R = 10$ μm, and areal density $\sim .4$ g/cm^2 from temperature ~ 1 KeV to ~ 10 KeV, a $\gtrsim 3$ kJ laser with power $\sim 10^{14}$ W and intensity $\sim 10^{20}$ W/cm^2 is required. PIC simulations show that these laser parameters lead to $\sim$ MeV electron beams with $\sim$ MA currents and ~ 1 fs duration, which are expected to stop near the target's core.

Without collective instabilities, the expected dominant stopping mech-

anism for the REB is binary collisions with the plasma electrons near the target's core [9]. At densities greater than or comparable to solid density, many particles in the plasma interact simultaneously with a beam electron. To calculate the energy loss of a beam electron, this effect can be treated macroscopically by considering the dielectric response of the plasma to the particle [10]. For a very dense plasma with electrons that have a DeBroglie wavelength comparable to their typical separation distance, which is the case for a compressed FI target, the electrons' wavefunctions begin to overlap. In this case, electron degeneracy must be taken into account when computing the plasma's dielectric function. This is accomplished in Ref. [11], where a pseudoanalytic fit is found for their quantum stopping numerics:

$$-\frac{dE}{dx} = \frac{4\pi n_{p0} e^4}{mv^2} \log(\frac{2mc^2\gamma^2}{\hbar\omega_p}). \tag{1.1}$$

Here, $\frac{dE}{dx}$ is the rate at which work is done by the plasma on the REB propagating along the x axis with velocity $|\vec{v}| \approx c$ and kinetic energy $E = (\gamma - 1)mc^2$, where γ is the beam's relativistic Lorentz factor, $\omega_p \equiv \sqrt{\frac{4\pi e^2 n_{p0}}{m}}$ is the electron plasma frequency, e is fundamental charge, m is the electron mass, and n_{p0} is the quiescent plasma number density. The quantity $\frac{dE}{dx}$ is commonly termed the 'stopping power' of the beam. For >MeV electron beams, Eq. (1.1) yields the approximate stopping time [11]

$$\tau_c \sim \frac{m^2 c^3 \gamma(t=0)}{4\pi n_{p0} e^4 \log(\frac{2mc^2\gamma^2}{\hbar\omega_p})}. \tag{1.2}$$

Direct energy deposition of the REB into the target via REB-plasma collisions is not the only mechanism for it to stop within an FI target; collective

instabilities can also play a significant role in the REB's deceleration. These instabilities arise mainly through two effects: first, the electric current carried by the REB is quickly neutralized by an induced plasma return current [12], and the transverse repulsion between the counter-propagating currents leads to instabilities; second, portions of the REB towards the beam's head can excite density oscillations within the plasma that affect the REB's tail, which can lead to positive feedback and longitudinal/oblique instabilities within the REB. The latter effect is considered to play a less significant role for high energy REB's in FI because of two reasons: oblique instabilities are believed to saturate by beam electron trapping before a significant fraction of the beam's energy is removed [13, 14, 15]; and the REB's longitudinal length is much longer than the plasma wavelength so that it does not resonantly drive plasma oscillations, leading to small oscillation amplitudes.

In FI scenarios, the anti-parallel current repulsion between the REB and plasma return current leads to what is believed to be the most robust collective instability within the beam: the transverse electromagnetic Weibel Instability (WI). The WI leads to beam pinching and filamentation, beam and plasma heating, and the generation of strong magnetic fields [16, 17, 18, 19], which can take away energy from the beam's longitudinal motion. In outer coronal regions of the FI target that have lower temperature and density than the core, beam-plasma collisions are less dominant, and finite plasma resistivity (FPR) created by plasma electron-ion collisions can enhance the WI via transverse magnetic field diffusion. In this thesis, we investigate the effect of the WI in

the presence of FPR on beam stopping time without considering beam-plasma collisions, where Eq. (1.2) is used as a benchmark for comparison.

1.3 Proton driver plasma wakefield acceleration

The concept of the plasma-based accelerator was first proposed by Tajima and Dawson [20]. These accelerators aim to efficiently accelerate 'witness' electrons via a dynamically produced accelerating structure within the plasma. This structure is created by a 'driver' propagating close to the speed of light that excites plasma density oscillations behind it, known as Langmuir waves [21]. Langmuir waves result in considerable transverse and longitudinal electromagnetic fields, known as 'wakefields', that co-propagate with the driver. Electrons that are in phase with the accelerating portion of the wakefield can gain considerable energy from the driver, and in the past decade, monoenergetic electron beams with ~ 1 GeV have been reported [22, 23, 24, 25]. The driver is usually either an intense laser pulse [20, 26], a relativistic electron beam [27, 28, 30], or a relativistic positron beam [31]. Figure 1.2 displays a schematic representation of plasma wakefield acceleration [29].

Plasma-based accelerators are of interest due to the large electric fields supported by plasmas in comparison to those in conventional radio frequency (RF) accelerating structures. The electric fields in an RF accelerator can lead to 'RF breakdown' or arcing that degrades the accelerating structure [32], limiting the accelerating gradient to ~ 100 MV/m [33]. In a plasma-based accelerator, this problem is circumvented because the plasma is already 'electrically

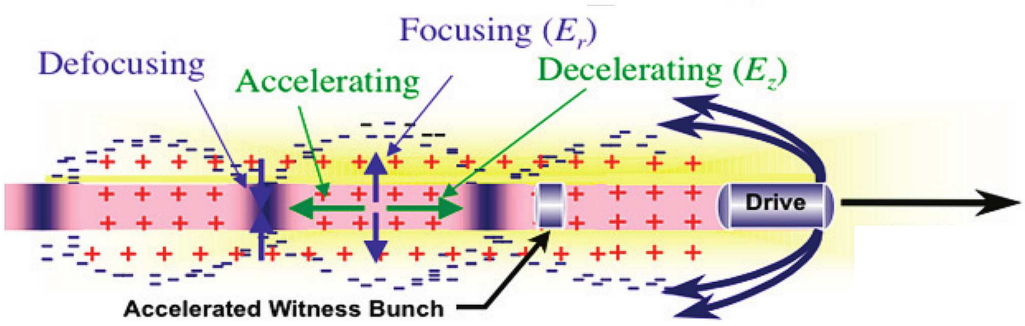

Figure 1.2: Schematic representation of plasma wakefield acceleration [29]. 'Drive' bunch (laser pulse, electron beam, positron bream, or proton beam) excites plasma density oscillations behind it, known as Langmuir waves [21]. Langmuir waves produce considerable transverse and longitudinal electromagnetic fields, known as 'wakefields', that co-propagate with the driver. 'Witness' electrons that are in phase with the accelerating portion of the wakefield can gain considerable energy from the driver.

broken', so that much larger fields can be supported. For example, plasmas with Langmuir waves that are oscillating near the 'wavebreaking' limit support electric fields of order $E \sim \frac{m_e \omega_p}{e}$, which is $E(V/cm) \approx \sqrt{n_{p0}(cm^{-3})} \sim 100$ GV/m for a plasma with density $n_{p0} = 10^{18}$ cm^{-3}- roughly three orders of magnitude greater than the maximum accelerating gradient supported by an RF accelerator. These large accelerating gradients make plasma-based accelerators attractive for the following applications due to the prospect of considerable size reduction and cost: colliders for high energy particle physics research [34, 35]; x-ray generation for materials and biological research [36]; and radiation therapy in oncology [37].

As mentioned above, charged particle beams may be used as a driver

for plasma based accelerators. For a particle driver, the maximum energy gain possible for the accelerated electrons is limited by the transformer ratio [38]:

$$R = \frac{E_{max}^{witness}}{E_{max}^{drive}} \leq 2 - \frac{N_{witness}}{N_{drive}}, \tag{1.3}$$

where $E_{max}^{witness}$ is the maximum accelerating field of the wake, E_{max}^{drive} is the maximum decelerating field within the drive beam itself, and $N_{witness}$ (N_{drive}) is the number of electrons (particles) in the witness (driver) bunch, respectively. Eq. (1.3) implies that individual witness electrons can at most achieve twice the energy of an individual driver particle's energy for a longitudinally symmetric driver. For example, meter long plasmas have been used to double the energy of a witness electron bunch initially accelerated via RF technology in a kilometer long conventional linear electron accelerator (LINAC) [39]. Due to the transformer ratio limitation, achieving ultra-high energy electrons $\sim$ TeV, which is of great interest in the particle physics community, is currently not possible using electron beam drivers.

To achieve unprecedented electron beam energies in the TeV range, TeV proton beams from CERN's Large Hadron Collider (LHC) have been proposed as a driver in a proton driver plasma wakefield acclerator (PDPWA) [34, 35]. For a Gaussian shaped driver bunch in which the charge bunch density is much lower than n_{p0}, the maximum axial electric field is given by [40]

$$E_{z,max} = eNk_p^2 \exp\left(\frac{-k_p^2\sigma_z^2}{2} + \frac{k_p^2\sigma_r^2}{2}\right)\Gamma(0, k_p^2\sigma_r^2/2), \tag{1.4}$$

where N is the number of particles in the driving bunch, $\Gamma(0,x) \equiv \int_x^\infty t^{\alpha-1}e^{-t}dt$ is the incomplete Gamma function, σ_r is the rms transverse size of the driv-

ing bunch in one dimension, σ_z is the rms length of the driving bunch, and $k_p \equiv \omega_p/c$ is the plasma wavenumber. According to Eq. (1.4), the σ_z value at which $E_{z,max}$ is maximized is $\sigma_z = \sqrt{2}k_p^{-1}$, and the field rapidly decays in strength for σ_z values greater than this. However, suggested plasma wavelengths of order 1 mm, which corresponds to the wave-breaking field of $\sim$1 GV/m, are much shorter than the r.m.s length of the proton beams at the LHC, $\sigma_z \sim 100\ \lambda_p$.

To resonantly excite plasma waves using a long proton beam with $\sigma_z \gg \lambda_p$, it has been suggested to rely on the so-called modulation instability (MI) within the proton beam to break it up into a 'train' of bunchlets separated by λ_p [41, 42]. The MI is a parametric, transverse, and axially symmetric electro-magnetic instability. It arises within long beams with $\sigma_z \gg \lambda_p$ and occurs because the beam generates its own wakefield within its body, leading to its self modulation and higher beam densities. This drives stronger wakefields, forming a positive feedback loop. Plasma wakefields excited towards the 'head' of the beam can only influence parts of the beam towards the 'tail', causing the instability to grow more rapidly towards the tail, making the MI a 'spatio-temporal' instability. The 'hosing-instability' (HI) [43, 44, 45], which develops in a similar way to the MI, but results in non-axially symmetric modulation throughout the proton beam and much weaker accelerating gradients, can also play an important role in the beam's evolution if given time to develop. To excite axially symmetric instability modes within the beam and ensure that the MI develops without the presence of the HI, an MI 'seed' is required. In

this thesis, we describe a novel way in which to seed the MI within a PDPWA driver, which is the first proposed experimentally achievable seeding method.

1.4 Electromagnetic field equations and plasma response

In the following sections, general expressions for the electromagnetic field equations and plasma response are obtained, which are used throughout Chapters 2, 3, and 4 of this thesis. First, Maxwell's equations are stated, then the plasma equation of motion is given. Using these two equations, global current neutrality is then demonstrated for the systems studied in this thesis. The resulting scaling relationship between the beam and plasma current densities is then used to simplify the plasma equation of motion and write down the plasma density's response to the driver bunch's density and laser pulse's ponderomotive force. Finally, with the plasma density's response known in terms of the sources, the electromagnetic field equations are written.

1.4.1 Maxwell's equations

The response of a charged particle beam propagating through a background plasma is coupled to the plasma response via the electromagnetic fields. These fields are given by Maxwell's equations:

$$\vec{\nabla} \cdot \vec{E} = 4\pi\rho, \tag{1.5}$$

$$\vec{\nabla} \cdot \vec{B} = 0, \tag{1.6}$$

$$\vec{\nabla} \times \vec{E} = -\frac{1}{c}\frac{\partial \vec{B}}{\partial t}, \tag{1.7}$$

and

$$\vec{\nabla} \times \vec{B} = \frac{4\pi}{c}\vec{J} + \frac{1}{c}\frac{\partial \vec{E}}{\partial t}, \tag{1.8}$$

where $\vec{E}$ is the electric field, $\vec{B}$ is the magnetic field, c is the speed of light, $\vec{J}$ is the current density, and ρ is the charge density. The beam and plasma both contribute to the sources $\vec{J}$ and ρ, and the plasma can both current and charge neutralize the beam. To see how this happens, it is useful to first consider the equation of motion for the plasma's electrons.

1.4.2 Plasma fluid equation of motion

To determine the plasma's dynamic response to a particle beam and laser pulse in the presence of plasma electron-ion collisions, we assume that the relatively heavy plasma ions are immobile and that the plasma electrons respond as a nonrelativistic, cold-fluid [46, 47]:

$$m_e \frac{\partial \vec{v}_p}{\partial t} + m_e(\vec{v}_p \cdot \vec{\nabla})\vec{v}_p = -e\vec{E} - e\frac{\vec{v}_p}{c} \times \vec{B} - \vec{\nabla}\phi_p - \nu m_e \vec{v}_p, \tag{1.9}$$

where $\vec{v}_p$ is the plasma electron fluid velocity, ν is the plasma-electron ion collision frequency, $\phi_p \equiv \frac{m_e c^2}{4}|a|^2$, $|a| \equiv \frac{e}{m_e c \omega_0}|\vec{E}_L|$, $\vec{E}_L$ is the electric field of a laser, and ω_0 is the laser's frequency. The term $-\nu\vec{v}_p$ accounts for momentum loss due to collisions between the plasma electron stream and plasma ions, while the term $\propto -\vec{\nabla}\phi_p$ represents the laser's ponderomotive force. The ponderomotive force is derived in Ref. [47] and can be separated from the $-e\vec{E}$,

$-e\vec{v}_p \times \vec{B}$ forces created by the fields of the plasma wake and particle beam only if $\omega_0 \gg \omega_p, \gamma_I$. Here, γ_I is the instability growth rate within the beam. Next, Eq. (1.9) and Maxwell's equations are used to show that the plasma current neutralizes the beam.

1.4.3 Current neutrality in the beam/plasma system

The plasma's equation of motion and Maxwell's equations (1.5-1.8) are now used to demonstrate that the plasma can neutralize the beam's current. We first take the curl of Eq. (1.8) and insert Eqs. (1.6) and (1.7), which gives

$$\left(\nabla^2 - \frac{1}{c^2}\frac{\partial^2}{\partial t^2}\right)\vec{B} = -\frac{4\pi}{c}\vec{\nabla} \times \vec{J}, \tag{1.10}$$

or in terms of the magnetic vector potential,

$$\left(\nabla^2 - \frac{1}{c^2}\frac{\partial^2}{\partial t^2}\right)\vec{A} = -\frac{4\pi}{c}\vec{J}. \tag{1.11}$$

We now switch from the coordinates $(\vec{x}_\perp, z, t)$ to the co-moving dependence $(\vec{x}_\perp, \zeta, t)$, where $\vec{x}_\perp$ is the position vector transverse to the beam's propagation direction, $\zeta \equiv ct - z$ is the co-moving coordinate for a relativistic beam, and z is the longitudinal spatial coordinate along the direction of propagation. The z and t derivatives then transform as $\frac{\partial}{\partial z}|_{\vec{x}_\perp,t} = -\frac{\partial}{\partial \zeta}|_{\vec{x}_\perp,t}$ and $\frac{\partial}{\partial t}|_{\vec{x}_\perp,z} = c\frac{\partial}{\partial \zeta}|_{\vec{x}_\perp,t} + \frac{\partial}{\partial t}|_{\vec{x}_\perp,\zeta}$, so that Eq. (1.11) becomes

$$\left(\nabla_\perp^2 - \frac{2}{c}\frac{\partial^2}{\partial \zeta \partial t} - \frac{1}{c^2}\frac{\partial^2}{\partial t^2}\right)\vec{A} = -\frac{4\pi}{c}\vec{J}. \tag{1.12}$$

For the systems considered in this thesis, the typical transverse length scale $\delta_\perp$ is much smaller than $c\tau$, where τ is the time scale over which change occurs at

a fixed ζ value, so that the t derivatives can be ignored in this equation. This is known as the quasi-static approximation, under which Eq. (1.12) simplifies to

$$\nabla_\perp^2 \vec{A} = -\frac{4\pi}{c}\vec{J}. \tag{1.13}$$

Equation (1.13) can be expressed in an alternate form by integrating over a transverse area A' bounded by contour L and invoking the divergence theorem:

$$\oint_L \vec{\nabla}_\perp A_m \cdot \vec{dl} = -\frac{4\pi}{c}\int_{A'} J_m d^2x_\perp, \tag{1.14}$$

where A_m and J_m are the m^{th} Cartesian components of $\vec{A}$ and $\vec{J}$, respectively. We immediately see from Eq. (1.14) that with periodic boundary conditions applied to $\vec{\nabla}_\perp A_m$ on L, which are assumed for REB propagation through a resistive plasma in Chapter 2, the LHS of Eq. (1.14) is zero, implying that the plasma neutralizes the beam's total current.

To see how Eq. (1.14) implies current neutrality for a particle beam of finite transverse width (no periodic boundary conditions) propagating through a collisionless plasma, which applies to the PDPWA driver considered in Chapters 3 and 4, we examine the behaviour of $\vec{A}$ far from the source $\vec{J_b}$. To accomplish this, we separate $\vec{J} = \vec{J_p} + \vec{J_b}$ into its beam and plasma constituents in Eqs. (1.13,1.14) and then relate $\vec{J_p}$ to $\vec{A}$. To express $\vec{J_p}$ in terms of $\vec{A}$, we rewrite $(\vec{v_p}\cdot\vec{\nabla})\vec{v_p} = \frac{1}{2}\vec{\nabla}|\vec{v_p}|^2 - \vec{v_p}\times(\vec{\nabla}\times\vec{v_p})$ in Eq. (1.9), take the curl of the resulting equation, and insert Eq. (1.7), yielding [48]

$$\frac{\partial\vec{\Omega}}{\partial t} - \vec{\nabla}\times(\vec{v_p}\times\vec{\Omega}) = -\nu\vec{\nabla}\times\vec{v_p}, \tag{1.15}$$

where $\Omega \equiv \vec{\nabla} \times \vec{v}_p - e\vec{B}/m_e c$ is the generalized vorticity. In a collisionless ($\nu = 0$), initially quiescent plasma, Eq. (1.15) implies that $\vec{\Omega} = 0$ for all times, so that $\vec{\nabla} \times \vec{v}_p = e\vec{B}/m_e c$, or

$$\vec{v}_p = e\vec{A}/m_e c. \tag{1.16}$$

With

$$\vec{J}_p \approx -en_{p0}\vec{v}_p, \tag{1.17}$$

where we have assumed the plasma number density $n_p \approx n_{p0}$ is weakly perturbed, Eqs. (1.16,1.17) yield the desired relationship between $\vec{J}_p$ and $\vec{A}$. Substituting $\vec{J} = \vec{J}_p + \vec{J}_b \approx -en_{p0}\vec{v}_p + \vec{J}_b$ into Eq. (1.13) and inserting Eq. (1.16) into the resulting equation yields

$$(\nabla_\perp^2 - k_p^2)\vec{A} = -\frac{4\pi}{c}\vec{J}_b. \tag{1.18}$$

The solution to Eq. (1.18) is given by

$$\vec{A}(\vec{x}_\perp) = \frac{4\pi}{c}\int G(\vec{x}_\perp - \vec{x}'_\perp)\vec{J}_b(\vec{x}'_\perp)d^2x'_\perp, \tag{1.19}$$

where $G(\vec{x}_\perp - \vec{x}'_\perp) \equiv iH_0^{(1)}(ik_p|\vec{x}_\perp - \vec{x}'_\perp|)/4$ is the Green's function, $H_0^{(1)}$ is the Hankel function of the first kind and order zero, and the integration is performed over the entire transverse plane. The Green's function G is a real, monotonically decreasing function and is only sizeable for $k_p|\vec{x}_\perp - \vec{x}'_\perp| \lesssim 1$. The solution Eq. (1.19) therefore implies that $\vec{A}$ decays rapidly over roughly one skin depth k_p^{-1} away from a localized source $\vec{J}_b$. In this case, the left hand side of Eq. (1.14) is zero for the contour L taken at infinity, implying that the

net current $\int_{A'} J_m d^2x_\perp$ is zero.

The existence of global current neutrality for both of the beam propagation scenarios considered in this thesis allows us to write the important scaling relation

$$n_b \vec{v}_b \sim n_p \vec{v}_p, \tag{1.20}$$

where n_b is the driver beam's number density, $\vec{v}_b$ is its velocity vector, immobile ions have been assumed. Equation (1.20) means that for the underdense beams $n_b \ll n_p$ dealt with throughout this thesis, $\vec{v}_p \sim \frac{n_b}{n_p} v_b$ and hence $\vec{v}_p \ll \vec{v}_b$. The plasma's motion can therefore be treated non-relativistically, consistent with Eq. (1.9). Next, Eq. (1.20) is used to simplify the plasma equation of motion Eq. (1.9) which enables us to derive a useful equation involving the perturbed plasma number density $\delta n_p \equiv n_p - n_{p0}$, n_b, and ϕ_p.

1.4.4 Plasma density's response to beam density and ponderomotive potential

The plasmas response to the driver beam and laser pulse is now found, resulting in an important equation that contains δn_p, n_b, and ϕ_p. To accomplish this, we first use the neutrality scaling Eq. (1.20) to simplify the plasma equation of motion. We find from Eqs. (1.5), (1.13), and (1.20) the relations $\vec{B} = \vec{\nabla} \times \vec{A} \sim \frac{4\pi q \delta_\perp}{c} \vec{n}_b \vec{v}_b$ and $\vec{E} \sim 4\pi\delta_\perp(q n_b - e\delta n_p)$, where q is the charge of a driver beam particle, which imply $\frac{\vec{E}}{\frac{\vec{v}_p}{c}\times\vec{B}} \sim n_p/n_b \gg 1$ and $\frac{e\vec{E}}{m_e(\vec{v}_p\cdot\vec{\nabla})\vec{v}_p} \sim n_p/n_b \gg 1$ assuming $\delta_\perp \sim k_p^{-1}$. Under these scalings, Eq. (1.9)

becomes

$$m_e \frac{\partial \vec{v}_p}{\partial t} = -e\vec{E} - \vec{\nabla}\phi_p - \nu m_e \vec{v}_p. \tag{1.21}$$

With Eq. (1.21), the desired relationship between δn_p and the sources n_b, ϕ_p can be now be found. Taking the divergence of Eq. (1.21) and inserting Eq. (1.5) results in

$$\frac{\partial \vec{\nabla}\cdot\vec{v}_p}{\partial t} = -\frac{\omega_p^2}{n_{p0}}\left(\frac{q}{|q|}n_b - \delta n_p\right) - \frac{1}{m_e}\nabla^2\phi_p - \nu\vec{\nabla}\cdot\vec{v}_p. \tag{1.22}$$

The plasma electrons' continuity equation is given by $\frac{\partial n_p}{\partial t} + (\vec{\nabla}\cdot\vec{v}_p)n_p + \vec{\nabla}n_p\cdot\vec{v}_p = 0$. Inserting $n_p = n_{p0} + \delta n_p$ and assuming small perturbations $\delta n_p \ll n_{p0}$, the continuity equation becomes $\frac{\partial \delta n_p}{\partial t} + (\vec{\nabla}\cdot\vec{v}_p)n_{p0} = 0$ to lowest order. The time derivative of this expression combined into Eq. (1.22) yields

$$\frac{\partial^2 \delta n_p}{\partial t^2} = \omega_p^2\left(\frac{q}{|q|}n_b - \delta n_p\right) + \frac{n_{p0}}{m_e}\nabla^2\phi + \nu n_{p0}\vec{\nabla}\cdot\vec{v}_p. \tag{1.23}$$

Upon switching from $(\vec{x}_\perp, z, t)$ to $(\vec{x}_\perp, \zeta, t)$ and assuming $\partial_t \delta n_p \ll \omega_p \delta n_p$ at a fixed ζ value, Eq. (1.23) transforms to

$$c^2\frac{\partial^2 \delta n_p}{\partial \zeta^2} = \omega_p^2\left(\frac{q}{|q|}n_b - \delta n_p\right) + \frac{n_{p0}}{m_e}\nabla_\zeta^2\phi_p + \nu n_{p0}\vec{\nabla}_\zeta\cdot\vec{v}_p, \tag{1.24}$$

where $\nabla_\zeta^2 \equiv \nabla_\perp^2 + \partial_\zeta^2$, $\vec{\nabla}_\zeta \equiv \vec{\nabla}_\perp - \hat{z}\partial_\zeta$, and $\hat{z}$ is the unit normal vector pointing along the direction of propagation. For the systems considered in this thesis, the collision frequency ν is taken to be sufficiently small that the right-most term of Eq. (1.24) can be neglected, allowing us to write

$$c^2\frac{\partial^2 \delta n_p}{\partial \zeta^2} = \omega_p^2\left(\frac{q}{|q|}n_b - \delta n_p\right) + \frac{n_{p0}}{m_e}\nabla_\zeta^2\phi_p. \tag{1.25}$$

Equation (1.25) describes the plasma's response to the sources n_b and ϕ_p. With the plasma response known, useful expressions for the electromagnetic fields are found next.

1.4.5 Field equations for REB propagation described in Chapter 2

The field equations for REB propagation described in Chapter 2 are now derived. For beams that are sufficiently long and smooth, which is the case for the REB considered in this thesis, the ζ derivatives in Eq. (1.25) are negligible. Assuming that there is no laser present ($\phi_p = 0$), Eq. (1.25) then becomes

$$n_b = -\delta n_p, \tag{1.26}$$

the quasi-neutrality relation. Under quasi-neutrality, the electro-magnetic fields can be characterized solely by the potential $\vec{A}$. If the beam's transverse directed velocity is much smaller than its longitudinal velocity, which is assumed in this thesis, then according to Eq. (1.13), the transverse components of $\vec{A}$, $\vec{A}_\perp$, are much smaller than the longitudinal component ψ. The dominant fields can therefore be determined from ψ only, so that the transverse magnetic field and longitudinal electric field are given by

$$\vec{B}_\perp = -\hat{e}_z \times \vec{\nabla}\psi \tag{1.27}$$

and

$$E_z = -\frac{1}{c}\frac{\partial \psi}{\partial t}, \tag{1.28}$$

respectively. Since $\vec{A}_\perp$ is small, we neglect the longitudinal magnetic field. The transverse electric field, though small, can be estimated by setting the

LHS of Eq. (1.9) equal to zero and neglecting the effect of plasma resistivity on transverse motion, resulting in

$$\vec{E}_\perp = \frac{v_{pz}}{c}\vec{\nabla}\psi. \tag{1.29}$$

The assumption of transverse force equilibrium in the plasma fluid is justified since the transverse electron plasma velocity of order $\vec{v}_{p\perp} \sim \frac{n_b}{n_p}\vec{v}_{b\perp}$ is very small for low transverse beam temperatures. The treatment outlined in this subsection was originally described in Ref. [46]. Next, we derive the expressions for the electromagnetic fields that are used in Chapters 3 and 4.

1.4.6 Field equations for PDPWA driver propagation described in Chapters 3 and 4

The electromagnetic field equations relevant to PDPWA propagation described in Chapters 3 and 4 are now found. The electric field experienced by the PDPWA driver can be calculated by first taking the time derivative of Eq. (1.8), inserting Eq. (1.7), and then substituting $\vec{\nabla} \times (\vec{\nabla} \times \vec{E}) = \vec{\nabla}(\vec{\nabla} \cdot \vec{E}) - \nabla^2\vec{E} = 4\pi\vec{\nabla}\rho - \nabla^2\vec{E}$, resulting in

$$\left(\nabla^2 - \frac{1}{c^2}\frac{\partial^2}{\partial t^2}\right)\vec{E} = \frac{4\pi}{c^2}\frac{\partial \vec{J}}{\partial t} + 4\pi\vec{\nabla}\rho. \tag{1.30}$$

Separating $\vec{J} = \vec{J}_b + \vec{J}_p$ into its beam and plasma components in Eq. (1.30) yields

$$\left(\nabla^2 - \frac{1}{c^2}\frac{\partial^2}{\partial t^2}\right)\vec{E} = \frac{4\pi}{c^2}\frac{\partial \vec{J}_b}{\partial t} - \frac{4\pi e n_{p0}}{c^2}\frac{\partial \vec{v}_p}{\partial t} + 4\pi\vec{\nabla}\rho, \tag{1.31}$$

where we have neglected δn_p in computing $\vec{J}_p = -e(n_{p0}+\delta n_p)\vec{v}_p \approx -en_{p0}\vec{v}_p$ under the assumption $\delta n_p \ll n_{p0}$. We now seek the wakefields downstream from

a laser pulse that are experienced by a much longer particle beam. Inserting Eq. (1.21) with $\phi_p = 0$ into Eq. (1.31) yields

$$\left(\nabla^2 - k_p^2 - \frac{1}{c^2}\frac{\partial^2}{\partial t^2}\right)\vec{E} = \frac{4\pi}{c^2}\frac{\partial \vec{J_b}}{\partial t} + 4\pi e\vec{\nabla}(n_b - \delta n_p). \tag{1.32}$$

Switching to the co-moving dependence in the quasi-static approximation and assuming cylindrical symmetry, Eq. (1.32) becomes [49]

$$\left(\nabla_\perp^2 - k_p^2\right)\vec{E} = -4\pi e\frac{\partial \vec{\delta} n_p}{\partial \zeta}\hat{z} + 4\pi e\frac{\partial}{\partial r}\left(n_b - \delta n_p\right)\hat{r}. \tag{1.33}$$

To determine $\vec{B}$, we take the curl of Eq. (1.18) [49]:

$$\left(\nabla_\perp^2 - k_p^2\right)\vec{B} = 4\pi e\frac{\partial n_b}{\partial r}\hat{\theta}. \tag{1.34}$$

From Eqs. (1.33) and (1.34), we see that the wakefield $\vec{W}_\perp \equiv e\vec{E}_\perp + e\widehat{z} \times \vec{B}_\perp$ and longitudinal electric field are thus determined from the single potential ψ given by [49]

$$(\nabla_\perp^2 - k_p^2)\psi = -4\pi e\delta n_p \tag{1.35}$$

according to

$$\vec{W}_\perp = \vec{\nabla}_\perp \psi \tag{1.36}$$

and

$$\vec{W}_\perp = \vec{\nabla}_\perp \psi, E_z = -\frac{\partial \psi}{\partial \zeta}. \tag{1.37}$$

1.5 Summary

This thesis is divided into three main chapters. Chapter 2 gives theoretical and qualitative descriptions of the nonlinear stage of the resistive WI

for an initially cold and fully current neutralized beam in the underdense beam limit with supporting computational results. The temporal evolution of the beam and its overall stopping time are calculated. In Chapter 3, we demonstrate that a laser pulse placed ahead of a PDPWA driver beam can efficiently seed the modulation instability within the driver beam and create maximal accelerating gradients that are comparable previously proposed seeding methods. The envelope equation for the proton beam's r.m.s radius is used to analytically describe these seeding methods, providing a theoretical comparison between each seed. Simulations are then used to supplement our theory and describe more realistic beam propagation scenarios. Chapter 4 describes a harmonic expansion formalism that attempts to describe the nonlinear stage of the modulation instability with the PDPWA driver. The formalism is developed first, then several crippling problems with it are identified. Despite this negative result, it is still important for the community to learn about the techniques that were attempted here so that it may try other methods and approximations to describe the nonlinear stage of the modulation instability.

The Appendix consists of three separate derivations that supplement the material within Chapters 2, 3, and 4. Appendix A derives the expression for the longitudinal electric field in the narrow beam limit generated by the PDPWA driver, which requires special treatment. Appendix B calculates the asymptotic behaviour of the perturbed beam radius of the PDPWA driver during the linear stage of the MI using complex analysis and steepest descent techniques. Finally, Appendix describes the separation of the co-propagating

longitudinal coordinate into the fast and slow variables relied upon by the harmonic expansion formalism used in Chapter 4.

Chapter 2

Analytic model of electron beam thermalization during the resistive Weibel Instability

2.1 Introduction and motivation

[1] Relativistic electron beam propagation through a background plasma occurs in a variety of physical systems, including inertial confinement fusion and astrophysical scenarios [1, 2, 3, 9, 50, 51, 52, 53]. In the originally envisioned Fast Ignition (FI) scheme, underdense relativistic electron beams (MeV) produced by a laser near the critical surface density are the final transport mechanism for energy deposition into the core of a pre-compressed target pellet, sparking the ignition [9]. Therefore, it is of great interest to understand the physics of this transport process both far away from and close to the dense target core, where plasma electron-plasma ion collisions are negligible and prevalent, respectively, due to increased plasma density. According to this scheme, the electron beam should stop inside the dense core and deposit its energy through collisions [9]. Electron beams with too high energies are capa-

[1]This chapter was previously published in the work *C. Siemon, V. Khudik, and G. Shvets, Physics of Plasmas* **18,** *103109 (2011).* Vladimir Khudik provided supporting work and Gennady Shvets was the supervisor.

ble of propagating through the core without stopping, failing to deposit their energy into it, while electron beams traveling too slowly can become scattered by collisions in the coronal region of the target before reaching the core [9].

The electric current carried by an underdense, 'fast' moving electron beam excited by the laser is quickly neutralized by an induced plasma return current, which is dense and 'slow' moving [12]. This is an unstable configuration that results in collective instabilities. The electrostatic two stream/oblique instabilities play a less significant role for high energy beams because they are believed to saturate by beam electron trapping before a significant fraction of the beam's energy is removed [13, 14, 15]. For relativistic beams, the robust instability is the transverse electromagnetic Weibel Instability (or WI) [16]. The WI leads to beam pinching and filamentation, beam and plasma heating, and the generation of strong magnetic fields [16, 17, 18, 19]. It is an important mechanism for beam slowing because it induces transverse thermalization and transfers energy from the beam to fields and background plasma [16]. The WI proceeds through the linear stage, in which beam density and magnetic field strength grow exponentially in time, and the nonlinear stage, in which beam filaments formed during the linear stage merge together.

Electron beam propagation has been studied using full Particle-in-Cell codes [17, 18, 59, 60, 61, 64], but it is, in general, very difficult to model FI scenarios with these codes. This is due to the large temporal and spatial scales involved and also the large number of macroparticles required to simulate high-density plasmas. Reduced hybrid approaches that treat the beam kinet-

ically and background plasma as a fluid mitigate this problem [55, 56, 57, 58]. The theory developed in this chapter is supported computationally by the 2-d hybrid models described in Refs. [46, 54, 68]. The model neglects two stream/oblique instabilities [13, 14, 15] because it assumes high beam energies and deals only with the effect of the WI on the beam's dynamics. The interplay between these instabilities is beyond the scope of this chapter.

While the original FI concept [9] relied on the electon beams losing energy via direct collisions (collisional stopping) with the ambient plasma, this mechanism is significantly suppressed due to the strong inverse dependence of the collision frequency on the beam's energy [69]. Finite plasma resistivity (FPR) presents another important mechanism for beam slowing since it produces energy dissipation and enhances energy transfer from the beam to magnetic field (due to enhanced filament merging caused by magnetic field diffusion). In this chapter, the effects of FPR on beam deceleration, which could possibly lead to much shorter stopping times than expected, are investigated without considering the simple, uninteresting collisional stopping mechanism. For underdense beams, this is most relavent to the coronal regions of FI targets, where the plasma temperature T_p is lower than it is in the core, and also for moderately low beam-plasma density ratios, n_b/n_p. This can be seen by taking the ratio of the collisional stopping time $\tau_c \sim \frac{m^2c^3\gamma(t=0)}{4\pi n_p e^4 \log(\lambda_c)}$ [11] discussed in Section 1.2 (valid scaling for >MeV beams) to the FPR stopping time $\tau_r \sim \frac{\gamma(t=0)}{\nu(n_b/n_p)} \sim \frac{\gamma(t=0)10^6 T_p^{3/2}}{4n_p(n_b/n_p)\log(\lambda_r)}$ (derived in Section 2.3), which is

$$\Gamma \equiv \tau_c/\tau_r \sim \frac{3(n_b/n_p)\log(\lambda_r)}{10(T_p/mc^2)^{3/2}\log(\lambda_c)}. \tag{2.1}$$

Here, m is the electron mass, c is the speed of light, $\gamma(t = 0)$ is the initial relativistic Lorentz factor for the beam, $\nu \sim 4 \cdot 10^{-5} T_p^{-3/2} n_p$ [69] is the plasma electron-ion collision frequency for light ions, and $\log(\lambda_r) \sim 10$ is the Coulomb logarithm for plasma electron-ion collisions [69]. Also, the logarithm $\log(\lambda_c)$ depends on the plasma's degeneracy and beam's energy and is typically ~ 10 for $\sim$ MeV beams [11]. As an example, $\Gamma \approx 10$ for $T_p = 500$ eV and $n_b/n_p = 1/1000$.

The linear stage of the resistive WI has been studied both analytically and computationally [54, 57, 63, 64], but analytic descriptions of the nonlinear stage are limited. This chapter gives theoretical and qualitative descriptions of the nonlinear stage of the resistive WI for an initially cold and fully current neutralized beam in the underdense beam limit, with supporting computational results. The temporal evolution of the beam and its overall stopping time are calculated.

To set the stage for the rest of the chapter, the typical evolution of an underdense, filamenting electron beam (Case 1) during the nonlinear stage of the resisitve WI (WI in the presence of plasma electron-ion collisions) is presented in Fig. 2.1. Case 1 shows unusual behavior when compared to the evolution of a uniformly distributed, filamentation-suppressed beam (Case 2) in which there is no WI. In Case 1, filaments are merging until they collect into one filament at time $t = 10^5 \omega_p^{-1}$, where $\omega_p = \sqrt{\frac{4\pi e^2 n_p}{m}}$ is the plasma frequency in CGS units, which will be used throughout this chapter. Past this time, there is only one filament propagating, which shows how the beam decelerates

when filaments are separated by far enough distances (on average) that they are essentially isolated from each other. The bottom row of Fig. 2.1 shows beam density snapshots for Case 1 during both of these stages. This figure raises the following questions, which are answered by this chapter: why is beam deceleration enhanced during the early stage (filaments' merger) of the beam's evolution, and why is deceleration reduced when Case 1's filaments are essentially isolated from each other?

The remainder of this chapter is organized as follows. The hybrid model of charge-neutralized beam propagation through a denser plasma [46, 54, 68] is reviewed in Section 2.2, and the background information pertaining to the WI is also presented there. The 0-dimensional model of beam deceleration due to finite plasma resisitivity is presented in Section 2.3. The diffusion of magnetic field during the resistive WI and its effect on filament merging is described in Section 2.4. The quantitave description of individual beam filaments in Bennett equilibrium is given in Section 2.5. The magnetic and electron plasma fluid energies in a filamented-beam system are calculated in Section 2.6. The qualitative description of filamented-beam deceleration is discussed in Section 2.7. The analytic calculation of filamented-beam dynamics and also the calculation of filamented-beam propagation stopping time are presented in Section 2.8.

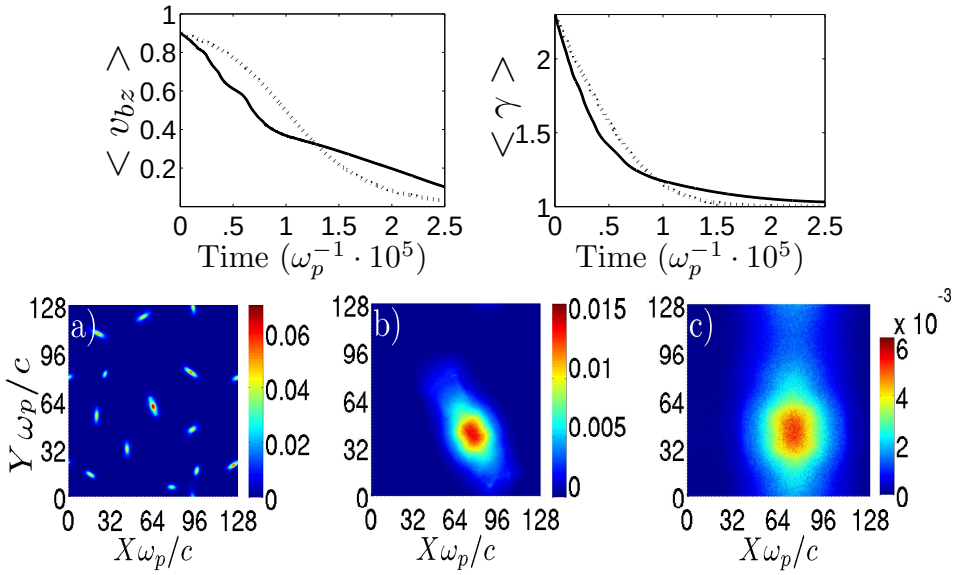

Figure 2.1: Anamolous beam slowing of a filamenting beam during the nonlinear stage of the resistive Weibel Instability (Case 1) when compared to a uniformly distributed, filamentation-suppressed beam (Case 2). Top row: solid and dashed lines- simulated $< v_{bz}(t) >$ (longitudinal beam velocity) and $< \gamma(t) >$ for Cases 1 and 2, respectively. Brackets denote average over beam particles. Bottom row: simulated n_b/n_i snapshots for Case 1 at times $10^4\omega_p^{-1}$, $10^5\omega_p^{-1}$, and $1.65 \cdot 10^5\omega_p^{-1}$ in a), b), and c) respectively. Beam and plasma paramters: initial density $n_b(t=0)/n_p = 1/1000$, initial beam energy $\gamma(t=0) = 2.29$, and constant collision frequency $\nu = .02\omega_p$.

2.2 Equations and background

The theory presented and supporting computational results are based on the model discussed in Refs. [46, 54, 68]. The model describes a relativistic electron beam propagating through a resistive background plasma. The beam is initially current neutralized by a slower moving, counter-propagating plasma electron current (return current). The model assumes quasi-neutrality, which is valid when the beam density n_b is much less than the background plasma electron density n_p, so that $n_b << n_p$ is also assumed. The growth rate of the dominant beam-plasma instability that arises in the system, the Weibel Instability, is therefore much smaller than the plasma frequency in the high beam energy-low beam density limit [16, 17, 18, 19], so that rapid plasma oscillations average out over the development of the instability. The beam is assumed to be long ($L_{beam} >> c/\omega_p$), so that $\frac{\partial}{\partial z} \equiv 0$, which enables a 2-D simulation (particles pushed in transverse plane). The relativistic beam electrons have much higher energy than the counter streaming plasma electrons, enabling them to be treated as a separate species- the beam electrons are modeled kinetically, plasma electrons as a fluid, and ions are immobile.

The expressions for the electromagnetic fields and plasma fluid response are now given, which have been derived in more detail in Section 1.4. The dominant magnetic field is in the transverse plane, which generates an inductive electric field E_z. The transverse electric field is found from the equation for plasma electron equilibrium in the transverse plane- $\vec{E}_\perp + \frac{v_{pz}}{c}\vec{e}_z \times \vec{B}_\perp = 0$, where v_{pz} is the longitudinal plasma electron velocity. In summary, the fields

are given by

$$\vec{B}_\perp = -\vec{e}_z \times \vec{\nabla}_\perp \psi,$$

$$\vec{E}_\perp = -\frac{v_{pz}}{c}\vec{\nabla}_\perp \psi,$$

and

$$E_z = -\frac{1}{c}\frac{\partial \psi}{\partial t},$$

where ψ is the longitudinal magnetic vector potential. The longitudinal magnetic field is small and is neglected in what follows.

The z-projection of the plasma electron equation of motion given by Eq. (1.21) (with the absence of a laser pulse, $\phi_p = 0$) is

$$\frac{\partial v_{pz}}{\partial t} + \nu v_{pz} = \frac{e}{mc}\frac{\partial \psi}{\partial t}, \tag{2.2}$$

where ν is the plasma electron-ion collision frequency, which is assumed to be constant. The beam electrons' equations of motion are given by

$$\frac{d(\gamma v_{jz})}{dt} = -\frac{e}{m}(E_z + \frac{\vec{v}_{j\perp}}{c} \times \vec{B}_\perp \cdot \vec{e}_z) = \frac{e}{mc}\frac{d\psi}{dt} \tag{2.3}$$

and

$$\frac{d(\gamma \vec{v}_{j\perp})}{dt} = \frac{e}{mc}(v_{pz} - v_{jz})\vec{\nabla}_\perp \psi, \tag{2.4}$$

where ψ is evaluated at the beam electron's position.

Ampere's law is used to solve for ψ, forming a closed system for the

fields ψ and particles, which is described in more detail in Section 1.4.3. Projecting Eq. (1.13) onto the z axis yields

$$\nabla^2\psi = \frac{4\pi e}{c}(v_{pz}n_p + v_{bz}n_b). \tag{2.5}$$

Numerical results for this chapter were obtained from 2-D hybrid PIC simulations [46, 54, 68] of initially charge/current neutralized, cold, underdense, uniformly distributed, flat top velocity beams. The plasma electron-ion collision frequency ν was held fixed throughout the simulations, consistent with previous treatments [54, 57]. The beam filaments merge until there is only one filament remaining in the computational domain of area $(128c/\omega_p)^2$. This reduced hybrid model is used to model collisional beam filamentation shown in Fig. 2.1 and all subsequent figures.

A propagating charge/current neutralized beam is unstable because its current is repelled by the counter-propagating return current. This repulsion creates density perturbations that induce magnetic fields. The magnetic fields then deflect particles further, enhancing density, which forms a feedback loop that results in exponential growth in the magnetic field and density perturbations. To model this process, known as the linear stage of the Weibel instability, we first write Eq. (2.5) in the limit of small beam density ($n_b \ll n_p$) and under the assumption of quasi-neutrality in which $n_p \approx n_{p0}$:

$$\nabla^2\psi = \frac{4\pi e}{c}(v_{pz}n_{p0} + v_{bz}n_b). \tag{2.6}$$

Here, n_{p0} is the quiescent background plasma number density. v_{bz} and γ will be treated as constants for simplicity in the following analysis of the linear

stage. To compute the beam density during the linear stage, we use: a) the transverse equation of motion for the electron beam in fluid form,

$$\frac{\partial \vec{v}_{b\perp}}{\partial t} = -\frac{ev_{bz}}{\gamma mc}\vec{\nabla}_{\perp}\psi, \tag{2.7}$$

where we have assumed $v_{bz} \gg v_{pz}$ (valid for underdense beams) and also small transverse beam temperature; and b) the beam's continuity equation

$$\frac{\partial n_b}{\partial t} = -n_b\vec{\nabla}\cdot\vec{v}_{b\perp} - \vec{\nabla}n_b\cdot v_{b\perp} \approx -n_b\vec{\nabla}\cdot\vec{v}_{b\perp}, \tag{2.8}$$

where we have used $n_b\vec{\nabla}\cdot\vec{v}_{b\perp} \gg \vec{\nabla}n_b\cdot v_{b\perp} = \vec{\nabla}\delta n_b\cdot v_{b\perp}$ for small beam density perturbations $\delta n_b \equiv n_b - n_{b0}$ from the initial uniform value n_{b0}. Rearranging Eq. (2.8) and taking the partial time derivative gives

$$\vec{\nabla}\cdot\frac{\partial \vec{v}_{b\perp}}{\partial t} = -\frac{\partial^2 \ln(n_b)}{\partial t^2}, \tag{2.9}$$

which becomes

$$\nabla^2\psi = \frac{\gamma mc}{ev_{bz}}\frac{\partial^2 \ln(n_b)}{\partial t^2} \tag{2.10}$$

upon insertion of the divergence of Eq. (2.7). Inserting Eq. (2.10) into Eq. (2.6) and applying the operator $\frac{\partial}{\partial t} + \nu$ gives

$$\frac{\gamma mc}{ev_{bz}}\frac{\partial^3 \ln(n_b)}{\partial t^3} + \frac{\gamma mc}{ev_{bz}}\nu\frac{\partial^2 \ln(n_b)}{\partial t^2} = \frac{4\pi e^2}{mc^2}\frac{\partial \psi}{\partial t}n_{p0} + \frac{4\pi ev_{bz}}{c}\frac{\partial n_b}{\partial t} + \frac{4\pi e\nu v_{bz}}{c}n_b, \tag{2.11}$$

where we have used Eq. (2.2). Acting $\nabla_{\perp}^2$ on Eq. (2.11) and inserting Eq. (2.10) gives a closed equation for n_b:

$$\frac{\gamma m}{e\beta_0}\frac{\partial^3\nabla_{\perp}^2 \ln(n_b)}{\partial t^3} + \frac{\gamma m}{e\beta_0}\nu\frac{\partial^2\nabla_{\perp}^2 \ln(n_b)}{\partial t^2} = \frac{4\pi e\gamma n_{p0}}{c^2\beta_0}\frac{\partial^3 \ln(n_b)}{\partial t^3} + 4\pi e\beta_0\frac{\partial\nabla_{\perp}^2 n_b}{\partial t} + 4\pi e\beta_0\nu\nabla_{\perp}^2 n_b, \tag{2.12}$$

where $\beta_0 \equiv v_{bz}/c$. Writing $n_b = n_{b0} + \delta n_b$ and $\frac{\partial \ln(n_b)}{\partial t} \approx \frac{1}{n_{b0}}\frac{\partial n_b}{\partial t}$ for $\delta n_b \ll n_{b0}$, Eq. (2.12) becomes

$$\frac{\gamma m}{e n_{b0}\beta_0}\frac{\partial^3 \nabla_\perp^2 n_b}{\partial t^3} + \frac{\gamma m}{e\beta_0 n_{b0}}\nu\frac{\partial^2 \nabla_\perp^2 n_b}{\partial t^2} = \frac{4\pi e\gamma n_{p0}}{c^2\beta_0 n_{b0}}\frac{\partial^3 n_b}{\partial t^3} + 4\pi e\beta_0\frac{\partial \nabla_\perp^2 n_b}{\partial t} + 4\pi e\beta_0\nu\nabla_\perp^2 n_b. \quad (2.13)$$

Introducing the constants $\omega_{b0} = \sqrt{\frac{4\pi e^2 n_{b0}}{\gamma m}}$ and $k_{pe} = c/\omega_{pe}$, Eq. (2.13) becomes

$$\frac{\partial^3 \nabla_\perp^2 n_b}{\partial t^3} + \nu\frac{\partial^2 \nabla_\perp^2 n_b}{\partial t^2} = k_{pe}^2\frac{\partial^3 n_b}{\partial t^3} + \beta_0^2\omega_{b0}^2\frac{\partial \nabla_\perp^2 n_b}{\partial t} + \beta_0^2\omega_{b0}^2\nu\nabla_\perp^2 n_b. \quad (2.14)$$

Equation (2.14) describes the evolution of the beam's density during the linear stage of the resistive Weibel instability. To determine how a perturbation with transverse wavevector $\vec{k}_\perp$ grows, we insert $n_b \sim e^{i(\vec{k}_\perp\cdot\vec{x}_\perp - \omega t)}$ into Equation (2.14) and solve the resulting eigenvalue problem, yielding the dispersion relation [54]

$$\omega^2 = -\frac{\omega_{b0}^2\beta_0^2\vec{k}_\perp^2}{\vec{k}_\perp^2 + k_{pe}^2/(1 + i\nu/\omega)}. \quad (2.15)$$

The Weibel growth rates are given in the limiting cases of $\nu >> \gamma_W$ and $\nu \to 0$ as

$$\gamma_W^{strong} \approx \frac{\omega_{b0}^2\beta^2 k_{pe}^2}{k_\perp^2\nu}$$

and

$$\gamma_W^{weak} \approx \frac{\omega_{b0}\beta k_\perp}{\sqrt{k_{pe}^2 + k_\perp^2}},$$

respectively. The expressions for γ_W^{strong} and γ_W^{weak} are applicable in the limits $\nu >> \nu_{crit}$ and $\nu << \nu_{crit}$, respectively, where

$$\nu_{crit} = \frac{\omega_{b0}\beta_0 k_{pe}^2 \sqrt{k_{pe}^2 + \vec{k}_\perp^2}}{\vec{k}_\perp^3}.$$

The growth in magnetic field and density perturbations described by these growth rates characterizes the linear stage of the resistive Weibel Instability (WI).

Eventually, the increasing density perturbations become comparable to and exceed the initial, unperturbed density, so that the linear stage saturates and exponential growth ceases, marking the beginning of the nonlinear stage of the WI. At this point, particles execute oscillatory motion within isolated, high beam density regions, or filaments, with 'bounce' frequency equal to the Weibel growth rate [17]. These filaments exert attractive parallel-parallel current forces on each other, causing them to merge. Figure 2.2 displays simulated beam density snapshots that show filament merging during the nonlinear stage of the WI for a strongly resistive system in which the growth rate of the linear stage is given by γ_W^{strong}. The simulation parameters and snapshot times are stated in the figure description.

In the next section, uniformly distributed beam propagation through a resistive plasma without filamentation (WI is suppressed artificially) is considered as a basis for comparison to the case of a filamenting beam (with WI). This highly simplified description is referred to as the 0-dimensional model (0-D) model.

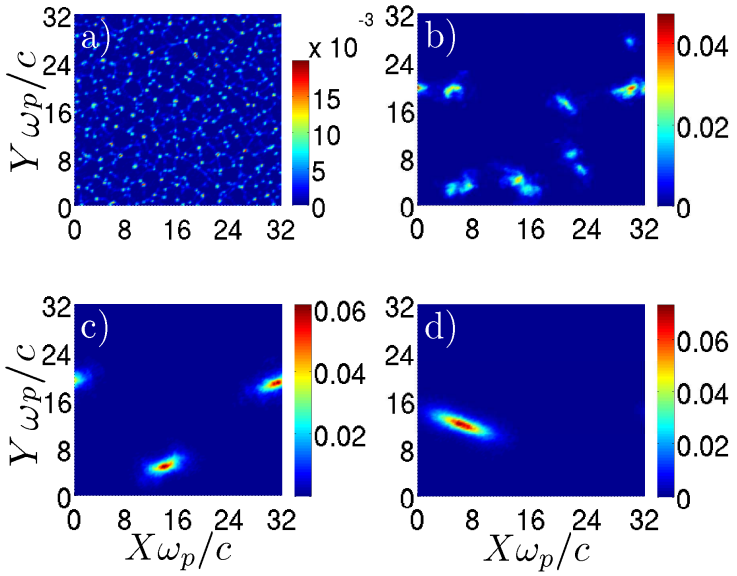

Figure 2.2: Density snapshots during filament's merger for a strongly resistive simulation. a), b), c) and d) show n_b/n_p at times $540\omega_p^{-1}$, $1.1 \cdot 10^3\omega_p^{-1}$,$1.8 \cdot 10^3\omega_p^{-1}$, and $4.5 \cdot 10^3\omega_p^{-1}$, respectively, for simulation with $\gamma(t = 0) = 2.29$, $n_{b0}/n_p = .001$, $\nu = .1\omega_p$, and $L_d = 32c/\omega_p$.

2.3 Deceleration of a uniformly distributed beam with suppressed filamentation: 0-D model

Cosider a system of merging filaments that have collected from an initially uniform, cold beam of density n_{b0} propagating through a resistive plasma. To study the effect of the resistive WI on beam deceleration, it is useful to compare this system to the propagation of a uniformly distributed beam of density n_{b0} in which filamentation is suppressed (0-D beam). The only mechanism for the 0-D beam to slow is through the electric field E_z induced by the resistive plasma. This field arises because plasma electrons are slowed down by collisions so that the plasma, seeking to neutralize current, induces an electric field along the beam propagation direction that decelerates the beam. This is expressed as

$$\frac{d(\gamma v_z)}{dt} = -\frac{e}{mc}E_z = \nu v_{pz} + \frac{\partial v_{pz}}{\partial t},$$

where transverse motion has been neglected. Inserting the current neutrality relationship $n_{b0}v_{bz} = -n_{p0}v_{pz}$ into this equation gives a closed equation for $v_{bz}(t)$:

$$\frac{d(\gamma v_{bz})}{dt} = \frac{-n_{b0}}{n_{p0}}(\nu v_{bz} + \frac{\partial v_{bz}}{\partial t}). \tag{2.16}$$

The neutrality relation $n_{b0}v_{bz} = -n_{p0}v_{pz}$ is the consequence of the 0-d model. Eq. (2.16) defines the resistive slowing-down (momentum-dissipation) time scale

$$\tau_r \equiv \gamma(t=0)(\nu n_b/n_p)^{-1}$$

for the filamentation-suppressed beam. This is the same slowing time scale for a beam in which filamentation is not suppressed, as shown later in Section 2.8.3. τ_r is referred to as the resistive slowing-down time scale throughout the remainder of this chapter.

2.4 Filament merging and diffusion of the magnetic field

In this section, the process of filament merging is described, which is essential for understanding the temporal evolution of the beam-plasma system during the resistive WI. Without resistivity, filament merging is impeded because filaments separated by distances greater than c/ω_p are effectively screened from each other. With finite resistivity, however, merging is expedited because plasma resistivity enables magnetic field diffusion, which allows filaments to exert attractive forces on each other over distances much greater than c/ω_p. Fig. 2.3, which demonstrates this effect, displays the beam density evolution during the nonlinear stage for a strongly resistive simulation (top row) and a collisionless resistive simulation (bottom row). The system parameters, which are the same for each system (except for resistivity), and density snapshot times are given in the figure's caption.

Rewriting Ampere's law as the diffusion equation shows that plasma resistivity enables diffusion. This is done by neglecting the inertial term in the

plasma equation of motion-

$$\frac{\partial v_{pz}}{\partial t} + \nu v_{pz} \approx v_{pz}/\tau_r + \nu v_{pz} \approx \nu v_{pz} \approx \frac{e}{mc}\frac{\partial \psi}{\partial t},$$

or

$$\nu v_{pz} \approx -\frac{e}{m}E_z = \frac{e}{mc}\frac{\partial \psi}{\partial t}, \tag{2.17}$$

which is valid for underdense beams since $\tau_r \equiv \gamma(t=0)(\nu n_b/n_p)^{-1} << \nu^{-1}$. Inserting this into Ampere's law gives the diffusion equation with source $n_b v_{bz}$-

$$\nabla^2 \psi = \frac{\omega_p^2}{\nu c^2}\frac{\partial \psi}{\partial t} + \frac{4\pi e}{c} n_b v_{bz}. \tag{2.18}$$

Identifying the constant of diffusivity in this equation as $D = \nu c^2/\omega_p^2$, the area of magnetic field spread at a given time is estimated as

$$r_\star^2 \approx 4Dt. \tag{2.19}$$

Since magnetic field diffusion is the slowest process in the context of filament merging, the number of filaments $N_f(t)$ remaining in a computational domain of L_d^2 after elapsed time t is approximately

$$N_f \approx L_d^2/r_\star^2 = L_d^2\omega_p^2/(4\nu c^2 t). \tag{2.20}$$

The simulation presented in the top row of Fig. 2.3 supports this relation. Note that $r_\star \sim \sqrt{L_d^2/N_f}$ is the average separation distance between filaments.

Several relationships regarding the plasma electrons can now be made that greatly symplify the modelling of this sytem: since v_{pz} diffuses with ψ, as implied by Eq. (2.17), the return current is diffused throughout the area $r_\star^2$;

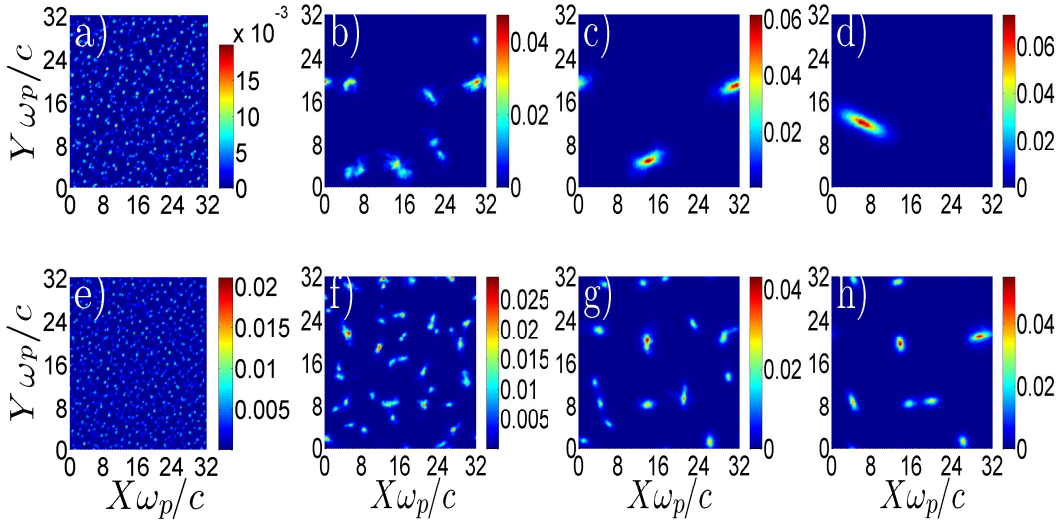

Figure 2.3: Comparison between the rates of filaments' merger in the plasma with finite (top row) and vanishing (bottom row) resistivity. Top row- a), b), c) and d) show n_b/n_p at times $540\omega_p^{-1}$,$1.1\cdot10^3\omega_p^{-1}$,$1.8\cdot10^3\omega_p^{-1}$, and $4.5\cdot10^3\omega_p^{-1}$, respectively, for $\gamma(t=0)=2.29$, $n_{b0}/n_p=.001$, $\nu=.1\omega_p$, and $L_d=32c/\omega_p$. Bottom row- same as top row except $\nu=0\omega_p$. Merging is expedited in the top row because plasma resistivity enables magnetic field diffusion.

assuming that the typical area of a filament πr_f^2 remains of order $\sim (c/\omega_p)^2$, the inequality $r_\star^2 >> r_f^2$ is true during most of the beam's evolution according to Eq. (2.19); the return current fully neutralizes a filament's current within the area $r_\star^2$, as seen by integrating Ampere's law across the transverse plane. Within filaments, the plasma return current density is therefore typically much smaller in magnitude than the beam's current density.

Next, a description of the beam's filaments are given that enable the dynamics of the beam-plasma system to be calculated.

2.5 Internal structure of a single beam filament: Bennett pinch equilibrium

Before beam slowing during the nonlinear stage of the resistive WI can be discussed qualitatively and quantified, it is necessary to describe the internal structure of the beam's filaments. In this section, some of the useful relationships between the temperature, size, and current of a self-focused electron beam are derived/reviewed. The role of the plasma is to charge-neutralize the beam. For situations in which the longitudinal velocity is not changing or changing slowly, one can expect a beam filament to enter an equilibrium or near equilibrium state. Since the beam particles are thermalized by the transverse magnetic field, it is natural to assign transverse temperature to a filament. For a filament to be in equilibrium, the inward magnetic pressure must balance the outward thermal pressure of the filament. Expressing the thermal pressure as $P_b = n_b k_B T_b$, where T_b is defined as $k_B T_b = \frac{\gamma}{2} m < v_{b\perp}^2 >$

(brackets denote average over beam particles), the transverse force balance equation for an electron filament is given by

$$\vec{\nabla}_{\perp}(n_b k_B T_b) = -e n_b[\vec{E}_{\perp} + \beta_{bz} B_{\theta}\hat{r}], \tag{2.21}$$

where $\beta_{bz} = v_{bz}/c$.

In order to make use of this equation, the following assumptions are made: cylindrical symmetry; β_{bz} and T_b are uniform throughout the filament; the plasma return current is negligible compared to the beam's current within the filament. The last assumption enables the magnetic field to be calculated from Ampere's law as

$$B_{\theta} = \frac{4\pi}{r} e \int_0^r dr^{'} r^{'} n_b(r^{'}) \beta_{bz},$$

where r is the distance from the center the filament. The radial electric force $-e\vec{E}_{\perp} = e\beta_{pz} B_{\theta}\hat{r}$ is much less than the $-e\beta_{bz} B_{\theta}\hat{r}$ force since $v_{bz} >> v_{pz}$, so that it can be neglected. With these relations, the force balance equation becomes

$$\frac{k_B T_b}{n_b}\frac{\partial n_b}{\partial r} = -\frac{4\pi e^2 \beta_{bz}}{r} \int_0^r dr^{'} r^{'} n_b(r^{'}), \tag{2.22}$$

which can be solved to give the density profile

$$n_b(r) = \widehat{n}_b/(1 + r^2/r_f^2)^2.$$

$\widehat{n}_b$ and r_f are the maximum beam density and approximate filament radius, respectively. $\widehat{n}_b$ is related to r_f through the relationship

$$2k_B T_b/(e^2 \beta_{bz}^2) = \widehat{n}_b \pi r_f^2. \tag{2.23}$$

This equation expresses the standard Bennett pinch equilibrium [66].

Integrating the above density profile over the transverse plane yields the particle conservation identity

$$\widehat{n}_b \pi r_f^2 = N_b, \tag{2.24}$$

where N_b is the number of particles per filament per unit length. With this relation, Eq. (2.24) combined with Eq. (2.23) yields another useful form of the Bennett equilibrium:

$$m\gamma < v_{b\perp}^2 > /(e^2 \beta_{bz}^2) = N_b. \tag{2.25}$$

The assumption of Bennett pinch equilibrium becomes invalid when the beam's velocity changes too rapidly and its filaments' outward temperature/pressure cannot adjust to the decreasing inward magnetic pressure, causing the filaments to expand. This typically happens when a) the beam's energy is low so its velocity rapidly decays; and b) filament merging, which increases magnetic pressure and helps to hold filaments together, is no longer prevalent. To understand criterion a), consider an isolated filament that is decelerated by the electric field that exists due to plasma electron-ion collisions (discussed in Section 2.3). For $v_{bz}^2 >> v_{b\perp}^2$, the longitudinal equation of motion for the beam electrons is approximately $\frac{\partial m\gamma v_{bz}}{\partial t} \sim -eE_z$, which can be rewritten as $\frac{\partial m v_{bz}}{\partial t} \sim \frac{-eE_z}{\gamma^3}$. If $\gamma >> 1$, then the electric field cannot affect v_{bz} significantly because it is reduced by the $1/\gamma^3$ factor. If $\gamma \sim 1$, then this is no longer true, and the electric force causes the beam's velocity and magnetic pressure to decay rapidly, which can cause the filaments to expand and break apart if

filament merging is not prevalent because the beam's outward pressure cannot decrease as fast.

2.6 Magnetic and electron energy in beam-plasma system

In this section, the magnetic and plasma electron energies are calculated in terms of the beam's velocity in order to solve the equations that determine the temporal evolution of the beam presented later in this chapter. We procede by calculating these energies in the region $0 < r < r_\star$, which when multiplied by N_f yield the energies contained in the entire system (including all filaments). The azimuthal magnetic field within filaments, $\vec{B}_{\theta in}$, is found by substituting the beam density profile $n_b(r) = \widehat{n}_b/(1 + r^2/r_f^2)^2$ into the integral form of Ampere's law, yielding

$$|\vec{B}_{\theta in}| = \frac{2e\pi r_f^2 \widehat{n}_b (v_{bz}/c) r}{r^2 + r_f^2} \tag{2.26}$$

for $0 < r < r_f$. The magnetic field in the region $r_f < r < r_\star$, $\vec{B}_{\theta out}$, is estimated by summing the fields due to the filament's current contained inside of the region $r < r_f$ and plasma return current contained in the region $r_f < r < r_\star$. Using the average plasma electron velocity

$$< v_{pz} >= -n_{b0} v_{bz}/n_p \tag{2.27}$$

(from current neutrality) for v_{pz} in the region $r_f < r < r_\star$, this field is found from Ampere's law and is

$$|\vec{B}_{\theta out}| \approx 2e\pi\beta_{bz} n_{b0}(r_*^2/r - r). \tag{2.28}$$

In deriving this relation, $r_f << r_*$ was assumed. Assuming $r_f \sim c/\omega_p$, $r_f << r_*$ is valid as long as $t >> 1/\nu$, as seen from Eq. (2.19), which is true during most of the beam's evolution. The magnetic energy in the region $0 < r < r_\star$, $E_{\vec{B}} = \frac{1}{8\pi}\int_0^{r_*} \vec{B}^2 d^2x L_z$, is then calculated using Eqs. (2.26)-(2.28) to be

$$E_{\vec{B}} = \frac{k\beta_{bz}^2 e^2 N_b^2 L_z}{2}, \tag{2.29}$$

where $k = \log(\widehat{n}_b/n_{b0}) - \alpha$ and $\alpha = \log(4) - 2 \approx 1.3$. We have used the relation $n_{b0} r_\star^2 \approx N_b$ in deriving Eq. (2.29), which follows directly from the assumption that a filament's current has collected from the area $r_\star^2$.

Note that the perpendicular beam energy within a filament

$$E_{b\perp} = \int \frac{m}{2} n_b \gamma < v_{b\perp}^2 > d^2x L_z = L_z e^2 \beta_{bz}^2 N_b^2/2$$

is related to the magnetic energy $E_{\vec{B}}$ by

$$E_{b\perp} = E_{\vec{B}}/k. \tag{2.30}$$

This agrees well with simulations when the assumption of Bennett equilibrium is valid. Since k is typically greater than 1, the magnetic energy is typically greater than the transverse kinetic energy of the beam.

The plasma electron fluid energy in the region $0 < r < r_\star$, E_p, is estimated by inserting Eq. (2.27) into the energy density $\frac{1}{2} m n_p v_{pz}^2$ and then

integrating over this area. This smooths over potentially large deviations of v_{pz} from $< v_{pz} >$ in the vicinity of filaments, which is acceptable since $r_f^2 << r_\star^2$. The resulting energy of the directed motion of the plasma electron fluid is then

$$E_p = \frac{m n_{b0}^2 v_{bz}^2 \pi r_\star^2 L_z}{2 n_p} = E_{\vec{B}} \frac{4}{k \widehat{r}_\star^2}, \tag{2.31}$$

where $\widehat{r}_\star = r_\star \omega_p / c$ is typically much greater than one in resistive systems.

The energy hierarchy for the beam-plasma system is therefore $E_{\vec{B}} \sim E_{b\perp} >> E_p$. The magnetic and transverse beam energies are comparable because the magnetic pressure balances the outward thermal pressure within filaments. The relation $E_{\vec{B}} \sim E_{b\perp} >> E_p$ is true in general because filament merging in the presence of a resistive plasma produces strong increases in $E_{\vec{B}}$ and $E_{b\perp}$ as seen later while E_p decreases because the plasma is resistive.

2.7 Qualitative description of beam slowing for a filamenting beam

2.7.1 The impact of a time varying magnetic field on beam deceleration

The presence of a time varying transverse magnetic field affects the deceleration of a filamented beam in addition to deceleration caused by the finite plasma resistivity (discussed in Section 2.3). This can be understood by the following argument: depending on how rapid filament merging is, the magnetic field can either increase or decrease within filaments. According to Lenz's law, the change in magnetic field induces a longitudinal electric field

that opposes this change. This modifies the magnitude of the net longitudinal electric field compared to the case of a filamentation-suppressed beam in which there are no magnetic fields.

In the initial stages of a filamented beam's evolution, when filaments are merging rapidly, the beam density and therefore magnetic field strength increase so that the induced electric field acts to decelerate the beam. In later stages, when filaments are separated by large distances (on average) and many are isolated from each other for long periods, the magnetic field decreases as filaments are slowed by deceleration caused by the finite plasma resistivity. Therefore, in the late stages of the beam's evolution, the induced electric field acts to accelerate the beam. Deceleration is therefore enhanced in the initial stages of the nonlinear resistive WI when compared to a filamentation-suppressed beam, but is reduced in the later stages.

2.7.2 The effect of diffusion on plasma return current and beam deceleration

The solution of the diffusion equation for the plasma electron velocity can be used to explain how the plasma return current and hence decelerating electric field (related via Eq. (2.17)) are affected within beam filaments. The diffusion equation for v_{pz} is found by taking the time derivative of Eq. (2.18) and inserting Eq. (2.17). The result is the equation

$$\frac{\partial v_{pz}}{\partial t} = D\nabla^2 v_{pz} - \frac{1}{n_p}\frac{\partial (n_b v_{bz})}{\partial t}, \tag{2.32}$$

which has the solution

$$v_{pz} = v_{pz0} - \frac{1}{n_p}\int_0^t \int_{-\infty}^{\infty}\int_{-\infty}^{\infty} \frac{\partial(v_{bz}n_b)}{\partial\tau} G(\vec{x},\vec{\zeta},t-\tau)d^2\vec{\zeta}d\tau, \tag{2.33}$$

where $D = \nu c^2/\omega_p^2$ and

$$G(\vec{x},\vec{\zeta},t) = \frac{1}{4\pi Dt} e^{-|\vec{x}-\vec{\zeta}|^2/(4Dt)}.$$

v_{pz0} represents the initial plasma fluid velocity and is assumed to be uniform.

The sign of the source term $-\frac{1}{n_p}\frac{\partial(v_{bz}n_b)}{\partial t}$ depends on how rapidly filaments are merging: in the early stages when merging is dominant, n_b increases rapidly, so that this term is negative and $|v_{pz}|$ is greater within filaments than outside according to Eq. (2.33). In later stages, when the average amount of time for a filament to merge becomes large and n_b changes slowly, the decreasing beam velocity causes the source term to become positive, so that $|v_{pz}|$ is smaller within filaments than outside according to Eq. (2.33). Because $E_z \propto |v_{pz}|$, the beam's deceleration is enhanced by diffusion in the early stages of the beam's evolution and is reduced by it in the later stages.

Figure 2.4 shows simulated beam and plasma return current profiles for a group of merging filaments and an isolated filament. For the isolated filament, the return current is clearly smaller within the filament than outside, while for the merging system, the opposite is true, supporting the conclusions made in the previous paragraph. The density is lower in the bottom row of Fig. 2.4 because the filament has already begun to expand. This filament is shown at the time t_0 directly after its two 'parent' filaments merged. For $0 < t \leq t_0$ (when filaments are merging), the above 'diffusion' interpretation

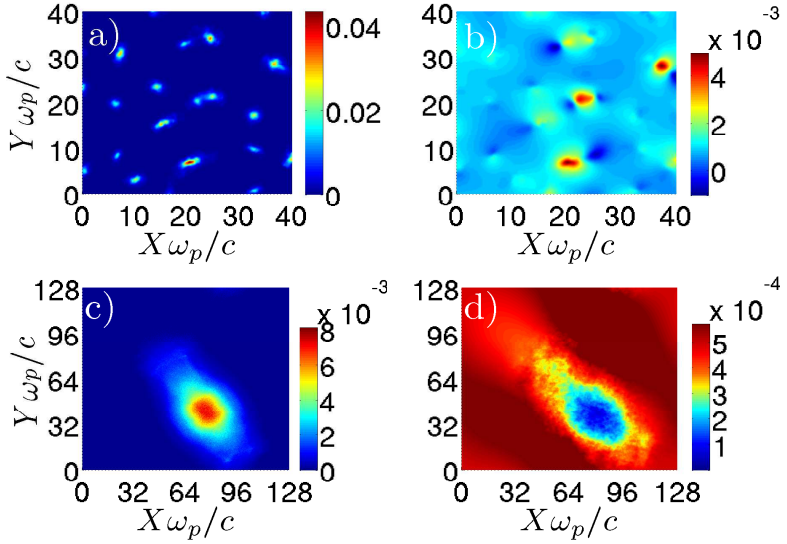

Figure 2.4: Snapshots of beam current (left column) and plasma return current (right column) density for a group of merging filaments (top row) and an isolated beam filament without filament merging (bottom row). a) and b) show $v_{bz}n_b/(n_pc)$ and $|n_pv_{pz}/(n_pc)|$, respectively at $t = 2.5 \cdot 10^3\omega_p^{-1}$; c) and d) show the same at time $t = 10^5\omega_p^{-1}$. Simulation parameters: $\gamma(t = 0) = 2.29$, $n_{b0}/n_p = 1/1000$, and $\nu = .02\omega_p$. Note: in b), the return current is greater within the filaments than outside; in d), the opposite is true.

applies, but past t_0, since the field can no longer diffuse beyond the simulation domain, the interpretation breaks down. The arguments presented in Section 2.7.1 still apply to this special case, however. Note how for the group of merging filaments, there are regions in which the return current co-propagates with the beam. This occurs when a filament migrates quickly across the transverse plane, causing the magnetic field to decrease rapidly so that $\frac{\partial \psi}{\partial t}$ and therefore the plasma electron velocity become positive according to Eq. (2.17).

Having established the qualitative basis for the role of magnetic field in the beam's deceleration due to finite plasma resistivity, the analytic description of this process is given in the next section.

2.8 Analytic calculation of beam dynamics

We proceed with the analysis of the beam's slowing down by computing the rate of energy loss of the entire system comprised of the beam and plasma's kinetic energy and the energy of the magnetic field. This energy is converted into the thermal energy of the ambient plasma. The energy loss equation is

$$\frac{\partial E'_{system}}{\partial t} = -\nu \int n_p m v_{pz}^2 d^2x L_z \approx -2\nu E'_p, \tag{2.34}$$

where $E'_{system} = E'_{beam} + E'_{\vec{B}} + E'_p$ can be rewritten in terms of v_{bz} providing the evolution equation for v_{bz}. The primes denote quantities for the entire beam-plasma system, which contains all of the beam filaments. The derivation of this equation in collisionless plasmas is discussed in Ref. [54]; it is simple to generalize it to include finite resistivity.

Assuming that γ is constant throughout a filament and that it can be calculated according to $\gamma \approx 1/\sqrt{1 - v_{bz}^2/c^2 - < v_{b\perp}^2 > /c^2}$, the energy of the beam comprising of N_f filaments is calculated by

$$E'_{beam} = \int mc^2 \gamma n_b d^2x L_z = \gamma mc^2 N_b N_f L_z = \gamma mc^2 N'_b L_z, \tag{2.35}$$

where $N'_b = N_b N_f$ is the total number of particles per unit length present in the beam. It is convenient to introduce the dimensionless variables $l_d = L_d \omega_p / c$, $\tau = t\omega_p$, $\widetilde{\nu} = \nu/\omega_p$, $\widetilde{n}_{b0} = n_{b0}/n_p$, $\beta_{bz} = v_{bz}/c$, and $\widetilde{N_b} = \omega_p^2/(c^2 n_p) N_b$. Inserting Eqs. (2.29) and (2.31) multiplied by N_f (since they represent the energies for a single filament) along with Eq. (2.35) into Eq. (2.34) and dividing by $mc^2 N'_b L_z$ yields

$$\frac{\partial(\gamma + k\beta_{bz}^2 \widetilde{N_b}/(8\pi))}{\partial \tau} = -\widetilde{\nu}\widetilde{n}_{b0}\beta_{bz}^2, \tag{2.36}$$

where $k(t) = \log(\widehat{n}_b/n_{b0}) - \alpha$. Note that $E'_p << E'_{beam}, E'_{\vec{B}}$ has been neglected. It is useful to consider this equation in two limits: a) the general case in which filaments are merging and N_b is changing with time; b) the limiting case in which filaments are isolated from each other and $N_b = constant$

2.8.1 Analytic calculation of deceleration for system of merging filaments

For a system of merging filaments, γ and $k(\widehat{n}_b/n_{b0})$ need to be written in terms of τ in order to close Eq. (2.36). γ is calculated by writing

$$\gamma = (1 - \beta_{bz}^2 - < \beta_\perp^2 >)^{-1/2} \approx (1 - \beta_{bz}^2 - \frac{\beta_{bz}^2 \widetilde{N'_b}}{\gamma N_f 4\pi})^{-1/2} \tag{2.37}$$

and solving for γ, where the normalized version of Eq. (2.25) from Bennett equilibrium has been used. Inserting N_f from Eq. (2.20) into the resulting expression for γ yields

$$\gamma \approx \frac{L\tau\beta_{bz}^2 + \sqrt{L^2\tau^2\beta_{bz}^2 + 4 - 4\beta_{bz}^2}}{2(1-\beta_{bz}^2)}, \tag{2.38}$$

where $L = \widetilde{n}_{b0}\widetilde{\nu}/\pi$.

To express $\widehat{n}_b$ as a function of time, we note that $\widehat{n}_b$ depends both on the number of the remaining filaments $N_f(t)$ and on the average filament's size $r_f(t)$. $r_f(t)$, in turn, is related to the time-evolution of the beam's temperature, T_b, and its forward moving velocity β_{bz} according to Eq. (2.23). To establish the relationship between $T_b(t)$ and $\beta_{bz}(t)$, an adiabatic assumption in which $PA^\alpha = constant$ for the entire multi-filament beam is used. Here, P is the beam pressure, $A = N_f\pi r_f^2$ is the net area occupied by the beam, and α is the adiabatic index. In two dimensions, $\alpha = 2$.

Adiabatic expansion is a reasonable assumption because plasma electron-ion collisions do not affect the transverse motion of the particles directly, and the dominant mechanism for the beam to change its transverse energy, $E_\perp$, is through the work W done by the magnetic $\vec{v} \times \vec{B}$ force on the transverse direction. This means that $dE_\perp \approx dW$, assuming that the net velocity does not change. When the net velocity does change due to damping, heat Q can flow into or out of the transverse plane, but the rate at which it is transferred is assumed to be much less than the rate at which W changes, which is true for weakly resistive plasmas. Thus, $dE/dt \approx dW/dt >> dQ/dt$, so that adiabatic expansion is a valid assumption.

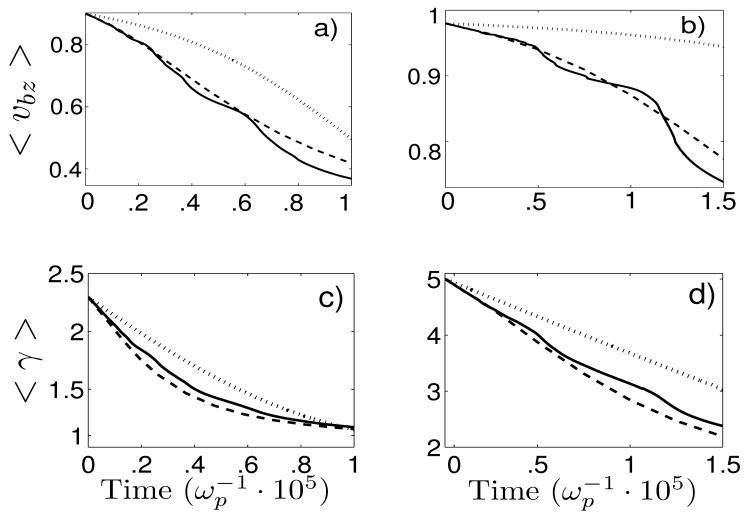

Figure 2.5: Theoretical (dashed lines) and simulated (solid lines) $< v_{bz}(t) > /c$ and $< \gamma(t) >$ curves for filamenting beams during the early stages of their filaments' merger for a mildly and strongly relativistic beam. Suppressed-filamentation curves are also plotted as dotted lines. Brackets denote average over beam's particles. Each plot has $n_{b0}/n_p = 1/1000$. Parts a) and b): $\gamma(t = 0) = 2.29$, $\nu = .02\omega_p$; Parts c) and d): $\gamma(t = 0) = 5$, $\nu = .014\omega_p$. The curves end when all of the filaments within the simulation domain stop merging consistently.

Using the identity $\widehat{n}_b = N_b'/A$, and estimating the pressure as $P \approx k_B \widehat{n}_b T_b$, the relationship $PA^2 = constant$ becomes $T_b/\widehat{n}_b = constant$. Inserting $T_b \propto \beta_{bz}^2/N_f$ into $T_b/\widehat{n}_b = constant$ gives

$$\widehat{n}_b = \frac{\kappa \beta_{bz}^2}{N_f} \ , \tag{2.39}$$

where κ is determined from the initial conditions. Note that to properly use Eq. (2.39) to calculate $\widehat{n}_b$, the relation

$$1/N_f = 1/N_{f0} + 4\nu\tau/\ell_d^2,$$

where $N_{f0} = N_f(t = 0)$, should be used instead of the expression given above for N_f. Otherwise, $\widehat{n}_b$ is not well defined at $t = 0$. Inserting this relationship into Eq. (2.39) and multiplying by N_{f0} yields

$$\widehat{n}_b = \frac{\widehat{n}_{b0}\beta_{bz}^2(1 + 4\nu\tau/r_{0*}^2)}{\beta_{bz0}^2}, \tag{2.40}$$

where $\widehat{n}_{b0} = \widehat{n}_b(t = 0)$, $\beta_{bz0}^2 = \beta_{bz}^2(t = 0)$, and $r_{0*} = r_*(t = 0)\omega_p/c$.

Inserting $\widetilde{N_b} = 4\widetilde{n}_{b0}\widetilde{\nu}\tau$ and Eq. (2.38) into Eq. (2.36) gives a dimensionless ODE for v_{bz}:

$$\frac{\partial}{\partial\tau}\left(\frac{L\tau\beta_{bz}^2 + \sqrt{L^2\tau^2\beta_{bz}^2 + 4 - 4\beta_{bz}^2}}{2(1 - \beta_{bz}^2)} + \frac{k\beta_{bz}^2 L\tau}{2}\right) = -\pi L\beta_{bz}^2, \tag{2.41}$$

where $\widehat{n}_b(t)$ is given by Eq. (2.40). The initial conditions are $\widehat{n}_{b0} = \widehat{n}_b(t = 0)$, $\beta_{bz0}^2 = \beta_{bz}^2(t = 0)$, and $r_{0*} = r_*(t = 0)$.

Figure 2.5 shows the theoretical (dashed lines: from Eq. (2.41)) and simulated (solid lines) $< v_{bz}(t) > /c$ (top row) and $< \gamma(t) >$ (bottom row) curves for two filamenting beams in the early stages of their filaments' merger. Suppressed-filamentation curves are also plotted as dotted lines, showing that deceleration for the filamenting beams is comparatively enhanced during these times. The beam energy curves for the filamenting beams generally lie below those of the suppressed-filamentation beams because a significant amount of energy is transferred from the filamenting beams to magnetic energy (which is proportional to $\frac{k\beta_{bz}^2 L\tau}{2}$). Deviations of the simulated curves from the theoretical ones are attributed to the finite number of filaments inside the simulation domain.

To show how a time varying magnetic field affects beam deceleration in support of the qualitative arguments presented in Section 2.7.1, Equation 2.36 is rewritten in the $v_{bz}^2 \sim c^2 >> \ < v_{b\perp}^2 >$ limit. This is done by combining Eq. (2.25) with the approximation

$$\gamma \approx \frac{p_{bz}}{mc} + \frac{p_\perp^2}{2p_{bz}mc} \approx \frac{p_{bz}}{mc} + \frac{\gamma < v_{b\perp}^2 >}{2c^2} \tag{2.42}$$

and inserting into Eq. (2.36). The result is the relation

$$\frac{\partial(\gamma v_{bz}/c)}{\partial\tau} \approx -\widetilde{\nu}\widetilde{n}_{b0}\beta_{bz}^2 - \frac{1}{2\pi}\frac{\partial[(k+1)\beta_{bz}^2\widetilde{n}_{b0}\widetilde{\nu}\tau]}{\partial\tau}. \tag{2.43}$$

The second term on the right hand side, $E_{eff} = -\frac{1}{2\pi}\frac{\partial[(k+1)\beta_{bz}^2\widetilde{n}_{b0}\widetilde{\nu}\tau]}{\partial\tau}$, is due to the effect of the time varying magnetic field discussed in Section 2.7.1 and also change in the transverse beam energy. E_{eff} is negative (positive) so that deceleration is enhanced (reduced) by E_{eff} when the condition $\frac{1}{2}\beta_{bz} > t|\frac{\partial\beta_{bz}}{\partial t}|$ is true (false). Solutions to Eq. (2.41) show that this condition holds until time $t \approx \tau_r/2$- past this time, the condition is violated. Taking $E_{eff} = 0$ yields the dynamics for a filamentation-suppressed beam since there are no magnetic fields or beam thermalization in the 0-D system. The deceleration of a filamenting beam is therefore enhanced in comparison to a filamentation-suppressed beam during the first half of its evolution and is reduced in the second half.

We now examine the energy loss rate of a relativsitic beam using Eq. (2.36). First, we study the loss rate during early times in which $\frac{1}{2}\beta_{bz} > t|\frac{\partial\beta_{bz}}{\partial t}|$ holds. Using $\widetilde{N_b} = 4\widetilde{n}_{b0}\widetilde{\nu}\tau$, neglecting the time derivative of $k(t)$ since it has weak logarithmic dependence, and assuming a sufficiently relativistic beam

that we can take $\beta_{bz} \approx 1$ and neglect β_{bz}'s time derivative, we conclude in early times that

$$\frac{\partial \gamma}{\partial \tau} \sim -\widetilde{n}_{b0}\widetilde{\nu}[1 + k(t)/(2\pi)]. \tag{2.44}$$

$k(t)/(2\pi)$ is typically of order 1 and is due to energy transfer of the beam into the magnetic field during filamentation. For the 0-D system without filamentation, the loss rate scales as

$$\frac{\partial \gamma}{\partial \tau} \sim -\widetilde{n}_{b0}\widetilde{\nu} \tag{2.45}$$

during early times for relativistic beams. Equations (2.44, 2.45) indicate that the loss rate is enhanced by approximately a factor of 2 during the early stage propagation of a filamenting beam, which is supported by Fig. 2.5. The scaling for the energy transfer rate becomes more complicated during later times in which $\frac{1}{2}\beta_{bz} > t|\frac{\partial \beta_{bz}}{\partial t}|$ holds, and we must either numerically solve Eq. (2.41) or simulate the beam's evolution to determine the loss rate during this stage.

2.8.2 Analytic calculation of isolated filament deceleration

In this section, Eq. (2.36) is solved in the $N_b = constant$ limit in which filaments are effectively isolated from each other. This is done to better understand why deceleration for a filamented beam in the presence of the resistive WI is reduced in the later stages of its evolution when compared to a filamentation-suppressed beam. The $N_b = constant$ limit is valid during the late stages of a beam's evolution in which filaments are separated by large distances and the expected time for a given filament to merge is large. Note

how in this limit, E_{eff} is always positive, so that deceleration is weaker than the filamentation-suppressed beam.

To solve Eq. (2.36) with $N_b = constant$, β_{bz} is written in terms of γ by solving Eq. (2.37) for $\beta_{bz}(\gamma)$. The result is the relation

$$\beta_{bz}^2 = (\gamma^2 - 1)/(\gamma^2 + \frac{\widetilde{N_b}}{4\pi}\gamma).$$

Inserting this into Eq. (2.36), dividing by β_{bz}^2, and multiplying by $d\tau$ yields

$$\frac{\gamma^2 + \frac{\widetilde{N_b}}{4\pi}\gamma}{(\gamma^2 - 1)}d\gamma + k\widetilde{N_b}\frac{d\beta_{bz}^2}{8\pi\beta_{bz}^2} = -d\tau\widetilde{\nu}\widetilde{n}_{b0}. \tag{2.46}$$

Integrating this equation gives the solution

$$\gamma - \text{arctanh}(\gamma) + \tfrac{1}{8\pi}\widetilde{N_b}\ln(\gamma^2 - 1) + \tfrac{k\widetilde{N_b}}{8\pi}\ln(\tfrac{\gamma^2-1}{\gamma^2+\frac{\widetilde{N_b}}{4\pi}\gamma}) = -\tau\widetilde{\nu}\widetilde{n}_{b0} + K,$$

where K is determined from the initial conditions. γ can then be related to β_{bz} through the above relation.

Figure 2.6 displays the simulated (solid lines) and analytical (dashed lines generated from the above relation) $< v_{bz}(t) >$ and $< \gamma(t) >$ curves for two thermalized, isolated filaments propagating through a resistive plasma. The filaments have collected from an initially uniform beam of density $n_{b0}/n_p = 1/1000$ upon its filamentation and subsequent merger of all filaments. The curves for filamentation-suppressed beams of density n_{b0} with the same initial energies and fixed transverse energies are plotted as dotted lines. The system parameters are given in the figure description. Deceleration for the isolated filaments is clearly reduced when compared to the filamentation-suppressed

beams, and the analytic model agrees well with the simulated results in parts b) and d) until the filaments begin to break apart and the assumption of Bennett pinch equilibrium becomes invalid. No analytic curves are presented for parts a) and c) because the filament is expanding and the model does not not apply to an isolated, expanding filament.

The beam energy E_{f-s} for the filamentation-suppressed beam is lower than the beam energy E_f for the isolated filament in Fig. 2.6 d) because the magnetic field helps to supply energy into the filament. E_{f-s} is typically higher than E_f in Fig. 2.6 c) because the filamentation-suppressed beam has fixed transverse energy. Because beam velocities are decoupled at these energies, this does not impact longitudinal deceleration, and the isolated filament's velocity decays at a slower rate than the filamentation-suppressed beam's because the decelerating electric field is smaller for the filamented case.

2.8.3 Calculation of beam propagation stopping time

Equation (2.36) rewritten as

$$\frac{\partial(\gamma + E'_{\vec{B}}/(N'_b L_z mc^2))}{\partial\tau} = -\widetilde{\nu}\widetilde{n}_{b0}\beta_{bz}^2$$

is used to calculate the time at which the beam stops propagating, τ_{stop}. Integrating this equation from time $\tau = 0$ to $\tau = \tau_{stop}$ yields

$$\gamma_0 - \gamma_f = \widetilde{\nu}\widetilde{n}_{b0} < \beta_{bz}^2 >_\tau \tau_{stop}, \tag{2.47}$$

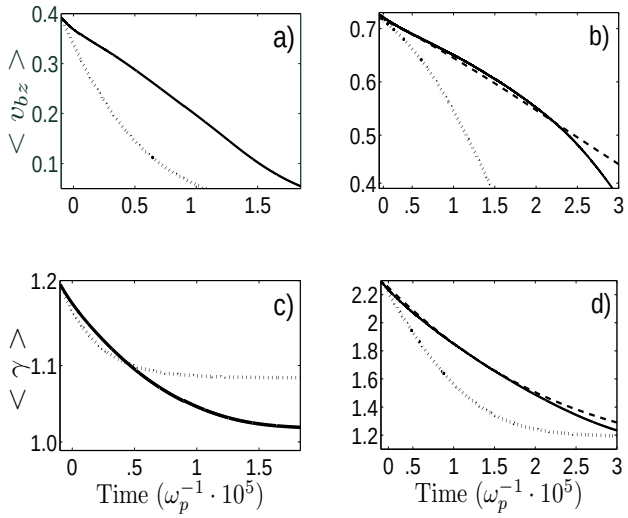

Figure 2.6: Theoretical (dashed lines) and simulated (solid lines) $< v_{bz}(t) > /c$ and $< \gamma(t) >$ curves for isolated beam filaments (no filament merging). Filaments have collected from initially uniform beam of density $n_{b0}/n_p = 1/1000$ upon its filamentation and subsequent merger of all filaments. Dotted lines-filamentation-suppressed beam of density n_{b0} with fixed transverse beam energy (same as initial transverse energy of the isolated filaments). Parts a) and c): $\gamma(t = 0) = 1.2$, $\nu = .02\omega_p$; Parts b) and d): $\gamma(t = 0) = 2.2$, $\nu = .014\omega_p$. No analytic curves are presented for parts a) and c) because the model does not not apply to expanding filaments.

where

$$< \beta_{bz}^2 >_\tau = \frac{\int_0^{\tau_{stop}} \beta_{bz}^2(\tau')d\tau'}{\tau_{stop}}$$

is the time average of β_{bz}^2 throughout the entire evolution of the beam, and $\gamma_0 = \gamma(\tau = 0)$ and $\gamma_f = \gamma(\tau = \tau_{stop})$. The magnetic energy does not appear explicitly in Eq. 2.47 because it is zero initially and is zero at τ_{stop} since the beam's longitudinal velocity and plasma electron velocity are both zero at this time (they must be in order to maintain current neutrality). The magnetic energy does, however, affect $< \beta_{bz}^2 >_\tau$. Solutions of Eq. (2.41) for >MeV beams show that if the maximum amount of magnetic and transverse beam energy generated during the beam's evolution is artificially removed from the beam's longitudinal energy initially, then v_{bz} remains close to c. This, combined with the fact the beam's velocity decays rapidly when $\gamma \sim 1$ (discussed in Section 2.5), implies that the beam cannot spend a significant amount of time at low velocities during its evolution. Therefore, for MeV beams with $\gamma >> 1$, the beam's longitudinal velocity is typically close to c and $< \beta_{bz}^2 >_t \sim 1$.

In general, the beam can have transverse energy at $\tau = \tau_{stop}$, but solutions of Eq. (2.41) show that the maximum possible transverse kinetic energy throughout the beam's evolution is small enough that $\gamma_f \approx 1$. The total amount of time for the beam to stop propagating for $\gamma_0 >> 1$ is therefore approximately

$$\tau_{stop} \approx \frac{\gamma_0}{\widetilde{\nu}\widetilde{n}_{b0}}, \tag{2.48}$$

or in dimensional units $t_{stop} = \frac{n_p \gamma_0}{n_{b0} \nu}$, which is the same as the stopping time of the filamentation-suppressed beam.

2.9 Summary

This chapter has demonstrated that the resistive WI enhances beam deceleration at first when compared to a filamentation-suppressed beam, but eventually reduces it, so that the net stopping time is essentially unaffected by the WI in the underdense beam limit. This is due to the fact that an electric field is induced before (after) time $t \approx \tau_r/2$ (about halfway through the beam's evolution) by an increasing (decreasing) magnetic field within filaments that acts to enhance (reduce) the deceleration of the filamented beam, respectively. A novel theoretical model has been presented that supports these statements and accurately calculates the dynamics of a filamenting beam during the non-linear stage of the resistive WI. Using this model, we analytically demonstrated that the energy transfer of a filamenting beam into the magnetic field increases the beam's energy loss rate during early times (when the energy content of the beam is most important) by approximately a factor of two in comparison to a filamentation-suppressed beam. This conclusion was supported by both numerical solutions and simulation. The model was also used to calculate the net stopping time for the beam in the presence of the resistive WI, which is approximately

$$t_{stop} \approx \gamma(t=0) n_{p0}/(n_{b0}\nu) -$$

about the same stopping time as a filamentation-suppressed beam.

This work was supported by the US DOE grant DE-FG02-05ER54840 and the 2008 NDSEG Fellowship award.

Chapter 3

Laser-seeded modulation instability in a proton driver plasma wakefield accelerator

3.1 Introduction and Motivation

[1] The past decade witnessed tremendous advances in plasma based particle acceleration [20, 27]. 100 MeV to 2 GeV accelerated electrons have been reported using either laser [23, 24, 25, 70, 71, 72] or particle beams [28, 30, 39, 73] as the driver. To achieve higher electron energies with a laser driver, improvements in power, focusing, and repetition rate are required. In particle-beam driven plasma wakefield accelerators (PWA) [27], the maximum energy gain of the witness bunch is restricted by the transformer ratio limit, which roughly states that a witness bunch's energy cannot exceed twice the driver bunch's energy [38].

To achieve unprecedented electron beam energies in the TeV range, TeV proton beams from CERN's Large Hadron Collider (LHC) have been proposed as a driver in a proton driver plasma wakefield acclerator (PDPWA) [34, 35].

[1] This chapter was previously published in the work *C. Siemon, V. Khudik, S. A. Yi, A. Pukhov, and G. Shvets, Physics of Plasmas* **20,** *103111 (2013).* Vladimir Khudik, S. Austin Yi, and Alexander Pukhov provided supporting work, and Gennady Shvets was the supervisor.

In order to efficiently excite plasma waves that produce large accelerating gradients, the driver beam should be of order one plasma wavelength, $\lambda_p \equiv 2\pi c/\omega_p$, where $\omega_p = \sqrt{4\pi e^2 n_{p0}/m_e}$ is the plasma frequency, c is the speed of light, $n_{p0} \sim 10^{15}\text{cm}^{-3}$ is the density of the unperturbed plasma, $-e$ and m_e are the electron charge and mass, respectively. However, for the plasma with $n_{p0} \sim 10^{15}\text{cm}^{-3}$ and wave-breaking field $E_{\text{WB}} = mc\omega_p/e \sim$1GV/m, the corresponding plasma wavelength $\lambda_p \sim$ 1mm is much shorter than the r.m.s length $\sigma_z \sim$ 10cm of the proton beams at the LHC. The proposed solution [41, 42] to this length scale mismatch is to rely on the modulation instability (MI) of a long proton bunch with $\sigma_z \gg \lambda_p$. The MI perturbs the proton bunch density with the spatial period equal to λ_p and resonantly excites the plasma wake, thereby producing a strong plasma wakefield. But as any linear instability, the MI needs to be initialized (seeded).

One recently proposed seeding method is to 'hard-cut' the proton beam in the longitudinal direction [42] by creating a co-propagating ionization front via a laser pulse within the beam as it propagates through an initially neutral gas, leading to a sharp transition in the plasma density [77]. A second method is to hard-cut using a 'dog-leg' device [76] in a pre-ionized plasma, creating a very sharp and large proton bunch density transition at its head. To avoid confusion with the seeding method proposed below, we mainly consider the latter method throughout this chapter. The density jump created by the dog-leg device excites a plasma density perturbation $\delta n_p \sim \hat{n}_b$ throughout the proton beam, where $\hat{n}_b$ is the density of the beam at the position of the cut. The MI

seeded by this perturbation undergoes an exponential spatio-temporal amplification as the proton bunch advances through the plasma [42, 83, 84]. Technologically, such abrupt termination of the beam is difficult to accomplish. Here we propose an alternative approach: to use a short (picosecond-scale) strongly focused laser pulse traveling in front of the proton bunch to produce a plasma wave in its wake. This method assumes a pre-ionized plasma which extends the variety of usable plasma sources in comparison to the hard-cut seeding scheme that involves a co-propagating ionization front. Although the laser pulse rapidly diffracts after propagating for a distance of order its Rayleigh range $z_R = \pi w_0^2/\lambda_L$, where w_0 is the laser spot size and λ_L is the laser wavelength, the resulting transient plasma wake can produce sufficient compression of the proton bunch to seed the MI. Naturally, because the seeded bunch compression is produced by the plasma wake, its spatial period is equal to λ_p and can be further amplified by the MI. The two instability seeding approaches are schematically shown in Fig. 3.1.

While the concept of laser-seeded modulational instability of a proton bunch in the plasma is quite straightforward, there are several technical issues that need to be addressed. First, the seed produced by the laser must be comparable to that produced by the hard-cut beam to be competitive. Second, the required laser intensity must be low enough so as not to produce any secondary ionization of the gas Rubidium vapor, which is the planned plasma source for the PDPWA experiments at the LHC's Super Proton Synchrotron (SPS) [74]. Higher plasma density during the transient period of laser wakefield

generation would result in seeding the bunch's compression with a mismatched spatial period corresponding to higher plasma density. Finally, for the sake of designing a constant gradient plasma wakefield accelerator, it is important to ensure that the amplitude of the saturated laser-seeded MI can be stabilized at a constant value for very long propagation distances. Addressing these issues is the main objective of this chapter.

Specifically, we demonstrate that it is more advantageous to use a laser pulse produced by a CO_2 laser ($\lambda_L \approx 10\mu$m) rather than by a solid state laser ($\lambda_L \approx 1\mu$m). In a nutshell, for a laser pulse with peak intensity I_L whose duration $c\tau_L \sim \lambda_p/2$ and spot size $w_0 \sim \sigma_r$ are matched to the plasma period and proton bunch's spotsize σ_r, the strength of the plasma wakefield is proportional to its ponderomotive potential $\phi_p \propto \lambda_L^2 I_L$. Assuming that the laser intensity is limited by the ionization potential of the gas, stronger wakefields favor longer laser wavelengths. This conclusion holds even when the shorter Rayleigh range of a CO_2 laser is taken into account. Recent advancements in CO_2 laser technology [87, 88] have led to the development of terawatt scale picosecond laser systems that match the requirements of a laser-seeded PDPWA and produce accelerating fields comparable to those generated by hard-cut seeding of the MI.

The rest of the chapter is organized as follows. Section 3.2 introduces the equations governing the excitation of the plasma wakefields, the transverse dynamics of the protons, and the evolution of the laser pulse. Laser ionization of the gas is also examined. In Sec. 3.3, the proton bunch dynamics is simplified

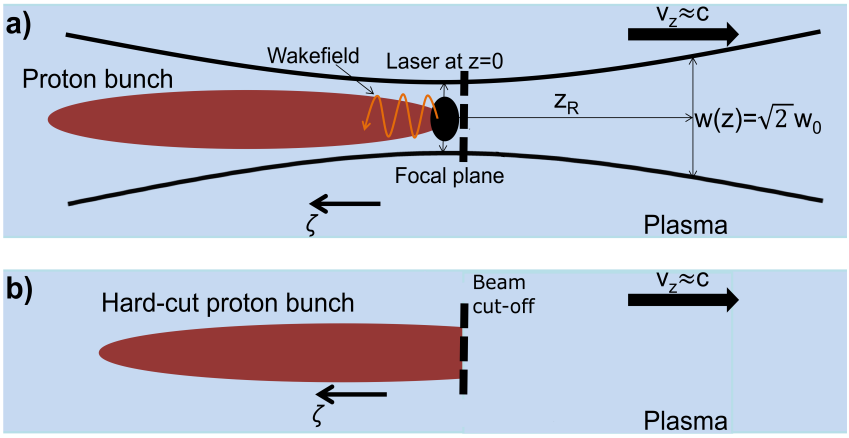

Figure 3.1: Schematic representation of laser (a) and hard-cut (b) modulation instability (MI) seeds. $\zeta = ct - z$ is the co-moving coordinate that measures the distance from the beam's head located at the vertical dashed lines. Laser is shown in black, proton beam in red, and plasma in blue.

by introducing the envelope equation for the beam's r.m.s radius. This simplified formalism is used to analytically describe the linear stage of the hard-cut and laser wakefield seeding of the MI. Comparisons between the results obtained using the envelope description of the protons with direct particle-in-cell (PIC) modeling of the protons is presented in Sec. 3.4 for both MI seeding techniques. It is also shown that a density ramp of the plasma can be used to stabilize the laser-seeded MI and create a quasi-equilibrium accelerating electric field of order 100MV/m which is sustained over long propagation distances.

3.2 Theoretical Formalism and Simplifying Assumptions

An important simplifying assumption used throughout this chapter is that only the transverse dynamics of the proton beam in response to the plasma wakefield needs to be taken into account to describe the MI. This assumption is valid as long as the proton beam's relativistic factor $\gamma = 1/\sqrt{1-(v_{bz}/c)^2}$, where v_{bz} is the proton beam's longitudinal velocity, is ultra-relativistic: $\gamma \gg 1$. One consequence of this assumption is that the protons are moving with the longitudinal velocity essentially equal to the speed of light and that the linear density of the proton bunch $\lambda(\zeta)$, where $\zeta = ct - z$ is the co-moving (with the bunch) coordinate, does not depend on the propagation distance z into the plasma.

The transverse dynamics of the i^{th} proton of mass m_p is then given by the following equation:

$$c\frac{\partial}{\partial z}\left(\gamma_i m_p v_\perp^{(i)}\right) = F_\perp^{(i)}, \tag{3.1}$$

where $\vec{F}_\perp^{(i)} = e\vec{W}_\perp^{(i)}$ is the transverse force exerted by the plasma wakefield $\vec{W}_\perp = e\vec{E}_\perp + e\widehat{z} \times \vec{B}_\perp$ on the proton, and $v_\perp^{(i)}$ is its transverse velocity. As derived in Section 1.4, the longitudinal component of the electric field E_z as well as the transverse component of the electric field $\vec{W}_\perp$ experienced by the proton bunch can be expressed as the gradients of the effective wake potential ψ:

$$E_z = -\partial_\zeta \psi, \vec{W}_\perp = \vec{\nabla}_\perp \psi, \tag{3.2}$$

where ψ is determined [43, 49, 78] solely by the plasma density perturbation

δn_p according to

$$\left(\nabla_\perp^2 - k_p^2\right)\psi = -4\pi e \delta n_p. \tag{3.3}$$

Here, $k_p \equiv \omega_p/c$ the plasma wavenumber.

It will be further assumed that the beam hosing instability [43, 44, 45] can be neglected, and all relevant beam and plasma quantities are azimuthally symmetric, i. e. are functions of the co-moving variable ζ, radial variable r, and the propagation variable z. For example, $n_{p,b} \equiv n_{p,b}(\zeta, r, z)$. In the thin proton driver limit of $\sigma_r \ll k_p^{-1}$, the transverse (radial) component of the wake $W_r \equiv \partial_r \psi$ is given by

$$W_r(\zeta, r, z) = -\frac{4\pi e}{r}\int_0^r dr' r' \delta n_p(\zeta, r', z), \tag{3.4}$$

which considerably simplifies the theoretical analysis presented in Section 3.3. The slightly more involved calculation of E_z in the thin bunch limit is carried out in Sec. A. Here, we present for reference the expression for the axial (accelerating) electric field $E_z^{axial} \equiv E_z(r = 0)$ without a derivation (see Appendix A):

$$E_z^{axial} = 4\pi e \frac{\partial}{\partial \zeta}\int_0^\infty dr' r' \ln\left(k_p r'\right)\delta n_p. \tag{3.5}$$

Although E_z is not needed for modeling the protons' dynamics, it needs to be calculated behind the proton bunch in order to evaluate the peak accelerating field of the PDPWA.

Throughout this chapter, another simplifying assumption is made: that the response of the ambient cold plasma is linear. Then, as derived in Section

1.4, the excitation of the plasma wave perturbation δn_p is given by the following linear equation [49, 79, 80]:

$$\frac{\partial^2 \delta n_p}{\partial \zeta^2} + k_p^2 \delta n_p = k_p^2 n_b + n_{p0} \nabla^2 \left(\frac{|a|^2}{4} \right), \tag{3.6}$$

where $|a| = e|\vec{E}_L|/(m_e c \omega_L)$ is the laser's normalized magnetic vector potential and $\omega_L \equiv 2\pi c/\lambda_L$ is the laser's angular frequency. Throughout this chapter, we assume $n_{p0} = 7 \cdot 10^{14} \text{cm}^{-3}$, which corresponds to $k_p^{-1} = .2\text{mm}$. These values are motivated by those of the planned PDPWA experiments at the SPS [81].

The linear approximation of the plasma wave enables the analytic calculation presented in the Section 3.3 and greatly simplifies the numerical modeling of the MI described in the Section 3.4. This is because it reduces the computationally intensive kinetic modeling of the plasma to solving Eq. (3.6) in quadratures. The physical basis for this approximation is provided by assuming (i) an initially underdense proton bunch with the peak on-axis density $n_{b0} \ll n_p$, (ii) weakly-relativistic laser amplitude $|a| \ll 1$, and (iii) modest r.m.s longitudinal bunch length σ_z. The latter assumption will be justified *a posteriori* by examining the saturation amplitude of the MI and ensuring that $|\delta n_p| \ll n_{p0}$ throughout the proton beam for long propagation lengths. As demonstrated in Section 3.4, this restricts the validity of the linear approximation to beam lengths that are roughly $2 - 3$ times shorter than the $\sigma_z \approx 12\text{cm}$ typical of the beams generated at the SPS [82, 93]. However, our demonstration of the laser-seeded MI using these shorter beams is still valid as a proof principle.

Equation (3.6) can be solved in quadratures. To simplify the solution, we choose $\zeta = 0$ to either (a) coincide with the abrupt beam cut-off or other density discontinuity of the proton bunch, or (b) to be immediately in front of the seeding laser pulse such that $|a_L| = 0$ for $\zeta < 0$. Then the leading portion of the proton bunch located at $\zeta < 0$ can be assumed non-evolving, and the expression for $\delta n_p(\zeta > 0, r, z)$ can be expressed as the sum of three density perturbation terms: $\delta n_p = N_p^{(b)}(\zeta, r, z) + N_p^{(L)}(\zeta, r, z) + N_p^{(i)}(r, \zeta)$, where

$$N_p^{(b)} = k_p \int_0^\zeta d\zeta' \sin[k_p(\zeta - \zeta')] n_b(\zeta', r, z) \tag{3.7}$$

is induced by the portion of the evolving beam located in the $\zeta > 0$ region,

$$N_p^{(L)} = n_{p0} \int_0^\zeta d\zeta' \sin[k_p(\zeta - \zeta')] \nabla^2 \left(\frac{|a|^2}{4k_p} \right) \tag{3.8}$$

is induced by the diffracting laser pulse, and

$$N_p^{(i)} = \cos(k_p\zeta)\delta n_p(\zeta = 0) - \frac{\sin(k_p\zeta)}{k_p} \frac{\partial \delta n_p}{\partial \zeta}(\zeta = 0) \tag{3.9}$$

is induced by the leading (non-evolving) portion of the proton bunch. The assumption of the non-evolving leading portion of the beam implies that it is charge-neutralized by the plasma and self-focused by its own magnetic field in such a way that its emittance, radius, and density are matched to enable $z-$independent propagation. A trivial case of the non-evolving leading portion of the beam arises when there are no protons at all for $\zeta < 0$, i.e. the hard-cut case. The boundary conditions $\delta n_p|_{\zeta=0}$ and $\partial_\zeta \delta n_p|_{\zeta=0}$ are chosen depending which of these two cases is under consideration.

Finally, we introduce several assumptions about the evolution and intensity of the laser pulse. First, we assume that the laser amplitude a_0 and spotsize w_0 in the focal plane are such that its power given by $P = (\pi/2)(w_0/1\text{mm})^2(a_0/.85)^2(1\mu\text{m}/\lambda_L)^2 10^{16}\text{W}$ is much smaller than the critical power for relativistic self-focusing $P_{crit} = (16.2\text{ GW})\times\omega_L^2/\omega_p^2$. The intensity of such a laser pulse evolves as if in vacuum according to

$$|a|^2 = a_0^2(w_0/w(z))^2 e^{-2r^2/w(z)^2} e^{-(\zeta-\zeta_c)^2/(\sqrt{2}\sigma_z^L)^2}, \tag{3.10}$$

where σ_z^L is the pulse's longitudinal r.m.s length, $\zeta_c > 0$ is the ζ value at which $|a|$ is maximized, $w(z) \equiv w_0\sqrt{1+(z-z_{focal})^2/z_R^2}$ is the evolving pulse's spotsize. Second, we assume that the laser pulse diffracts rapidly enough to make the phase slippage between the proton beam (moving essentially at the speed of light) and the pulse (moving with a slower group velocity $v_g/c \approx 1-\lambda_L^2/(2\pi w_0)^2-\omega_p^2/\omega_L^2$ [94]) small: $z_R(1-v_g/c) \ll k_p^{-1}$. Finally, it is assumed that the maximal slippage between the plasma waves created by the laser pulse and proton beam a distance $\zeta_{max} \sim 100\lambda_p$ from the laser pulse is also negligible: $(1-v_g/c)\zeta_{max} \ll \lambda_p/2$.

It will be further assumed that the peak laser intensity is smaller than required for producing secondary ionization of Rb vapor, which is the planned plasma source for the PDPWA experiments at the SPS [74]. Figure 3.2 shows the ionization level n_{p0}/n_{p0}^{max} of Rubidium vapor calculated using the ADK model [91] for the laser parameters given in the caption for two laser wavelengths: $\lambda_L = 10\mu$m (top panel) and $\lambda_L = 1\mu$m (bottom panel).

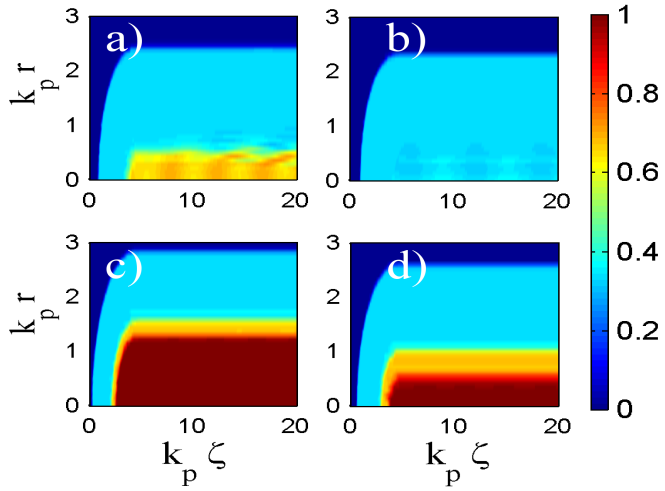

Figure 3.2: Ionization level n_{p0}/n_{p0}^{max} of Rubidium vapor for different laser parameters. Parts (a) and (b): $a_0 = .2$ and $a_0 = .15$, respectively, for a $\lambda_L = 10\mu$m laser. Parts (c) and (d): $a_0 = .06$ and $a_0 = .03$, respectively, for a $\lambda_L = 1\mu$m laser. Light blue: single ionization state of Rb, yellow/red: second/third states. Laser pulse is centered at $\zeta_c = 4.3k_p^{-1}$, has $\sigma_z^L = k_p^{-1} =$ .2mm and spotsize $w(z) =$ .28mm, and is propagating to the left. Laser intensities greater than $I_{max} \sim 5.5 \cdot 10^{14}$W/cm^2 lead to significant secondary ionization.

The laser pulse is propagating from right to left. The ADK model is used to calculate the Rubidium atom's ionization probability as a function of the laser's intensity $I_L \propto a_0^2/\lambda_L^2$, which is then used to calculate $n_{p0}(\zeta, r)$. Here, $n_{p0}^{max} = 2.1 \cdot 10^{15}\text{cm}^{-3}$ is the density of triply-ionized Rb vapor. The light blue regions correspond to first level ionization while the yellow and red regions correspond to secondary and tertiary ionization, respectively. According to the ADK model, laser intensities exceeding $I_{max} \sim 5.5 \cdot 10^{14}\text{W/cm}^2$ result in substantial secondary ionization.

The comparison between ionization plots for the two laser wavelengths shown in the Fig. 3.2 indicates that a $\lambda_L = 10\mu$m laser can have significantly higher (by at least a factor 5) values of a_0 than a $\lambda_L = 1\mu$m laser without producing secondary ionization. According to Eq. (3.6), the strength of the laser wake is proportional to a_0^2. Therefore, a CO_2 laser with $\lambda_L \approx 10\mu$m is better suited to seed the MI than a solid-state laser with $\lambda_L \approx 1\mu$m even after the shorter Rayleigh range of the former is taken into account. For the remainder of this chapter, we assume that $\lambda_L = 10\mu$m and $a_0 = .1$, thereby ensuring that the peak laser intensity is below I_{max} and no secondary ionization by the laser is expected according to Fig. 3.2(b). The unperturbed plasma density $n_{p0} = 7 \cdot 10^{14}\text{cm}^{-3}$ will be assumed throughout the rest of the chapter.

Under the stated above assumptions, the full kinetic modeling of the MI can be numerically carried through the following steps: (a) calculating the proton bunch density $n_b(\zeta, r, z)$ using numerical macro-particles emulating the protons; (b) calculating $\delta n_p(\zeta > 0, r, z)$ from Eqs. (3.7,3.8,3.9); (c) calculat-

ing the wake potential $\psi(\zeta, r, z)$ and the transverse force $W_\perp$ calculated from Eqs. (3.2,3.3) using δn_p obtained in the previous step, and (d) advancing the numerical macro-particles along the propagation distance z according to Eq. (3.1). This full kinetic modeling is described in Sec. 3.4. Below we simplify the treatment of the proton bunch by assuming that it retains its Gaussian radial profile in every cross section $\zeta = \text{const}$ for all propagation distances z, and by further assuming that its radius remains smaller than the plasma skin depth: $r_b(\zeta, z) \ll k_p^{-1}$.

3.3 Envelope description for an ultra-thin proton beam driver

To analytically model the proton beam's evolution, we use the envelope equation [92] for its r.m.s radius, $r_b(\zeta, z)$. We assume that the beam focal spot is at the plasma's entrance at $z = 0$ and, therefore, $r_b(\zeta, z = 0) = \sigma_r$, where σ_r is the initial radius. A self-similar azimuthally symmetric Gaussian density ansatz is assumed:

$$n_b(\zeta, r, z) \equiv \frac{\lambda(\zeta)}{\pi r_b^2(\zeta, z)} e^{-r^2/r_b^2(\zeta,z)}, \tag{3.11}$$

where $\lambda(\zeta)$ is a non-evolving but, in general, non-uniform linear density of the proton bunch. Throughout this section it will be assumed that $\lambda(\zeta > 0) \equiv \lambda = \pi n_{b0} \sigma_r^2$ is constant in every cross section of the beam, where n_{b0} is the beam's initial maximal density. The normalized emittance of the proton bunch $\epsilon_n \equiv \gamma \sigma_r \sigma_\theta$ is proportional to σ_r and its initial angular divergence σ_θ. Although σ_r and σ_θ are determined by the beam's injector, we further assume

that a charged-neutralized beam remains in equilibrium in the plasma due to its own magnetic self-focusing. Therefore, the relevant betatron frequency of the proton bunch in the plasma is given by $\omega_\beta = \sqrt{4\pi e^2 n_{b0}/\gamma m_p}$ is the betatron frequency of the proton beam. The MI develops [42] over a typical scale on the order of the proton beam's betatron length $k_\beta^{-1} \equiv c/\omega_\beta \approx 4.2$m.

The envelope equation for the radius of a proton bunch [92] is given by

$$\frac{\partial^2 r_b}{\partial z^2} = \frac{\epsilon_n^2}{\gamma^2 r_b^3} + \frac{e}{\gamma m_p c^2 r_b}\langle r W_r \rangle, \tag{3.12}$$

where the brackets denote the radial averaging operation, i. e. $\langle A(r)\rangle = (2/r_b^2)\int_0^\infty dr\, r \exp\left(-r^2/r_b^2\right) A(r)$ for an arbitrary function $A(r)$. Using the simplified expression for the radial wake W_r given by Eq. (3.4) and inserting δn_p from Eqs. (3.7,3.8,3.9), we obtain the transverse wake $W_r = W^{(b)} + W^{(i)} + W^{(L)}$ as the sum of separate contributions of the trailing (perturbed) portion of the proton bunch located at $\zeta > 0$,

$$W^{(b)} = -\frac{2ek_p\lambda}{r}\int_0^\zeta d\zeta' \left(1 - e^{-r^2/r_b^2(\zeta')}\right)\sin[k_p(\zeta - \zeta')], \tag{3.13}$$

of the leading portion of the proton bunch located at $\zeta < 0$ expressed as the boundary conditions $\delta n_p(\zeta = 0, r)$ and $\partial_\zeta \delta n_p(\zeta = 0, r)$,

$$W^{(i)} = -\frac{4\pi e}{r}\int_0^r dr' r' N_p^{(i)}, \tag{3.14}$$

and of the laser pulse's wake,

$$W^{(L)} = \frac{\pi^{3/2} e n_{p0} a_0^2}{2\sqrt{2} k_p r}\sigma_z^L e^{-k_p^2 \sigma_z^{L2}/2} P_L(r, z)\sin k_p(\zeta - \zeta_c). \tag{3.15}$$

Here the diffracting radial profile is given by

$$P_L(r,z) = 16\frac{w_0^2 r^2}{w^4(z)} e^{-2r^2/w^2(z)} + k_p^2 w_0^2 \left(1 - e^{-2r^2/w^2(z)}\right), \tag{3.16}$$

and the boundary condition function $N_p^{(i)}(r,\zeta)$ given by Eq. (3.9) describes the transversely non-uniform plasma perturbation produced by the leading (unperturbed) portion of the proton bunch.

For simplicity, and as justified below in the Section 3.3.1, we assume the following initial conditions determined by the density profile of the leading portion of the bunch: $\partial_\zeta \delta n_p(r)|_{\zeta=0} = 0$ and $\delta n_p(r)|_{\zeta=0} = \kappa n_{b0} \exp(-r^2/\sigma_r^2)$, where $0 < \kappa < 1$ is a real number. Under this assumption, the envelope equation becomes:

$$\begin{aligned}\frac{\partial^2 r_b}{\partial z^2} =& \frac{\epsilon_n^2}{\gamma^2 r_b^3} - \kappa \frac{\cos(k_p\zeta) k_\beta^2 \sigma_r^2}{2} \frac{r_b}{\sigma_r^2 + r_b^2} \\ &- \frac{k_\beta^2 k_p \sigma_r^2}{2} \int_0^\zeta d\zeta' \frac{r_b(\zeta) \sin k_p(\zeta - \zeta')}{r_b^2(\zeta') + r_b^2(\zeta)} \\ &+ \left[\frac{a_0^2 G_L(z) q_z^L n_{p0}}{n_{b0}}\right] k_\beta^2 r_b \sin k_p(\zeta - \zeta_c),\end{aligned} \tag{3.17}$$

where $q_z^L \equiv k_p \sigma_z^L \exp -(k_p \sigma_z^L)^2$ is the longitudinal form-factor of the laser pulse maximized for $\sigma_z^L = k_p^{-1}$, and $G_L(z)$ describes the diminishing laser impact on the bunch as a function of the propagation length:

$$G_L(z) = \sqrt{\frac{\pi}{32}} \frac{w_0^2[8 + k_p^2(2r_b^2 + w^2(z))]}{k_p^2(2r_b^2 + w^2(z))^2}, \tag{3.18}$$

which decays on a spatial scale of $z_R \ll k_\beta^{-1}$. The first term in the rhs of the Eq. (3.17) describes proton bunch spreading due to finite transverse emittance ϵ_n, the second through fourth terms describe its focusing/defocusing

by the plasma wakes generated by the leading portion of the bunch (second term), trailing portion of the bunch (third term), and the diffracting laser pulse (fourth term). A similar envelope equation was utilized earlier for proton bunches with a flat-top density transverse distribution [42, 83]. Equation (3.17) is different from the earlier work in two respects. First, it describes the bunch with a transverse profile (Gaussian) which is naturally produced by beam injectors. Second, the effect of a laser pulse on the bunch is described. The latter feature is essential for modeling the laser-seeded MI. As shown below, another feature of the Eq. (3.17) is that it describes the effect of beam density discontinuity at $\zeta = 0$ by proper choice of κ. We also note that equation Eq. (3.17) is formally similar [75] to the one describing the evolution of a Gaussian laser pulse undergoing relativistic self-focusing.

3.3.1 Initial conditions

To understand the evolution of the MI, it is instructive to first examine the equilibrium of the bunch which is self-focused in the plasma. We assume that the beam is in the state of equilibrium if it is completely charge-neutralized by the plasma, i.e. $\delta n_p = \bar{n}_b \equiv n_{b0} \exp\left(-r^2/r_{b0}^2\right)$, where $\bar{n}_b$ and r_{b0} are the equilibrium beam density and radius, respectively. Because the beam's current is not neutralized due to $r_{b0} \ll k_p^{-1}$, the self-magnetic field of the bunch counter-balances its transverse thermal pressure, resulting in the emittance-matched beam with $r_{b0} = \sqrt{2\epsilon_n/\gamma\omega_\beta}$. Any finite deviation $\delta\bar{n}_p = \delta n_p - \bar{n}_b$ from the equilibrium plasma density, or from the equilibrium beam radius,

$\delta r_b = r_b - r_{b0}$, acts as a seed for the MI. Because the evolutions of both r_b and δn_p are governed by second-order differential equations, the finite derivatives $\partial_z r_b$ and $\partial_\zeta \delta n_p$ seed the MI as well. Note that the fully charge-netralized beam at $\zeta = 0$ ($\delta \bar{n}_p = 0$) corresponds to $\kappa = 1$, whereas the hard-cut at $\zeta = 0$ beam ($\delta \bar{n}_p = -\bar{n}_b$), which is out of equilibrium, corresponds to $\kappa = 0$.

Mathematically, the evolution of r_b according to Eq. (3.17) can be described on the $(\zeta > 0, z > 0)$ domain subject to the initial/boundary conditions (IBCs) at the $z = 0/\zeta = 0$ boundaries, respectively. This simplification is justified on the physical grounds as long as (i) the Rayleigh range of the laser satisfies $z_R \ll k_\beta^{-1}$, and (ii) the laser centroid's position satisfies $\zeta_c \ll \sigma_z$, i.e. it is placed sufficiently close to $\zeta = 0$ to justify the assumption of non-evolving leading portion of the bunch. In that limit, the effect of the laser pulse can be modeled as a position-dependent radial velocity kick to the bunch. The resulting radial velocity wave throughout the proton beam does not change r_b substantially (during the laser's time of influence) and can be modeled as an IBC at the $z = 0$ boundary: $\partial_z \delta r_b(\zeta \geq 0, z = 0) = \frac{V_L}{c} \sin[k_p(\zeta - \zeta_c)]$ and $\delta r_b = 0$. The velocity amplitude V_L is calculated by integrating $G_L(z)$ over the propagation distance:

$$\frac{V_L}{\omega_\beta r_{b0}} \approx \frac{\pi^{3/2} q_z^L}{4\sqrt{2}} \frac{n_{p0}}{n_{b0}} \left[a_0^2 k_\beta z_R\right] \left[w_0 \frac{4 + k_p^2(2r_{b0}^2 + w_0^2)}{k_p^2(2r_{b0}^2 + w_0^2)^{3/2}}\right], \tag{3.19}$$

where we have assumed without loss of generality that $k_p \zeta_c = 2\pi M$ (where M is a small integer number). In deriving Eq. (3.19), the aforementioned z integration was simplified by substituting $r_b = r_{b0}$ into the expression for $G_L(z)$. This

I.B.C's	Laser-seed	Hard-cut seed
$\delta r_b(\zeta \geq 0, z = 0)$	0	0
$\frac{\partial \delta r_b}{\partial z}(\zeta \geq 0, z = 0)$	$\frac{V_L}{c}\sin(k_p\zeta)$	0
$\delta \bar{n}_p(\zeta = 0, z \geq 0)$	0	$-\bar{n}_b$
$\frac{\partial \delta \bar{n}_p}{\partial \zeta}(\zeta = 0, z \geq 0)$	0	0

Table 3.1: Initial/boundary conditions (I.B.C's) the laser and hard-cut seeded MI. The non-zero conditions for $\frac{\partial \delta r_b}{\partial z}(\zeta \geq 0, z = 0)$ and $\delta \bar{n}_p(\zeta = 0, z \geq 0)$ each excite the MI for the laser and hard-cut cases, respectively. For a proton beam in equilibrium, all of these I.B.C's are equal to zero.

is justified since the fractional change in the radius $\delta r_b / r_{b0} \sim \frac{V_L z_R}{c r_{b0}} \ll \frac{V_L}{\omega_\beta r_{b0}} \ll 1$ is small during the laser's time of influence for the parameters considered throughout this chapter.

On the other hand, for the hard-cut seeded MI, the non-trivial IBC $\delta \bar{n}_p(\zeta = 0, z \geq 0) = -\bar{n}_b$ (or $\kappa \neq 1$) is established at the head of the proton beam at $\zeta = 0$. A schematic representation of the two seeding approaches is shown in Fig. 3.3. The shaded region of the proton beam in part Fig. 3.3(a) corresponding to the laser-seeded MI represents the leading ($\zeta < 0$) portion of the proton bunch that is unperturbed by the laser and propagates through the plasma in the state of self-focused equilibrium. An instructive mathematical comparison of the IBCs for the two seeding scenarios is summarized in Table 3.1.

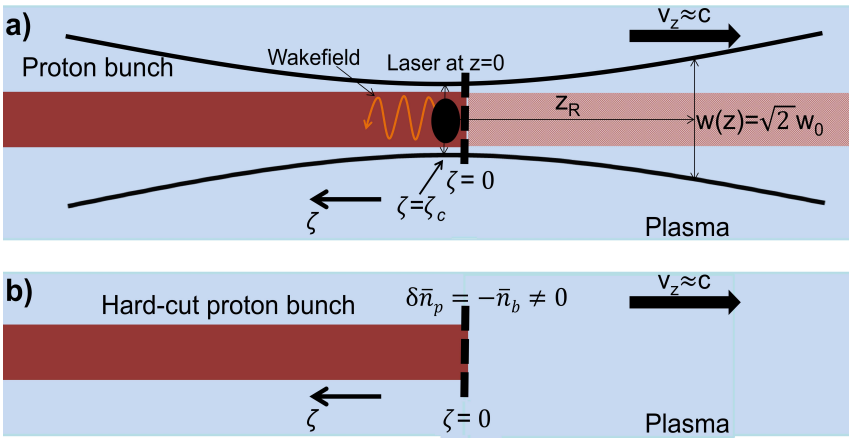

Figure 3.3: Schematic for laser (a) and hard-cut (b) MI seeds in a uniform proton beam for the theory presented in Sec. 3.3. The shaded region of the proton beam in part a) denotes the portion of the beam that is unperturbed and in equilibrium, which extends to $\zeta = -\infty$. Laser is shown in black, proton beam in red, and plasma in blue.

3.3.2 Linear analysis of laser and hard-cut seeded MI

In this section, we analytically describe the linear stage of the MI for both the hard-cut and laser-seeded MI. By absorbing the effect of the laser pulse into the initial condition for $\partial_z r_b(\zeta, z = 0)$ and assuming a matched proton bunch, we recast Eq. (3.17) as

$$\frac{\partial^2 r_b}{\partial z^2} = \frac{k_\beta^2 r_{b0}^4}{4 r_b^3} - \kappa \frac{\cos(k_p \zeta) k_\beta^2 r_{b0}^2}{2} \frac{r_b}{r_{b0}^2 + r_b^2} - \frac{k_p k_\beta^2 r_{b0}^2}{2} \int_0^\zeta d\zeta' \sin[k_p(\zeta - \zeta')] \frac{r_b(\zeta)}{r_b^2(\zeta') + r_b^2(\zeta)}, \tag{3.20}$$

where $\kappa = 1$ ($\kappa = 0$) corresponds to the laser (hard-cut) seeded cases, respectively. Note that the variant of Eq. (3.20) with $\kappa = 0$ modified to account for a flat-top radial density profile considered earlier [42, 83] is strictly valid *only*

for a hard-cut beam with $\lambda(\zeta < 0) \equiv 0$. We further observe that at $z = 0$, Eq. (3.20) becomes $\partial_z^2 r_b = (k_\beta^2 r_{b0}^2/4)(1-\kappa)\cos k_p\zeta$. Therefore, the radial velocity modulation of the beam is seeded by either the laser wake (through the initial condition $\partial_z r_b(\zeta, z = 0) = (V_L/c)\sin k_p\zeta$) for $\kappa = 1$, or by the non-vanishing value of $(1-\kappa)$ for a proton bunch with a finite beam density jump at $\zeta = 0$. Moreover, it follows from the same equation that the leading edge ($\zeta = 0$) of a hard-cut beam expands as if in vacuum because of its finite emittance.

The linearized equation for the perturbed beam is found by Taylor expanding Eq. (3.20) about $r_b = r_{b0}$ to first order in δr_b, yielding

$$\left(\frac{\partial^2}{\partial z^2} + \frac{3k_\beta^2}{4}\right)\delta r_b = \frac{1-\kappa}{4}k_\beta^2 r_{b0}\cos k_p\zeta + \frac{k_p k_\beta^2}{4}\int_0^{\zeta'} d\zeta' \delta r_b(\zeta')\sin k_p(\zeta - \zeta'). \tag{3.21}$$

For a long proton bunch with $\zeta \gg k_p^{-1}$, Eq. (3.21) can be further simplified by assuming a slowly varying beam radius ansatz $\delta r_b = (1/2)r_b^1(\zeta, z)\exp(ik_p\zeta) + c.c$, where $\partial_\zeta r_b^1 \ll k_p r_b^1$. Inserting thus expressed δr_b into Eq. (3.21) yields

$$\frac{\partial^2 r_b^1}{\partial z^2} + \frac{ik_\beta^2 k_p}{8}\int_0^{\zeta} d\zeta' r_b^1(\zeta') = (1-\kappa)\frac{k_\beta^2 r_{b0}}{4}, \tag{3.22}$$

where we have assumed the strongly coupled instability limit of $\partial_z^2 r_b^1 \gg k_\beta^2 r_b^1$. Consistent with the initial conditions given in Table 3.1, Eq. (3.22) is solved with the following initial conditions on r_b^1: (a) $r_b^1(\zeta, z = 0) = 0$, $\partial_z r_b^1(\zeta, z = 0) = -iV_L$, $\kappa = 1$ for the laser-seeded MI, and (b) $r_b^1(\zeta, z = 0) = \partial_z r_b^1(\zeta, z =$

0) = 0, $\kappa = 0$ for the hard-cut seeded MI. Note that in Case (b) the non-vanishing rhs of Eq. (3.22) plays the role of the initial condition.

Using the Laplace transform technique method outlined in Refs. [98, 99], we obtain the asymptotic solutions for $R_1 \equiv \Re(r_b^1 \exp(ik_p\zeta))$ in the long-beam ($k_p\zeta \gg 1$) regime (see Appendix B for a detailed derivation):

$$R_1^{(L)} \approx \frac{3^{7/4}}{8\sqrt{2\pi}} \frac{V_L}{c} \frac{z}{N^{3/2}} e^N \cos\left(k_p\zeta - \frac{N}{\sqrt{3}} + \frac{3\pi}{4}\right) \tag{3.23}$$

for the laser-seeded MI, and the corresponding solution for the hard-cut seeding:

$$R_1^{(HC)} \approx \frac{27 \cdot 3^{1/4}}{128\sqrt{2\pi}} \frac{k_\beta^2 r_{b0} z^2}{N^{5/2}} e^N \cos\left(k_p\zeta - \frac{N}{\sqrt{3}} - \frac{7\pi}{12}\right). \tag{3.24}$$

Here $N = (3\sqrt{3}/4)(k_\beta^2 k_p z^2 \zeta/4)^{1/3}$ is the number of e-foldings of the MI, which is the same for both seeding methods. The asymptotic solutions given by Eqs. (3.23,3.24) are valid in the limit of $1 \ll k_\beta z \ll N \ll k_p\zeta$. The presence of $N(\zeta, z)$ in the expression for the phase of $R_1^{(HC)}$ manifests [83, 84] in the reduction of the phase velocity of the plasma wake produced by the MI. We observe from Eq. (3.23) that the same effect exists when the instability is seeded by the laser pulse.

To compare the effectiveness of the two seeding methods, we calculate the condition for which the amplitude of the laser-seeded radius perturbation $|R_1^{(L)}(\zeta, z)|$ exceeds the radius perturbation $|R_1^{(HC)}(\zeta, z)|$ seeded by the hard-cut proton bunch. The comparison is somewhat complicated by the fact that despite having the same exponential factors, the two seeding approaches have pre-exponential factors that have different spatio-temporal dependencies

on ζ and z. However, a simple estimate of $V_L/\omega_\beta r_{b0} \gtrsim k_\beta z/N$ can be used to find the conditions on the laser intensity required to produce a stronger linear modulation of the beam than in the hard-cut case. We find that this condition is satisfied for typical laser and plasma parameters such as $a_0 = .1$, $w_0 = .28$mm, $n_{p0} = 7 \cdot 10^{14}\text{cm}^{-3}$, $z = k_\beta^{-1} = 4.2$m, and $\zeta = 30$mm. Direct numerical integration of the nonlinear envelope equation given by Eq. (3.17) as well as direct PIC simulations of the proton bunch carried out in Section 3.4 confirm this conclusion.

We also note that the asymptotic spatio-temporal scaling of the pre-exponential factor in the expression for $R_1^{(HC)}(\zeta, z)$ with ζ and z is proportional to $\zeta^{-5/6} z^{1/3}$. Figure 3.4 shows the pre-exponential factor dependence during the linear stage of the instability as analytically calculated from Eq. (3.24) (dashed red lines) and extracted from the numerical solution of Eq. (3.20) (solid blue lines). The figure demonstrates excellent agreement between the analytic and numerical solutions, thus confirming the spatio-temporal scaling of the exponential pre-factor shown in Eq. (3.24). Note that this scaling differs from the one obtained in Ref. [83], where an equation of the same form as Eq. (3.21) (with $\kappa = 0$) was analyzed.

The expressions for $R_1^{(HC)}$ and $R_1^{(L)}$ can now be used to calculate the plasma density perturbation $\delta n_p \approx N_p^{(b)}$ for a developed instability. Assuming that the amplitude of the plasma wave varies slowly on the scale of k_p^{-1}, we express the density perturbation as $\delta n_p = (1/2) p_1 \exp(i k_p \zeta) + c.c.$ and compute p_1 using the expressions for r_b^1 for the two seeding scenarios. After straight-

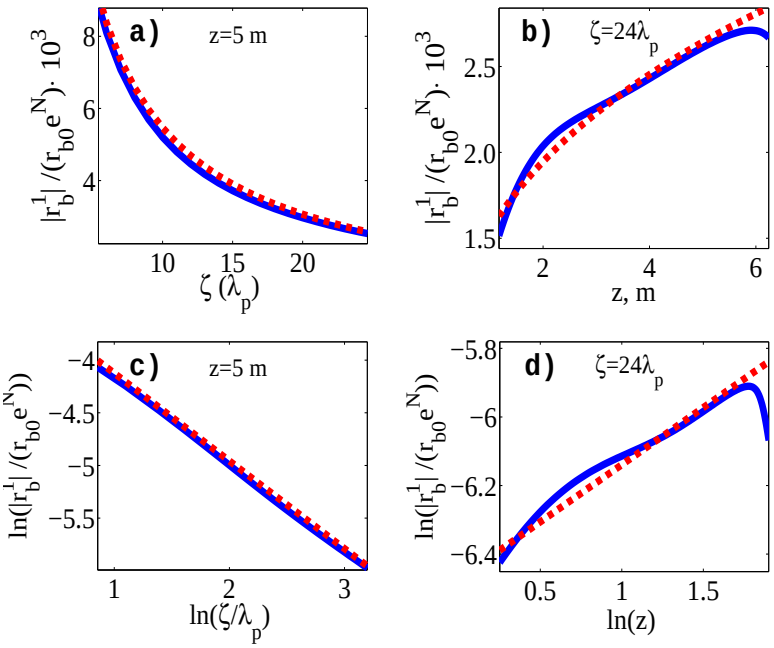

Figure 3.4: Spatio-temporal dependence of the pre-exponent factor during the linear stage of the modulational instability seeded by a hard-cut proton bunch. The pre-exponent factor is plotted on the linear (panels (a), (b)) and logarithmic (panels (c), (d)) scales of the distance $\zeta = ct - z$ from the head of the bunch (panels (a) and (c)) at $z = 5$, and of the propagation distance z (panels (b) and (d)) at the tail end of the bunch at $\zeta = 24\lambda_p$. Dashed red lines: from Eq. (3.24). Solid blue lines: from the numerical solution of Eq. (3.20) with $\kappa = 0$ and the initial conditions at $z = 0$, $r_b(\zeta > 0) = r_{b0}$ and $\partial_z r_b(\zeta > 0) = 0$. Plasma/beam parameters: $k_\beta^{-1} = 4.2$ meters, $k_p^{-1} = .2$mm, and $r_{b0} = 0.1 k_p^{-1}$.

forward algebraic calculations, the following expressions for the plasma wave amplitudes $P_1 \equiv \Re(p_1 \exp(ik_p\zeta))$ are obtained:

$$\begin{aligned} P_1^{(L)} =& \frac{8\sqrt{2}n_{b0}}{3^{5/4}\sqrt{\pi}} \frac{V_L}{\omega_\beta r_{b0}} \frac{N^{1/2}}{k_\beta z} e^N \cos\left(k_p\zeta - \frac{N}{\sqrt{3}} - \frac{7\pi}{12}\right) \\ & \times (1 - r^2/r_{b0}^2) e^{-r^2/r_{b0}^2}, \\ P_1^{(HC)} =& \frac{3^{1/4} n_{b0}}{\sqrt{2\pi}} \frac{1}{\sqrt{N}} e^N \cos\left(k_p\zeta - \frac{N}{\sqrt{3}} + \frac{\pi}{12}\right) \\ & \times (1 - r^2/r_{b0}^2) e^{-r^2/r_{b0}^2}. \end{aligned} \tag{3.25}$$

These expressions for the plasma wave amplitude can now be used for calculating the respective amplitudes of the axial electric field using Eq. (3.5):

$$\begin{aligned} E_z^{(L)} =& \frac{8\sqrt{2\pi} e k_p r_{b0} n_{b0}}{3^{5/4}} \frac{V_L}{\omega_\beta} \frac{N^{1/2}}{k_\beta z} e^N \\ & \times \cos\left(k_p\zeta - \frac{N}{\sqrt{3}} - \frac{13\pi}{12}\right), \\ E_z^{(HC)} =& \frac{3^{1/4}\sqrt{\pi} e k_p n_{b0} r_{b0}^2}{\sqrt{2}} \frac{1}{\sqrt{N}} e^N \\ & \times \cos\left(k_p\zeta - \frac{N}{\sqrt{3}} - \frac{5\pi}{12}\right). \end{aligned} \tag{3.26}$$

3.4 Numerical simulations of the seeded modulation instability

3.4.1 Simulation description

In this Section, numerical simulations that were used to supplement and validate the above theoretical analysis are described. The simulations are carried out using a hybrid particle-in-cell (h-PIC) code analogous to the

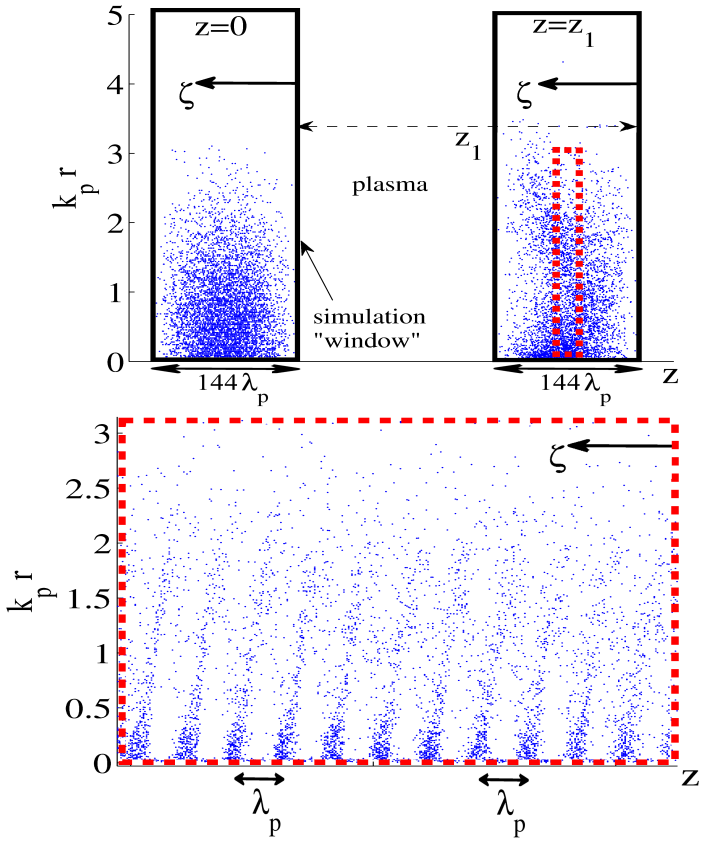

Figure 3.5: Moving "window" geometry of the h-PIC simulation. Blue dots: macro-particles emulating protons of the bunch. Top row, left panel: initial proton distribution in the $0 < \zeta < 144\lambda_p$ window at $z = 0$. Top row, right panel: same for $z = z_1 = 6.3$m. Bottom row: 'zoomed in' view of inset shown in the top row denoted by dashed red lines.

Proton beam parameters	Laser parameters
$r_{b0} = .02\text{mm}$	$w_0 = .28\text{mm}$
$n_{b0}/n_{p0} = 1/500$	$\sigma_z^L = .2\text{mm}$
$\gamma = 479$	$\lambda_L = 10\mu\text{m}$
$k_\beta^{-1} = 4.2\text{m}$	$z_R = 2.5\text{cm}$
$\sigma_\theta = .0024\text{mrad}$	$a_0 = .1$
$\lambda_p = 1.3\text{mm}$	$z_{focal} = 4z_R$
$\zeta_{max} = 24\lambda_p$	$\zeta_c = \lambda_p$

Table 3.2: Proton beam and seeding laser parameters used in h-PIC simulations.

LCODE developed by Lotov [86]. The full set of equations solved by the h-PIC is given in Sec. 3.2. The beam's protons are treated kinetically, plasma ions are assumed immobile, and plasma electrons are described using a single linear quantity, its density perturbation δn_p, which is calculated using Eq. (3.6). For the laser-seeded simulations, the laser is evolved in the presence of the proton beam according to Eq. (3.10). This is in contrast to the theory presented in Sec. 3.3.2 which modeled the effect of the laser pulse as a single impact imparting position-dependent transverse momenta to the protons. The protons' transverse momenta and positions are advanced in the laboratory frame according to Eq. (3.1) inside a computational 'window' co-propagating with the beam with the speed of light. Figure 3.5 shows the macro-particles (in blue) of a PDPWA driver inside the moving computational window at the initial ($z = 0$) and later propagation distances ($z = z_1 = 6.3\text{m}$).

The h-PIC simulations are initialized and advanced in propagation dis-

tance z as follows. At $z = 0$, the beam's macro-particles are given a Maxwellian velocity distribution in the transverse direction with r.m.s velocity equal to $\sigma_\theta c$, and are spatially distributed according to Eq. (3.11) with $r_b = r_{b0} = .1k_p^{-1}$ in every $\zeta > 0$ transverse slice. At each step z, the proton bunch density $n_b(r, \zeta, z)$ is calculated on a 2D grid (r, ζ) according to the chosen weighting function [85] from the numerically obtained positions of the driver's macro-particles. The grid dimensions were $.7k_p^{-1}$ in the radial direction and $150.7k_p^{-1}$ in the ζ-direction, with the grid unit $\Delta\zeta = .2k_p^{-1}$ and $\delta r = .7/256k_p^{-1}$

Thus obtained $n_b(r, \zeta, z)$ is then used to, first, numerically compute δn_p from Eqs. (3.7,3.8,3.9) subjected to the initial condition listed in the Table 3.1 depending on the seeding method, and then to calculate $\psi(\zeta, r, z)$ using Eq. (3.3) in cylindrical geometry. Protons are then advanced in z by the second order leap-frog integration of Eq. (3.1), and the simulation procedure described above is repeated. Approximately 10^5 macro-particles (4 particles per cell) were utilized per given transverse slice.

3.4.2 Comparison between kinetic simulations and envelope equation modeling

In this Section, the results of kinetic h-PIC simulations are described and compared with the predictions of the simplified theory developed in Sec. 3.3 based on the envelope description of the proton bunch. To ensure the consistency of the two approaches, the proton beam parameters used in this Section and listed in Table 3.2 correspond to an emittance-matched beam

with $r_{b0} \ll k_p^{-1}$ (as was assumed in Sec. 3.3). The laser parameters listed in Table 3.2 were chosen to provide an MI seed comparable in strength to the one provided by the hard-cut beam. The magnitude of the laser-generated seed is such that at the beam's tail ($\zeta_{max} = 24\lambda_p$), the velocity modulation amplitude $V_L = .047\omega_\beta r_{b0}$ is much smaller than the transverse thermal velocity of the beam $\sigma_\theta c$. The magnitude of the velocity modulation is in good agreement with the prediction of the impulsive excitation estimate given by Eq. (3.19). The physical parameters of such a laser, corresponding to the power $P \approx 200$ GW, the FWHM duration of $\tau_L \approx 1.6$ ps, and the total energy of $U \approx 0.3$ Joules, are not significantly more ambitious than those of the presently developed [87, 89] short-pulse CO_2 laser systems.

Figure 3.6 displays the amplitude of the proton bunch envelope perturbation $|r_b^1|$ during the linear stage of the MI for the laser (top-row) and hard-cut (bottom-row) seeded cases. The dashed red lines are obtained from Eqs. (3.23,3.24), solid blue lines are obtained by numerically solving the nonlinear envelope equation for the beam's radius given by Eq. (3.20), and the dotted black lines are obtained from the h-PIC simulation. The snapshots of $|r_b^1|(\zeta)$ at $z = 5$m are displayed in panels (a) and (c) for the two seeding methods. Similarly, the evolution of $|r_b^1|(\zeta = 24\lambda_p)$ with the propagation distance z is shown in panels (b) and (d). The modulational instability exhibits a clear spatio-temporal pattern: its amplitude grows towards the tail end of the beam and increases with the propagation distance. Overall, Fig. 3.6 indicates good agreement between the analytic linear model, the nonlinear envelope model,

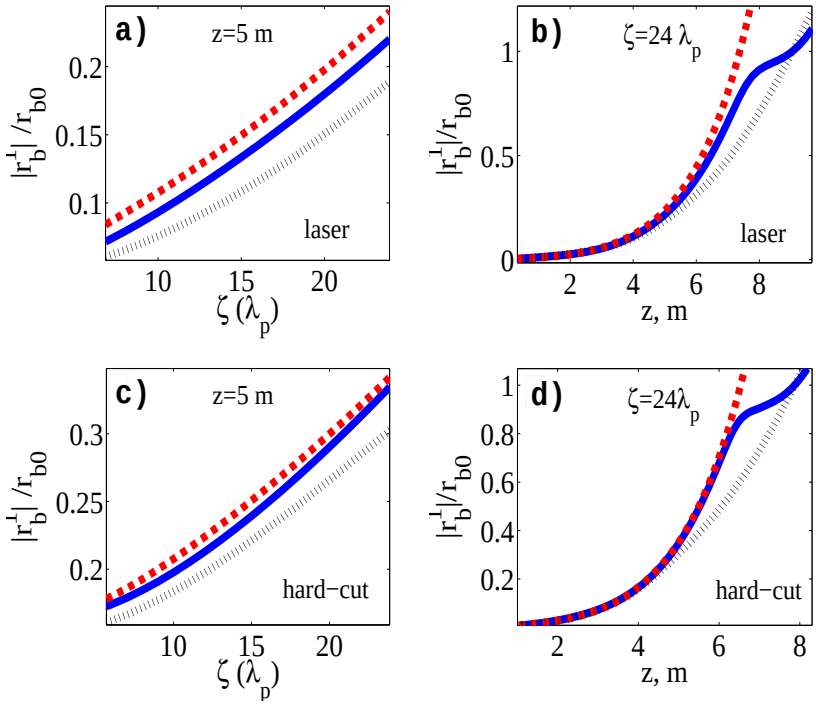

Figure 3.6: Evolution of $|r_b^1|$ according to envelope description and simulations during the linear stage of the laser (top) and hard-cut (bottom) seeded MI. Dashed red lines- Eqs. (3.23) and (3.24). Solid blue lines- solutions to Eq. (3.20) with initial conditions $r_b|_{z=0} = r_{b0} + \delta r_b|_{z=0}$ and $\frac{\partial r_b}{\partial \zeta}|_{z=0} = \frac{\partial \delta r_b}{\partial \zeta}|_{z=0}$, where $\delta r_b|_{z=0}$ and $\frac{\partial \delta r_b}{\partial \zeta}|_{z=0}$ are given in Table 3.1. Dotted black lines- simulated solutions with $\delta \bar{n}_p|_{\zeta=0}$ and $\frac{\partial \delta \bar{n}_p}{\partial \zeta}|_{\zeta=0}$ given in Table 3.1 and initial macro-particle phase-space distribution described in text. System parameters are given in Table 3.2.

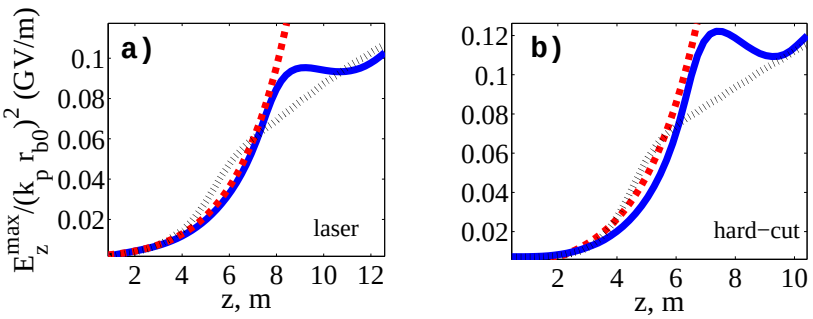

Figure 3.7: Evolution of E_z^{max} vs. z according to envelope description and simulations during the linear stage of the MI for the cases of Fig. 3.6. Parts (a) and (b): laser and hard-cut seeded MI, respectively. Dashed red lines- analytically calculated from Eq. (3.26). Solid blue lines- obtained from Eq. (A.8), where r_b is obtained numerically from Eq. (3.20). Dotted black lines- calculated from simulation. Simulated curves here and in Fig. 3.6 begin once $V_L \approx .047 r_{b0}\omega_\beta$ is achieved throughout the proton beam.

and the full kinetic model. The difference between the envelope solutions and full kinetic simulations is attributed to the fact that the proton beam's transverse shape eventually deviates from its Gaussian shape.

Because the ultimate deliverable of the PDPWA is the accelerating field behind the proton bunch that can be utilized for wakefield acceleration of electrons or positrons, we have computed the electric field inside the proton bunch of finite length $0 < \zeta < 24\lambda_p$. To facilitate the comparison with analytic calculations carried out in Sec. 3.3.2, we have limited the propagation length $z < 7$m to avoid the onset of the strongly nonlinear regime of the modulation instability. The results are plotted in Fig. 3.7.

3.4.3 MI in proton beams with realistic longitudinal density profile

While analytic calculations were considerably simplified by assuming that the longitudinal profile of the proton bunch is flat-top, realistic bunches provided by typical high energy storage rings (such as, for example, a Super Proton Synchrotron at CERN) have a monotonic shape. Below, using h-PIC simulations, we model the laser-seeded MI in a proton beam that has the following density profile [93] prior to entering the plasma region:

$$n_b = \frac{n_{b0}}{2} \exp\left(-r^2/\sigma_r^2\right) \left[1 + \cos\left(\sqrt{\frac{\pi}{2}} \frac{(\zeta - \sigma_z\sqrt{2\pi})}{\sigma_z}\right)\right] \tag{3.27}$$

for $0 < \zeta < 2\sigma_z\sqrt{2\pi}$. Beam parameters, which are closer to those available at CERN's SPS-LHC ring, are listed in Table 3.3. The analytic results derived in Section 3.3 are no longer strictly valid because the ultra-thin beam condition $k_p\sigma_r \ll 1$ is no longer satisfied for the beam parameters given in Table 3.3. However, the kinetic h-PIC simulations do not make the ultra-thin beam assumptions and, therefore, are applicable. As in the previous Section, both laser-seeded and hard-cut seeded modulational instability scenarios illustrated in Fig. 3.1 are modeled.

The simulations presented in this section are performed on the computational domain $\zeta_0 \leq \zeta \leq 2\sqrt{2\pi}\sigma_z$, where ζ_0 is the location of the beam's head. The value of ζ_0 and the boundary conditions at this location depend on the seeding scenario as stated in Table 3.4, where $\hat{n}_p \equiv \delta n_p - \hat{n}_b$ and $\hat{n}_b \equiv n_b(r, \zeta = \zeta_0, z)$. Note that for the hard-cut beam, $\hat{n}_b$ can indeed be a function of the propagation distance z because the leading edge of the bunch

Proton beam parameters		
$\sigma_r = .28$mm	$\sigma_z = 3.7$cm	$\sigma_\theta = .04$mrad
$\gamma = 479$	$k_\beta^{-1} = 4.2$m	$n_{b0}/n_{p0} = 1/500$

Table 3.3: Proton beam parameters (similar to those of the planned PDPWA experiments using CERN's SPS-LHC beam) used for simulating the modulational instability of the bunch with the longitudinal density profile given by Eq. (3.27).

B.C's at ζ_0	Laser-seed	Hard-cut seed
ζ_0	0	$\sqrt{\pi/2}\sigma_r$
$\hat{n}_p(\zeta = \zeta_0, z \geq 0)$	0	$-\hat{n}_b$
$\frac{\partial \hat{n}_p}{\partial \zeta}(\zeta = \zeta_0, z \geq 0)$	0	0

Table 3.4: Boundary conditions (B.C's) for tapered proton beam simulations. Simulations are performed on the domain $\zeta_0 \leq \zeta \leq 2\sigma_z\sqrt{2\pi}$. Terminating the beam at $\zeta_0 = \sigma_z\sqrt{\pi/2}$ was found to maximize E_z^{max} for the hard-cut seed, where the non-zero value of $\delta\hat{n}_p(\zeta = \zeta_0, z \geq 0)$ excites the MI.

is not charge-neutralized and, therefore, expands as it propagates through the plasma. Figure 3.1 shows a schematic representation of the laser/hard-cut seeds for the tapered proton beam, where the vertical dashed lines denote the location of ζ_0.

The choice of ζ_0 is governed by maximizing the amplitude of the plasma wave in the wake of the bunch. Clearly, for the laser-seeded scenario it is advantageous to place the laser pulse immediately in front of the beam head at $\zeta = \zeta_0$ and to choose $\zeta_0 = 0$ in order to maximize the length of the bunch over which the MI develops. The situation is somewhat different for the hard-cut case because the amplitude of the seed would vanish if the beam's head was at $\zeta_0 = 0$. Specifically, the finite value of $\hat{n}_p(\zeta = \zeta_0, z \geq 0) = -n_b(\zeta_0)$ seeds the MI. While the strongest seed for the MI corresponds to $\zeta_0 = \sigma_z\sqrt{2\pi}$ (middle of the bunch), such a choice of the beam's cut-off point would effectively reduce the beam's length by a factor of 2, thereby suppressing the instability. Our calculations indicate that the intermediate choice of $\zeta_0 = \sigma_z\sqrt{\pi/2}$ approximately maximizes E_z^{max} by providing a strong instability seed while maintaining a sufficiently long bunch.

The nonlinear evolution of the peak accelerating field E_z^{max} vs. z modeled by h-PIC simulations is shown in Fig. 3.8(a) for the two scenarios of seeding the MI: using a laser (blue line) and hard-cut proton bunch (dashed black line). For the laser-seeded case, laser parameters from Table 3.2 are used. For clarity, the relatively high but transient values of E_z^{max} produced by the transient plasma wake prior to the laser pulse's diffraction ($z < 2z_{focal}$) are not

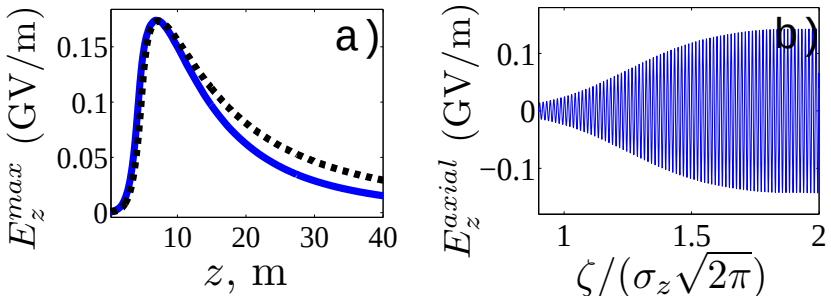

Figure 3.8: Results of h-PIC simulation of laser and hard-cut seeded modulational instability of a realistically shaped proton beam. (a): E_z^{max} vs. z for the hard-cut (dashed black line) and laser-seeded (blue line) MI. (b): Snapshot of $E_z^{axial}(\zeta)$ after $z = 5$m of beam propagation for laser-seeded MI. Proton beam parameters and boundary conditions for the linearized plasma wave: Tables 3.3 and 3.4. Beam's density profile is given by Eq. (3.27). Seeding laser parameters: Table 3.2. Plasma density: $n_{p0} = 7 \cdot 10^{14}\text{cm}^{-3}$.

displayed. The strongest accelerating field is produced towards the tail end of the proton bunch as shown in Fig. 3.8(b), where a snapshot of laser-seeded $E_z^{axial}(\zeta)$ is plotted after $z = 5$m of bunch propagation through the plasma with density $n_{p0} = 7 \cdot 10^{14}\text{cm}^{-3}$. As Fig. 3.8(a) clearly demonstrates, seeding the modulational instability with a modestly intense laser pulse can produce peak accelerating fields of the same magnitude as the hard-cut bunches. The advantage of laser seeding is that no manipulation of the SPS proton bunch aimed at producing a sharp leading edge of the beam is required.

As can be observed from Fig. 3.8(a), the accelerating field of the plasma saturates after several meters of beam propagation and monotonically decreases afterwards regardless of how the modulational instability is seeded. This general behavior has been predicted earlier [93] for a hard-cut proton

bunch with the shape given by Eq. (3.27) and the beam cut-off point at $\zeta_0 = \sigma_z\sqrt{2\pi}$. It was attributed to off-axis scattering of the protons by the plasma wake whose phase velocity is always smaller [83, 84] than the speed of light. The proposed solution [93] is to allow the wake to catch up with the micro-bunched proton beam by introducing a short plasma ramp. An upshift in plasma density decreases the plasma wavelength, which aligns the focusing phase of the wakefield with regions of the proton beam that are tightly focused, providing stable propagation for the tightly focused bunches.

Below we demonstrate that the same approach works for a laser-seeded MI. Specifically, a density ramp placed in the early stages of the laser-seeded MI stabilizes the instability and leads to a quasi-equilibrium for which E_z^{max} of order ~ 100MV/m is sustained over very long propagation distances. Here, we use a linear plasma ramp that starts at $z = L_0$ into the plasma and terminates at $z = L_0 + L_r$. Plasma density inside the ramp is assumed to be linearly increasing with z from the initial value of n_{p0} to the terminal value of $n_{p0} + \delta n_{p0}$. The ramp is represented schematically in Fig. 3.9(a).

The peak accelerating field E_z^{max} is plotted as a function of the propagation distance z for the two seeding scenarios in Fig. 3.9(b) in the presence of the plasma ramp. To maximize the quasi-equilibrium value of E_z^{max}, different ramp parameters (L_0 and L_r given in the figure caption) were used for the hard-cut (dashed black line) and laser-seeded (blue line) scenarios. With the exception of the somewhat larger $\sigma_z = 6.5$ cm bunch length, the same laser and beam parameters were used in the ramped simulation as in the homoge-

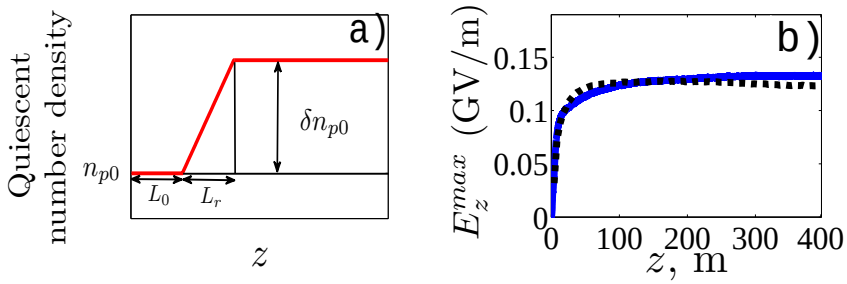

Figure 3.9: Stabilization of the MI using a plasma density ramp for the two seeding scenarios. (a) Schematic of the plasma ramp. (b) Simulated accelerated field E_z^{max} vs. propagation distance z with plasma density ramp for the hard-cut (dashed black line) and laser-seeded (blue line) cases. Laser and proton beam parameters are the same as in Fig. 3.8, except $\sigma_z = 6.5$ cm. For laser (hard-cut) seed, $L_0 = 1.68$m ($L_0 = 1.8$m) and $L_r = 2.2$m ($L_r = 2.6$)m. Initial plasma density is $n_{p0} = 7 \cdot 10^{14}\text{cm}^{-3}$ and $\delta n_{p0} = .038 n_{p0}$ for both seeds.

neous plasma simulation shown in Fig. 3.8. This is done to maximize E_z^{max} because the density ramp leads to lower peak accelerating fields and smaller density perturbations than for the homogeneous plasma [93]. Figure 3.9 clearly demonstrates that the concept of ramp-stabilization of the accelerating field can be applied to the laser-seeded MI as effectively as the earlier considered case of a hard-cut proton bunch, leading to sustained E_z^{max} values over long distances.

3.5 Conclusion

In summary, we have shown that a laser pulse can be used to efficiently seed the MI inside a PDPWA driver. It is found that a 10μm CO_2 laser is required to prevent secondary/tertiary ionization while providing a sufficiently

strong instability seed. The amplitude of the transverse radial velocity wave imparted to the proton beam by the laser's wakefield has been calculated. Using this velocity as an initial condition, the linear stage of the MI was described analytically and compared to the hard-cut seeded MI, and this theory was then compared with simulation results. Using simulations, we then demonstrated that a laser pulse with experimentally achievable parameters produces peak accelerating gradients that are comparable to those produced by a hard-cut seed in a proton beam with a realistic longitudinal density profile. Finally, we have shown that a density ramp placed in the early stages of the laser-seeded MI stabilizes the instability and leads to a quasi-equilibrium for which E_z^{max} values of order $\sim$ 100MV/m are sustained over long distances.

This work was supported by the US DOE grant DE-FG02-12ER41794.

Chapter 4

On the harmonic expansion formalism that attempts to describe the nonlinear stage of the modulation instability

4.1 Introduction and motivation

The initial growth stage of the modulation instability (MI) in a proton driver plasma wakefield accelerator, or 'linear stage', has been studied in Chapter 3 and also in other works [42, 83], and is characterized by exponential growth of the longitudinal accelerating gradient and beam density. Growth during the linear stage occurs until a nonlinear saturation regime is reached in which these quantities cease growing and then begin to decrease. The particle-in-cell (PIC) simulated curves (see Chapter 3 for PIC description) of Fig. 4.1 demonstrate this phenomenon for several different initial r.m.s. beam widths, σ_r. This effect has also been observed in Ref. [93], but a theoretical description of the MI's saturation and subsequent decay is lacking.

The harmonic expansion formalism described here was intended to explain the behaviour of the MI after its linear stage ends, such as the field decay observed in Fig. 4.1. The original idea or thesis was to use the formalism to argue that growth in the proton beam's average r.m.s. radius (zeroth harmonic) during the MI's post-linear stage leads to axial field decay. First, we

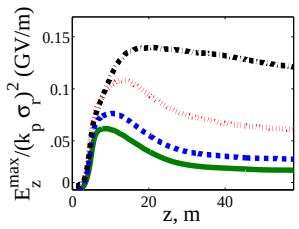

Figure 4.1: Growth, saturation, and decrease of maximal accelerating gradient produced by a PDPWA driver subjected to the modulation instability (MI) for several different initial beam sizes. Solid green, dashed blue, dotted red, and dashed/dotted black curves correspond to $k_p\sigma_r$ values of 1, .7, .35, and .1, respectively, which were calculated using the particle-in-cell (PIC) described in Chapter 3 and the system parameters of Fig. 4.2. This paper describes the nonlinear saturation of these curves and calculates their peak accelerating gradient.

outline the formalism and then highlight several problems with it. Then, we give an example in which a proton beam's zeroth harmonic grows indefinitely but the axial field remains stable, which is in direct contradiction to the thesis and what is suggested by the formalism.

We begin by assuming an ultrarelativistic hard-cut proton beam propagating through a cold plasma with Lorentz factor $\gamma \equiv 1/\sqrt{1-(v_{bz}/c)^2} \gg 1$, where v_{bz} is the beam's longitudinal velocity. For a linear plasma wake, the envelope equation for the beam's r.m.s. radius $r_b(\zeta, z)$ at distance $\zeta \equiv ct - z$ from the beam's head after propagation distance z is (from Chapter 3)

$$\frac{\partial^2 r_b}{\partial z^2} = \frac{k_{\beta 0}^2 \rho_0^4}{4 r_b^3} - \frac{k_p k_{\beta 0}^2 \rho_0^2}{2} \int_0^\zeta d\zeta' \frac{\sin[k_p(\zeta - \zeta')] r_b(\zeta, z)}{r_b^2(\zeta', z) + r_b^2(\zeta, z)}, \tag{4.1}$$

where $\rho_0 \equiv \left(\frac{4\epsilon_n^2}{\gamma^2 \omega_{\beta 0}^2}\right)^{1/4}$ is the radius of an emittance-matched proton beam with normalized emittance ϵ_n, $k_{\beta 0} \equiv c/\omega_{\beta 0}$, $\omega_{\beta 0} \equiv \sqrt{\frac{4\pi e^2 n_{b0}}{\gamma m_p}}$ is the initial betatron

frequency of the proton beam, and m_p is the proton mass. Equation (4.1) has assumed a self-similar Gaussian beam profile

$$n_b = \frac{n_{b0}\rho_0^2 e^{-r^2/r_b^2}}{r_b^2} \tag{4.2}$$

for tractability, is used as a benchmark for the analytical theory presented below, and is similar to the evolution equation given in Ref. [75] that describes a Gaussian laser pulse undergoing relativistic self-focusing. The initial conditions (I.C's) of a hard-cut beam for Eq. (4.1) are $\frac{\partial r_b}{\partial z}(\zeta \geq 0, z = 0) = 0$ and $r_b(\zeta \geq 0, z = 0) = \rho_0$ on $\zeta \geq 0$. It is convenient to rewrite Eq. (4.1) using integration by parts:

$$\begin{aligned}\frac{\partial^2 r_b}{\partial z^2} =& \frac{k_{\beta 0}^2 \rho_0^4}{4}\left(\frac{1}{r_b^3} - \frac{1}{\rho_0^2 r_b}\right) + \frac{k_{\beta 0}^2 \rho_0^2}{2}\cos(k_p\zeta)\frac{r_b(\zeta, z)}{r_b^2(\zeta = 0, z) + r_b^2(\zeta, z)} \\ &+ \frac{k_{\beta 0}^2 \rho_0^2}{2}\int_0^\zeta d\zeta' \cos[k_p(\zeta - \zeta')]\frac{\partial}{\partial \zeta'}\left[\frac{r_b(\zeta, z)}{r_b^2(\zeta', z) + r_b^2(\zeta, z)}\right].\end{aligned} \tag{4.3}$$

The second term of Eq. (4.3) corresponds to the effect of the beam's transverse emittance, the third term represents the beam's response to the plasma wave excited at the hard-cut beam's leading edge, and the fourth term models the effect of the transverse plasma wakefield excited by the beam on itself, providing feedback that results in the MI. With the above I.C's, Eq. (4.3) is

$$\frac{\partial^2 r_b}{\partial z^2} = \frac{k_{\beta 0}^2 \rho_0}{4}\Re(e^{ik_p\zeta})$$

at $z = 0$, thereby seeding the modulation of r_b which subsequently undergoes an exponential growth in (z, ζ) for large propagation distances.

The evolution of the axial accelerating gradient E_z^{ax}, the ultimate deliverable of the PDPWA, is tied closely to that of n_b and r_b through the following expression that is used to compare between different numerical/analytical models (from Chapter 3):

$$E_z^{ax} = 4\pi e k_p^2 \int_0^\infty \int_0^\zeta d\zeta' dr' r' K_0(k_p r') \cos(k_p(\zeta - \zeta')) n_b(\zeta', r', z). \tag{4.4}$$

This expression becomes

$$E_z^{ax} = -e\lambda k_p^2 \int_0^\zeta d\zeta' \cos(k_p(\zeta - \zeta')) e^{k_p^2 r_b^2/4} Ei(k_p^2 r_b^2/4) \tag{4.5}$$

upon insertion of the Gaussian profile Eq. (4.2), where

$$Ei(z) = -\int_{-z}^\infty \frac{e^{-t}}{t} dt. \tag{4.6}$$

Figure 4.2(a) shows a comparison between the beam's r.m.s. at $z = 2/k_{\beta 0}$ as calculated from PIC (solid black), numerical solution to Eq. (4.3) (dotted blue), and $r_b = r_b^0 + |r_b^1| \cos(k_p \zeta + \psi)$ (dotted red) extracted from envelope solution at this bin for which $\psi \approx \pi$. Figure 4.2(b) shows the maximal accelerating gradient using the same line scheme as Fig. 4.2(a). The envelope solution produces a nonphysical structure near the axis, where the presence of higher harmonics is clearly present in this structure, and this type of structure leads to nonphysical 'wiggles' in the maximal electric field plot. The system parameters used are $n_{p0} = 7 \cdot 10^{14}$c.m^{-3}, $k_p^{-1} = .2$ mm, $n_{b0}/n_{p0} = 1/500$, $\gamma = 479$, $k_{\beta 0}^{-1} = 4.2$m, and $k_p \rho_0 = .7$, which are similar to those of the planned PDPWA experiments at CERN's SPS-LHC [81]. As discussed in Ref. [96], the envelope equation disagrees with PIC due to its assumption of constant

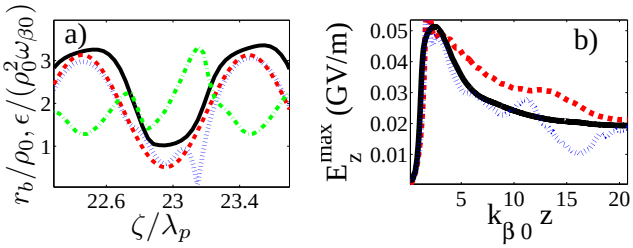

Figure 4.2: Comparison between PIC and numerical solution to envelope equation. (a): $z = 2/k_{\beta 0}$; r.m.s. radius as calculated from PIC (solid black), Eq. (4.3) (dotted blue), and extracted two harmonic solution $r_b = r_b^0 + |r_b^1|\cos(k_p\zeta + \psi)$ (dashed red); beam's emittance is shown in dash-dot green. (b): Maximal electric field using same line scheme as (a). Emittance growth and absence of couplings between higher moments cause envelope description to differ from PIC, leading to nonphysical r_b structure and 'wiggles' in the field behaviour. Two harmonic solution agrees better with PIC, motivating need for a two harmonic description. System parameters: $n_{b0}/n_{p0} = 1/500$, $\gamma = 479$, $k_{\beta 0}^{-1} = 4.2$m, $k_p\rho_0 = .7$, $n_{p0} = 7 \cdot 10^{14}$c.m^{-3}, and $k_p^{-1} = .2$ mm.

emittance $\epsilon = \sqrt{< \vec{x}_\perp^2 >< \vec{v}_\perp^2 > - < \vec{x}_\perp \cdot \vec{v}_\perp >^2}$ and the absence of couplings between higher moments. In support of this, the PIC-calculated emittance (dash-dot green) in Fig. 4.2(a) shows substantial deviation from its initial value of $\epsilon = .5\rho_0^2\omega_{\beta 0}$, especially in more compressed portions of the beam. The two harmonic solution shows better agreement with PIC in Fig. 4.2.

In an attempt to allow for an analytical and more physical description of the MI in its nonlinear stages and avoid the aforementioned shortcomings of the envelope equation, we proceed by extracting coupled equations for the beam's zeroth and first harmonic envelopes from Eq. (4.3).

4.2 Harmonic expansion formalism

The formalism used to compute a) the evolution equations for the beam's zeroth and first harmonic envelopes and b) the expression for the axial field in terms of these envelopes is now described. We begin by noting that Eqs. (4.3, 4.5) contain integrals of the form $Q \equiv \int_0^\zeta d\zeta' G(\zeta, \zeta', z)$ with kernel

$$G(\zeta, \zeta', z) \equiv \cos[k_p(\zeta - \zeta')] F(\tilde{\zeta}, \tilde{\zeta}', z). \tag{4.7}$$

Separating the ζ dependence of r_b and G into the rapidly and slowly varying scales described by the variables $\phi \equiv k_p \zeta$ and $\hat{\zeta}$, respectively, and then Fourier expanding in terms of these variables yields

$$r_b(\hat{\zeta}, z; \phi) = r_b^0 + \sum_{m=-M, m\neq 0}^{m=M} r_b^m(\hat{\zeta}, z) e^{im\phi}/2, \tag{4.8}$$

$$G(\hat{\zeta}, \hat{\zeta}', z; \phi, \phi') = \sum_{m=-M}^{m=M} \sum_{m'=-M'}^{m'=M'} G_{m,m'}(\hat{\zeta}, \hat{\zeta}', z) e^{i(m\phi + m'\phi')}, \tag{4.9}$$

where the sums are taken over the indices/harmonics of interest (e.g. $M, M' = 1$). The envelopes r_b^m and $G_{m,m'}$ are given by

$$\begin{aligned} r_b^m(\hat{\zeta}, z) =& \frac{1}{\pi(\hat{\delta}_{m,0} + 1)} \int_0^{2\pi} d\phi e^{-im\phi} r_b(\hat{\zeta}, z; \phi), \\ G_{m,m'}(\hat{\zeta}, \hat{\zeta}', z) =& \frac{1}{4\pi^2} \int_0^{2\pi} d\phi' \int_0^{2\pi} d\phi e^{-i(m\phi + m'\phi')} G(\hat{\zeta}, \hat{\zeta}', z; \phi, \phi'), \end{aligned} \tag{4.10}$$

where $\hat{\delta}_{m,m'}$ is the Kronecker delta function, and are assumed to satisfy $\partial_{\zeta', \zeta} G_{m,m'} \ll k_p G_{m,m'}$ and $\partial_\zeta r_b^m \ll k_p r_b^m$. The length scale separation and

accompanying equations used above are justified in Appendix C.

The dominant contribution to the integral

$$Q \equiv \int_0^{\zeta} d\zeta' G = \sum_{m=-M}^{m=M} \sum_{m'=-M'}^{m'=M'} \int_0^{\zeta} d\zeta' G_{m,m'}(\hat{\zeta}, \hat{\zeta}', z) e^{i(m\phi + m'\phi')} \tag{4.11}$$

is from the $m' = 0$ terms which is simply

$$Q = \sum_{m=-M}^{m=M} \int_0^{\hat{\zeta}} d\hat{\zeta}' G_{m,0}(\hat{\zeta}, \hat{\zeta}', z) e^{im\phi}. \tag{4.12}$$

To compute the m^{th} harmonic of

$$Q = Q_0(\hat{\zeta}, z) + \frac{1}{2} \sum_{m=-M}^{m=M} Q_m(\hat{\zeta}, z) e^{im\phi}, \tag{4.13}$$

we integrate Eq. (4.13) over $\frac{1}{\pi(\delta_{m,0}+1)} \int_0^{2\pi} d\phi e^{-im\phi}$, yielding

$$Q_m(\hat{\zeta}, \hat{\zeta}', z) \equiv \frac{1}{\pi(\hat{\delta}_{m,0} + 1)} \int_0^{2\pi} d\phi e^{-im\phi} Q(\hat{\zeta}, z; \phi). \tag{4.14}$$

Inserting Eq. (4.12) yields

$$\begin{aligned} Q_m(\hat{\zeta}, \hat{\zeta}', z) \equiv & \frac{1}{\pi(\hat{\delta}_{m,0} + 1)} \sum_{m''=-M}^{m''=M} \int_0^{2\pi} d\phi \int_0^{\hat{\zeta}} d\hat{\zeta}' G_{m'',0}(\hat{\zeta}, \hat{\zeta}', z) e^{i(m''-m)\phi} \\ = & \frac{2}{(\hat{\delta}_{m,0} + 1)} \int_0^{\hat{\zeta}} d\hat{\zeta}' G_{m,0}(\hat{\zeta}, \hat{\zeta}', z) \\ = & \int_0^{\hat{\zeta}} d\hat{\zeta}' R_m(\hat{\zeta}, \hat{\zeta}', z), \end{aligned} \tag{4.15}$$

where

$$R_m(\hat{\zeta}, \hat{\zeta}', z) \equiv \frac{2}{(\hat{\delta}_{m,0} + 1)} G_{m,0}(\hat{\zeta}, \hat{\zeta}', z) \tag{4.16}$$

and $G_{m,0}$ is given by Eq. (4.10) with $m' = 0$. Eq. (4.16) is now used in computing both the evolution equations for r_b^0 and r_b^1 and the axial field in terms of these envelopes.

4.2.1 Derivation of equations for zeroth and first harmonics of r_b

In this section, the evolution equations for the harmonic envelopes of r_b are derived. To accomplish this, we integrate Eq. (4.3) against $\frac{1}{\pi(\delta_{m,0}+1)}\int_0^{2\pi} d\phi e^{-im\phi}$ with r_b written according to Eq. (4.8). The result is the evolution equation

$$\frac{\partial^2 r_b^m}{\partial z^2} = E_m(\hat{\zeta}, z) + I_m(\hat{\zeta}, z) + W_m(\hat{\zeta}, z) \tag{4.17}$$

with terms

$$\frac{\partial^2 r_b^m}{\partial z^2} = \frac{1}{\pi(\delta_{m,0}+1)}\int_0^{2\pi} d\phi e^{-im\phi}\frac{\partial^2 r_b}{\partial z^2}, \tag{4.18}$$

$$E_m(\hat{\zeta}, z) \equiv \frac{k_{\beta 0}^2\rho_0^4}{4\pi(\hat{\delta}_{m,0}+1)}\int_0^{2\pi} d\phi e^{-im\phi}\left(\frac{1}{r_b^3(\hat{\zeta}, z; \phi)} - \frac{1}{\rho_0^2 r_b(\hat{\zeta}, z; \phi)}\right),$$

$$I_m(\hat{\zeta}, z) \equiv \frac{k_{\beta 0}^2\rho_0^2}{2\pi(\hat{\delta}_{m,0}+1)}\int_0^{2\pi} d\phi e^{-im\phi}\frac{\cos(\phi) r_b(\hat{\zeta}, z; \phi)}{r_b^2(\hat{\zeta}=0, z; \phi=0) + r_b^2(\hat{\zeta}, z; \phi)},$$

$$W_m(\hat{\zeta}, \hat{\zeta}', z) \equiv \frac{k_{\beta 0}^2\rho_0^2}{2}\int_0^{\hat{\zeta}} d\hat{\zeta}' R_m(\hat{\zeta}, \hat{\zeta}', z). \tag{4.19}$$

The expression for R_m in Eq. (4.19) is given by Eq. (4.16). The G integral kernel from Sec. 4.2 that is required to compute R_m is

$$G = k_p \cos[\phi - \phi']\frac{\partial}{\partial \phi'}\left[\frac{r_b(\hat{\zeta}, z; \phi)}{r_b^2(\hat{\zeta}', z; \phi') + r_b^2(\hat{\zeta}, z; \phi)}\right] \tag{4.20}$$

in this case.

We now consider the evolution of r_b^0 and r_b^1 only with the I.C's $r_b^0(\hat{\zeta} \geq 0, z=0) = 1$, $\partial_z r_b^0(\hat{\zeta} \geq 0, z=0) = 0$, $r_b^1(\hat{\zeta} \geq 0, z=0) = 0$, $\partial_z r_b^1(\hat{\zeta} \geq 0, z=0) = 0$, which are consistent with the I.C's for Eq. (4.3), and assume all higher

harmonics are zero (corresponding to $m = 0, 1$ in Eq. (4.17)). The kernels

$$R_0(\hat{\zeta}, \hat{\zeta}', z) \equiv \frac{k_{\beta 0}^2 \rho_0^2}{2} G_{0,0}(\hat{\zeta}, \hat{\zeta}', z) \tag{4.21}$$

and

$$R_1(\hat{\zeta}, \hat{\zeta}', z) \equiv k_{\beta 0}^2 \rho_0^2 G_{1,0}(\hat{\zeta}, \hat{\zeta}', z) \tag{4.22}$$

are found by first writing Eq. (4.20) as

$$\begin{aligned} G = & \frac{k_p i}{2}(e^{i(\phi-\phi')} + e^{-i(\phi-\phi')}) \frac{r_b(\hat{\zeta}, z; \phi) r_b(\hat{\zeta}', z; \phi')}{[r_b^2(\hat{\zeta}, z; \phi) + r_b^2(\hat{\zeta}', z; \phi')]^2} \times \\ & (r_b^{1*}(\hat{\zeta}', z) e^{-i\phi'} - r_b^1(\hat{\zeta}', z) e^{i\phi'}) \end{aligned} \tag{4.23}$$

under this truncation. The expressions for $G_{0,0}$ and $G_{1,0}$ are then

$$\begin{aligned} G_{0,0}(\hat{\zeta},\hat{\zeta}', z) = & \frac{1}{4\pi^2} \int_0^{2\pi} d\phi' \int_0^{2\pi} d\phi G(\hat{\zeta}, \hat{\zeta}', z; \phi, \phi') \\ = & \frac{k_p i}{8\pi^2} \int_0^{2\pi} d\phi' \int_0^{2\pi} d\phi \frac{r_b(\hat{\zeta}, z; \phi) r_b(\hat{\zeta}', z; \phi')}{[r_b^2(\hat{\zeta}, z; \phi) + r_b^2(\hat{\zeta}', z; \phi')]^2} \\ & \times [e^{i(\phi-2\phi')} r_b^{1*}(\hat{\zeta}', z) - e^{i\phi} r_b^1(\hat{\zeta}', z) + e^{-i\phi} r_b^{1*}(\hat{\zeta}', z) - e^{i(2\phi'-\phi)} r_b^1(\hat{\zeta}', z)] \end{aligned} \tag{4.24}$$

and

$$\begin{aligned} G_{1,0}(\hat{\zeta}, \hat{\zeta}', z) = & \frac{1}{4\pi^2} \int_0^{2\pi} d\phi' \int_0^{2\pi} d\phi e^{-i\phi} G(\hat{\zeta}, \hat{\zeta}', z; \phi, \phi') \\ = & \frac{k_p i}{8\pi^2} \int_0^{2\pi} d\phi' \int_0^{2\pi} d\phi \frac{r_b(\hat{\zeta}, z; \phi) r_b(\hat{\zeta}', z; \phi')}{[r_b^2(\hat{\zeta}, z; \phi) + r_b^2(\hat{\zeta}', z; \phi')]^2} \\ & \times [r_b^{1*}(\hat{\zeta}', z)(e^{-2i\phi'} + e^{-2i\phi}) - r_b^1(\hat{\zeta}', z) e^{2i(\phi'-\phi)} - r_b^1(\hat{\zeta}', z)]. \end{aligned} \tag{4.25}$$

The terms proportional to $e^{\pm 2i\phi'}$ and/or $e^{\pm 2i\phi}$ typically have negligible contribution due to their rapid oscillation, but during the post-linear stage in which

$|\tilde{r}_b^1| \approx r_b^0$ is achieved throughout much of the beam, these pieces can have some effect. However, for the sake of the discussion below, which argues that lack of analytic tractability after the MI's linear stage inhibits theoretical progress, we do not need to keep these rapidly oscillating terms to get our point across. In fact, if we did keep them, it would only make the argument for lack of analytic tractability stronger. Eqs. (4.24,4.25) are then approximately

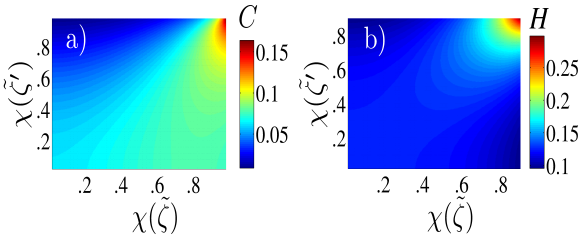

Figure 4.3: The functions $C(\chi(\tilde{\zeta}), \chi(\tilde{\zeta}'), \kappa(\tilde{\zeta}, \tilde{\zeta}'))$ and $H(\chi(\tilde{\zeta}), \chi(\tilde{\zeta}'), \kappa(\tilde{\zeta}, \tilde{\zeta}'))$ displayed over a wide range of inputs as calculated from Eqs. (4.30,4.31) for $\kappa = 1$. Here, $\chi \equiv |r_b^1|/r_b^0$. Typically $C(\kappa = 1) \approx 1/16$ and $H(\kappa = 1) \approx 1/8$. However, for both $\chi(\tilde{\zeta}), \chi(\tilde{\zeta}') \approx 1$, C and H are divergent.

$$G_{0,0}(\hat{\zeta}, \hat{\zeta}', z) \approx \frac{k_p}{4\pi^2} \Im[r_b^1(\hat{\zeta}', z) \int_0^{2\pi} d\phi' \int_0^{2\pi} d\phi e^{i\phi} \frac{r_b(\hat{\zeta}, z; \phi) r_b(\hat{\zeta}', z; \phi')}{[r_b^2(\hat{\zeta}, z; \phi) + r_b^2(\hat{\zeta}', z; \phi')]^2}] \tag{4.26}$$

and

$$G_{1,0}(\hat{\zeta}, \hat{\zeta}', z) \approx -\frac{k_p i r_b^1(\hat{\zeta}', z)}{8\pi^2} \int_0^{2\pi} d\phi' \int_0^{2\pi} d\phi \frac{r_b(\hat{\zeta}, z; \phi) r_b(\hat{\zeta}', z; \phi')}{[r_b^2(\hat{\zeta}, z; \phi) + r_b^2(\hat{\zeta}', z; \phi')]^2}. \tag{4.27}$$

Defining $\tilde{r}_b^m \equiv r_b^m/\rho_0$, $\tilde{R}_m \equiv R_m/(k_p k_{\beta 0}^2 \rho_0)$, $\tilde{\zeta} \equiv k_p \hat{\zeta}$, and $\chi \equiv |r_b^1|/r_b^0$, the corresponding expressions for $\tilde{R}_0$ and $\tilde{R}_1$ are

$$\tilde{R}_0(\tilde{\zeta}, \tilde{\zeta}', z) \approx -\frac{\tilde{r}_b^0(\tilde{\zeta})\chi(\tilde{\zeta}')\chi(\tilde{\zeta})}{(\tilde{r}_b^0(\tilde{\zeta}'))^2} \sin[\psi(\tilde{\zeta}') - \psi(\tilde{\zeta})] C(\chi(\tilde{\zeta}), \chi(\tilde{\zeta}'), \kappa(\tilde{\zeta}, \tilde{\zeta}')) \quad (4.28)$$

and

$$\tilde{R}_1(\tilde{\zeta}, \tilde{\zeta}', z) \approx -ie^{i\psi(\tilde{\zeta}')} \frac{\tilde{r}_b^0(\tilde{\zeta})\chi(\tilde{\zeta}')}{(\tilde{r}_b^0(\tilde{\zeta}'))^2} H(\chi(\tilde{\zeta}), \chi(\tilde{\zeta}'), \kappa(\tilde{\zeta}, \tilde{\zeta}')), \quad (4.29)$$

where ψ is the complex phase of $\tilde{r}_b^1 = |\tilde{r}_b^1| e^{i\psi}$. The expressions for the C and H functions contained in Eqs. (4.28,4.28) are

$$C(\chi(\tilde{\zeta}), \chi(\tilde{\zeta}'), \kappa(\tilde{\zeta}, \tilde{\zeta}')) \equiv$$
$$-\frac{1}{8\pi^2} \int_0^{2\pi} \int_0^{2\pi} d\phi d\phi' \frac{\cos(\phi)(\chi(\tilde{\zeta})^{-1} + \cos(\phi))(1 + \chi(\tilde{\tilde{\zeta}}') \cos(\phi'))}{[\kappa(\tilde{\zeta}, \tilde{\zeta}')^2 (1 + \chi(\tilde{\zeta}) \cos(\phi))^2 + (1 + \chi(\tilde{\zeta}') \cos(\phi'))^2]^2} \quad (4.30)$$

and

$$H(\chi(\tilde{\zeta}), \chi(\tilde{\zeta}'), \kappa(\tilde{\zeta}, \tilde{\zeta}')) \equiv$$
$$\frac{1}{8\pi^2} \int_0^{2\pi} \int_0^{2\pi} d\phi d\phi' \frac{(1 + \chi(\tilde{\zeta}) \cos(\phi))(1 + \chi(\tilde{\zeta}') \cos(\phi'))}{[\kappa(\tilde{\zeta}, \tilde{\zeta}')^2 (1 + \chi(\tilde{\zeta}) \cos(\phi))^2 + (1 + \chi(\tilde{\zeta}') \cos(\phi'))^2]^2}, \quad (4.31)$$

where

$$\kappa(\tilde{\zeta}, \tilde{\zeta}') \equiv \frac{\tilde{r}_b^0(\tilde{\zeta})}{\tilde{r}_b^0(\tilde{\zeta}')}. \quad (4.32)$$

Figure 4.3 displays C and H for $\kappa = 1$ over a wide range of inputs, which shows that typically $C(\kappa = 1) \approx 1/16$ and $H(\kappa = 1) \approx 1/8$. However, for both $\chi(\tilde{\zeta}), \chi(\tilde{\zeta}') \approx 1$, C and H are divergent. Attempts to simplify Eqs.

(4.30,4.31) for $\chi(\tilde{\zeta}), \chi(\tilde{\zeta}') \approx 1$ have been futile, and this is important because as discussed more below, $\chi(\tilde{\zeta}), \chi(\tilde{\zeta}') \approx 1$ is achieved throughout much of the beam after the MI's linear stage. As an example of one of these simplification attempts, we note that Taylor expanding about $\chi(\tilde{\zeta}), \chi(\tilde{\zeta}') = 1$ and assuming small deviations is not possible because of the divergences. Another attempt to simplify Eqs. (4.30,4.31) involved using the technique of evaluation of definite trigonometric integrals via complex analysis [90], but this failed because it requires solving a quartic equation that does not simplify.

It is now convenient to introduce the normalized quantities $\tilde{r}_b \equiv r_b/\rho_0$,

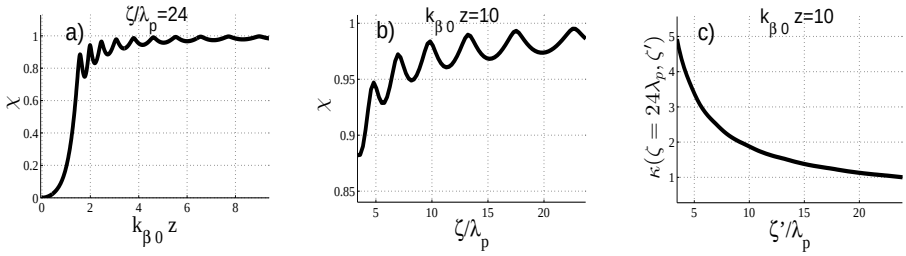

Figure 4.4: Plots of χ and κ during the MI's post-linear stage generated from numerical solutions to Eq. (4.17) with $m = 0, 1$ for the system parameters of Fig. 4.2. The curves show that $\kappa > 1$ and both $\chi(\tilde{\zeta}), \chi(\tilde{\zeta}') \approx 1$ are achieved throughout most of the beam during the post-linear stage. In this nonlinear limit ($\chi(\tilde{\zeta}), \chi(\tilde{\zeta}') \approx 1$), C and H are divergent (see Fig. 4.3) and their expressions do not simplify. Also, the $(1-\chi^2)^{-5/2}$ dependencies in Eqs. (4.33, 4.34) imply strong nonlinearity. Both of these facts hinder analytic progress during the post-linear stage. Even if we could write down analytic expressions for C and H, they would still be divergent for $\chi(\tilde{\zeta}), \chi(\tilde{\zeta}') \approx 1$, and the strong degree of nonlinearity present in Eqs. (4.33, 4.34) makes it very difficult for useful statements to be made.

$\tilde{E}_m \equiv E_m/(k_{\beta 0}^2 \rho_0)$ $\tilde{I}_m \equiv I_m/(k_{\beta 0}^2 \rho_0)$, $\tilde{W}_m \equiv W_m/(k_{\beta 0}^2 \rho_0)$, $\tilde{R}_m \equiv R_m/(k_p k_{\beta 0}^2 \rho_0)$,

and $\tilde{z} \equiv k_{\beta 0} z$. Under Eqs. (4.28,4.29) and the truncation of harmonics with $|m| > 1$ in the expansion of $\tilde{r}_b$, Eq. (4.17) with $m = 0, 1$ is

$$\frac{\partial^2 \tilde{r}_b^0}{\partial \tilde{z}^2} \approx \frac{1}{8(\tilde{r}_b^0)^3} \frac{2 + \chi^2 - 2(\tilde{r}_b^0)^2(1-\chi^2)^2}{(1-\chi^2)^{5/2}} - \tilde{r}_b^0 \chi \int_0^{\tilde{\zeta}} d\tilde{\zeta}' \sin[\psi(\tilde{\zeta}') - \psi(\tilde{\zeta})] \frac{C(\tilde{\zeta}', \tilde{\zeta}) \chi(\tilde{\zeta}')}{(\tilde{r}_b^0(\tilde{\zeta}'))^2}, \tag{4.33}$$

$$\frac{\partial^2 \tilde{r}_b^1}{\partial \tilde{z}^2} \approx \frac{1}{4\tilde{r}_b^0} - \frac{3}{4(\tilde{r}_b^0)^3} \frac{\chi}{(1-\chi^2)^{5/2}} e^{i\psi} - i\tilde{r}_b^0 \int_0^{\tilde{\zeta}} d\tilde{\zeta}' H(\tilde{\zeta}', \tilde{\zeta}) e^{i\psi(\tilde{\zeta}')} \frac{\chi(\tilde{\zeta}')}{(\tilde{r}_b^0(\tilde{\zeta}'))^2}, \tag{4.34}$$

where we have not written the $\tilde{z}$ dependence explicitly for brevity. Eqs. (4.33, 4.34) are not tractable after the MI's linear stage. The main reason for this is that after the linear stage, $\kappa > 1$ and $\chi(\tilde{\zeta}), \chi(\tilde{\zeta}') \approx 1$ are achieved throughout most of the beam, as seen in Fig. 4.4. In this nonlinear limit ($\chi(\tilde{\zeta}), \chi(\tilde{\zeta}') \approx 1$), C and H are divergent (see Fig. 4.3) and their expressions do not simplify. Also, the $(1-\chi^2)^{-5/2}$ dependencies in Eqs. (4.33, 4.34) imply strong nonlinearity. Even if we could write down analytic expressions for C and H, they would still be divergent for $\chi(\tilde{\zeta}), \chi(\tilde{\zeta}') \approx 1$, and the strong degree of nonlinearity present in Eqs. (4.33, 4.34) makes it very difficult for useful statements to be made.

The axial accelerating gradient is calculated within our harmonic expansion formalism next.

4.2.2 Axial field within harmonic expansion framework

In this section, expressions for the harmonic envelopes of the axial field E_z^{ax} are derived from Eq. (4.5), which are then shown to predict nonphysical

results. To determine the m^{th} harmonic of $E_z^{ax} = E_z^0 + \frac{1}{2}\sum_{m=-M}^{m=M} E_z^m(\hat{\zeta}, z)e^{im\phi}$ using Eq. (4.15) from Sec. 4.2, we write

$$E_z^m/(e\lambda k_p^2) = Q_m(\hat{\zeta}, \hat{\zeta}', z) = \int_0^{\hat{\zeta}} d\hat{\zeta}' R_m(\hat{\zeta}, \hat{\zeta}', z), \tag{4.35}$$

where R_m is given by Eq. (4.16). In this case,

$$F = F(\hat{\zeta}', z; \phi') = e^{k_p^2 r_b^2(\hat{\zeta}', z; \phi')/4} Ei(k_p^2 r_b^2(\hat{\zeta}', z; \phi')/4) \tag{4.36}$$

in the function $G = k_p \cos[\phi - \phi']F(\hat{\zeta}', z; \phi')$ from Sec. 4.2 that is required to compute R_m. The corresponding kernels R_0 and R_1 are

$$R_0 = G_{0,0}(\hat{\zeta}, \hat{\zeta}', z) = \frac{1}{4\pi^2}\int_0^{2\pi} d\phi' \int_0^{2\pi} d\phi \cos[\phi - \phi']F(\hat{\zeta}', z; \phi') = 0 \tag{4.37}$$

and

$$\begin{aligned} R_1 = 2G_{1,0}(\hat{\zeta}, \hat{\zeta}', z) &= \frac{1}{2\pi^2}\int_0^{2\pi} d\phi' \int_0^{2\pi} d\phi e^{-i\phi} \cos[\phi - \phi']F(\hat{\zeta}', z; \phi') \\ &= \frac{1}{2\pi}\int_0^{2\pi} d\phi' e^{-i\phi'} F(\hat{\zeta}', z; \phi'). \end{aligned} \tag{4.38}$$

Writing $F = F(r_b(\hat{\zeta}', z; \phi')) = F(r_b^0(\hat{\zeta}', z) + |r_b^1(\hat{\zeta}', z)| \cos(\phi' + \psi(\hat{\zeta}')))$, Eq. (4.38) becomes

$$\begin{aligned} R_1 =& e^{i\psi(\hat{\zeta}')}\frac{1}{2\pi}\int_0^{2\pi} d\phi' e^{-i\phi'} F(r_b^0(\hat{\zeta}', z) + |r_b^1(\hat{\zeta}', z)| \cos(\phi')) \\ =& e^{i\psi(\hat{\zeta}')} Z(\hat{\zeta}', z), \end{aligned} \tag{4.39}$$

where

$$\begin{aligned} Z(\hat{\zeta}', z) \equiv& Z(\chi(\hat{\zeta}', z), k_p r_b^0(\hat{\zeta}', \hat{z})) \equiv \\ & \frac{1}{4\pi}\int_0^{2\pi} d\phi' \cos(\phi') T(k_p r_b^0(\hat{\zeta}', z)(1 + \chi(\hat{\zeta}', z) \cos[\phi'])) \end{aligned} \tag{4.40}$$

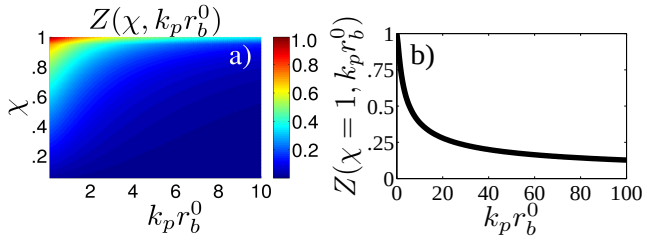

Figure 4.5: Visualization of Z kernel of Eq. (4.41) used to calculate the axial field in terms of beam's harmonic envelopes. (b): lineout of Z vs. $k_p r_b^0$ for $\chi = 1$. Z is a monotonic increasing function in χ with maximum value at $\chi = 1$, and Z is a monotonic decreasing function in $k_p r_b^0$.

and $T(x) = Ei(x^2/4)e^{x^2/4}$. According to Eq. (4.35), the harmonic envelopes of E_z^{ax} are then $E_z^0 = 0$ and

$$E_z^1 = e\lambda k_p^2 \int_0^{\hat{\zeta}} d\hat{\zeta}' e^{i\psi(\hat{\zeta}', z)} Z(\hat{\zeta}', z). \tag{4.41}$$

Figure 4.5(a) shows Z plotted as a function of χ and $k_p r_b^0$ while Fig. 4.5(b) displays a line-out of Z vs. $k_p r_b^0$ at $\chi = 1$. Z is a monotonic increasing function in χ with maximum value at $\chi = 1$, and Z is a monotonic decreasing function in $k_p r_b^0$.

The decay of the Z kernel of Eq. (4.41) with increasing $k_p r_b^0$ implies another serious problem with the harmonic expansion formalism. In short, this is because there are cases in which $k_p r_b^0$ grows to very large values but the maximal accelerating gradient E_z^{max} does not decay and remains stable, which is in direct contradiction to what our formalism predicts. To see an example of this, we first note that it has been reported that the accelerating gradient can be stabilized during the MI's post linear stage by introducing a shift in

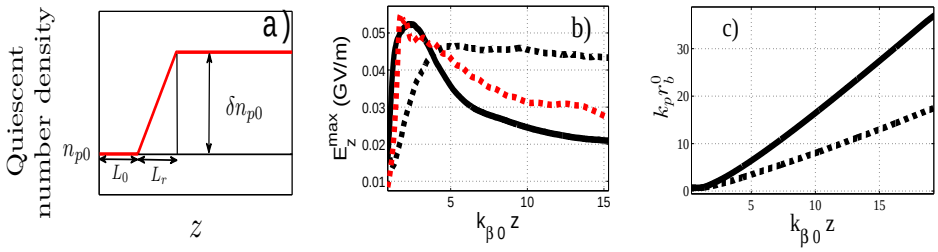

Figure 4.6: Behaviour of maximal accelerating gradient E_z^{max} throughout the MI for the system of Fig. 4.2 with and without the introduction of a shift in background plasma number density (plasma ramp). See text for plasma ramp parameters. Part (a): schematic of plasma ramp. Part (b): PIC-calculated E_z^{max} with (dashed black curve) and without (solid black curve) a plasma ramp; dashed red curve- E_z^{max} without a plasma ramp as calculated from Eq. (4.17) with $m = 0, 1$. Part (c): PIC-calculated growth of $k_p r_b^0$ with (dashed black curve) and without (solid black curve) plasma ramp; growth in $k_p r_b^0$ should cause E_z^{max} to decay regardless of whether or not there is a plasma ramp according to our harmonic expansion formalism (see Fig. 4.5 and Eq. (4.41)), but in fact, E_z^{max} is stable for hundreds of $k_{\beta 0}^{-1}$ beyond what is shown in panel (b) for propagation with a plasma ramp. This a) invalidates the hypothesis that growth in $k_p r_b^0$ is the reason for E_z^{max} to decay, and b) makes the harmonic expansion formalism's ability to explain the MI's post-linear-stage behaviour questionable.

background plasma number density (plasma ramp) during the initial growth stage of the MI [93, 97]. Figure 4.6(a) shows a schematic of a linear plasma ramp. For $k_{\beta 0} L_0 = .9$, $k_{\beta 0} L_r = .26$, and $\delta n_{p0} = .08 n_{p0}$, we observe that the accelerating gradient is stabilized by the plasma ramp for the system of Fig. 4.2 considered thus far, where Fig. 4.6(b) shows the stabilized E_z^{max} curve (dashed black). Figure 4.6(b) also displays E_z^{max} without the plasma ramp as calculated from PIC (solid black) and Eq. (4.17) with $m = 0, 1$ (dashed red). Figure 4.6(c) shows the PIC-calculated growth of $k_p r_b^0$ at $k_p \zeta = 24 \lambda_p$ with

(dashed black) and without (solid black) a plasma ramp- these curves both grow indefinitely for large z. According to our harmonic expansion formalism, the exhibited growth in $k_p r_b^0$ should cause E_z^{max} to decay regardless of whether or not there is a plasma ramp, but in fact, E_z^{max} is stable for hundreds of $k_{\beta 0}^{-1}$ beyond what is shown in Figure 4.6(b) for propagation with a plasma ramp. This observation a) invalidates the hypothesis that growth in $k_p r_b^0$ is the reason for E_z^{max} to decay, and b) makes the harmonic expansion formalism's ability to explain the MI's post-linear-stage behavior questionable.

4.3 Conclusion

In summary, the harmonic expansion formalism fails to explain the post-linear stage behavior of the modulation instability (MI) within a PDPWA driver for two main reasons. The first major problem is the lack of analytic tractability in the evolution equations for the zeroth and first harmonics of r_b after the linear stage of the MI, which overall makes the formalism self-defeating since its intention is to analyze the post-linear stage in an analytic, understandable manner. The second major downfall of the harmonic expansion formalism is that the expression for the axial accelerating gradient calculated within this formalism predicts nonphysical results. Collectively, and arguable individually, these problems are substantial enough to warrant the discontinuation of this work.

Even though the attempt described here was unsuccessful, it is important to note that other approximations and approaches may be able to describe

the nonlinear stage of the modulation instability within a PDPWA driver.

Chapter 5

Conclusion

The propagation of charged particle beams through a background plasma is a rich field. A variety of interesting collective instabilities can arise within the these beams due to feedback between the plasma and beam, which interact via the electromagnetic fields. This thesis focused on the following important beam instabilities: the Weibel Instability (WI) of a relativistic electron beam propagating through a plasma with finite plasma resistivity (FPR) created by electron-ion collisions; and the modulation instability (MI) within a long, ultra relativistic proton bunch.

Chapter 2 has shown that the WI in the presence of FPR enhances beam deceleration at first when compared to a filamentation-suppressed beam (without the WI), but eventually reduces it, so that the net stopping time is essentially unaffected by the WI in the underdense beam limit. This is due to the fact that an electric field is induced before (after) time $t \approx \tau_r/2$ (about halfway through the beam's evolution) by an increasing (decreasing) magnetic field within filaments that acts to enhance (reduce) the deceleration of the filamented beam, respectively. A novel theoretical model has been presented that supports these statements and accurately calculates the dynamics of a filamenting beam during the nonlinear stage of the resistive WI. The model

was used to calculate the net stopping time for the beam in the presence of the resistive WI, which is approximately

$$t_{stop} \approx \gamma(t=0)n_{p0}/(n_{b0}\nu)-$$

about the same stopping time as a filamentation-suppressed beam.

In Chapter 3 we have shown that a laser pulse can be used to efficiently seed the MI in a proton driver plasma wakefield accelerator (PDPWA), which is the first proposed experimentally feasible seeding method. We have found that a 10μm CO_2 laser is required to prevent secondary/tertiary ionization while providing a sufficiently strong instability seed. The amplitude of the transverse radial velocity wave imparted to the proton beam by the laser's wakefield has been calculated. Using this velocity as an initial condition, the linear stage of the MI was described analytically and compared to the hard-cut seeded MI, and this theory was then compared with simulation results. Using simulations, we then demonstrated that a laser pulse with experimentally achievable parameters produces peak accelerating gradients that are comparable to those produced by a hard-cut seed in a proton beam with a realistic longitudinal density profile. Finally, we have shown that a density ramp placed in the early stages of the laser-seeded MI stabilizes the instability and leads to a quasi-equilibrium for which E_z^{max} values of order ~ 100 MV/m are sustained over very long distances.

Chapter 4 has described a harmonic expansion formalism that attempts to explain the post-linear stage behavior of the MI within a PDPWA driver. The formalism was shown to be unsuccessful in its attempt for two main

reasons. The first major problem is the lack of analytic tractability in the evolution equations for the zeroth and first harmonics of r_b after the linear stage of the MI, which overall makes the formalism self-defeating since its intention is to analyze the post-linear stage in an analytic, understandable manner. The second major downfall of the harmonic expansion formalism is that the expression for the axial accelerating gradient calculated within this formalism predicts nonphysical results. Collectively, and arguable individually, these problems are substantial enough to warrant the discontinuation of this work.

It is important to note that other approximations and approaches may be able to explain the the nonlinear stage of the modulation instability within a PDPWA driver, but the attempt described here was unsuccessful.

Appendices

Appendix A

Longitudinal electric field during modulation instability

General expressions for the longitudinal accelerating gradient and its form during the linear stage of the modulation instability (MI) are derived in this section, which requires special treatment for $\sigma_r \ll k_p^{-1}$. In this limit, Eq. (3.3) becomes $\nabla_\perp^2 \psi = S \equiv -4\pi e \delta n_p$. The solution to this equation is given by

$$\psi = \int_0^r dr' r' S(r', \zeta, z) \log(r/r') + F(\zeta, z). \tag{A.1}$$

Note that while determining the radial component $W_r \equiv \partial_r \psi$ of the plasma wake does not require knowledge of the function $F(\zeta, z)$ as expressed by Eq. (3.4), the calculation of $E_z \equiv -\partial_\zeta \psi$ does.

To determine the function $F(\zeta, z)$, which is required to calculate E_z, we match ψ to the solution of the equation $(\nabla_\perp^2 - k_p^2)\psi' = -4\pi e \delta n_p$ in the small k_p limit, where the $k_p^2 \psi'$ term includes the effect of the plasma's return current:

$$\begin{aligned} \psi' = &- \int_0^r dr' r' S(r', \zeta, z) K_0(k_p r) \\ &- \int_r^\infty dr' r' S(r', \zeta, z) K_0(k_p r'). \end{aligned} \tag{A.2}$$

Here, K_0 is the zeroth order modified Bessel function of the second kind. In the limit of small k_p, $K_0(k_p r) \approx -[\gamma' + \ln(k_p r/2)]$, where $\gamma' \approx .577$ is the Euler-Mascheroni constant, and

$$\begin{aligned}\psi' = &\int_0^r dr' r' S(r', \zeta, z) \ln(r) \\ &+ \int_r^\infty dr' r' S(r', \zeta, z) \ln(r') \\ &+ \int_0^\infty dr' r' S(r', \zeta, z)[\gamma' + \ln(k_p/2)]. \end{aligned} \tag{A.3}$$

Inserting

$$\begin{aligned}\int_r^\infty dr' r' S(r', \zeta, z) \ln(r') = &\int_0^\infty dr' r' S(r', \zeta, z) \ln(r') \\ &- \int_0^r dr' r' S(r', \zeta, z) \ln(r') \end{aligned} \tag{A.4}$$

yields

$$\begin{aligned}\psi' = &\int_0^r dr' r' S(r', \zeta, z) \ln(r/r') \\ &+ \int_0^\infty dr' r' S(r', \zeta, z)[\gamma' + \ln(k_p r'/2)]. \end{aligned} \tag{A.5}$$

Matching Eq. (A.1) to Eq. (A.5) gives $F(\zeta, z) = \int_0^\infty dr' r' S(r', \zeta, z)[\gamma' + \ln(k_p r'/2)]$, so that

$$\begin{aligned}\psi = &\int_0^r dr' r' S(r', \zeta, z) \ln(r/r') \\ &+ \int_0^\infty dr' r' S(r', \zeta, z)[\gamma' + \ln(k_p r'/2)]. \end{aligned} \tag{A.6}$$

The axial accelerating gradient $E_z^{axial} \equiv E_z(r = 0)$ is therefore given by

$$E_z^{axial} = 4\pi e \int_0^\infty dr' r' \ln(k_p r') \frac{\partial \delta n_p}{\partial \zeta}, \tag{A.7}$$

where we have neglected $\gamma' - \ln 2 \approx 0.12$ in the integrand in comparison with the $\ln(k_p r')$ term in the relevant limit of $k_p r_b \ll 1$.

To calculate E_z^{axial} for the laser ($\kappa = 1$) and hard-cut ($\kappa = 0$) seeded MI as a function of r_b, we insert $n_p = N_p^{(b)} + N_p^{(i)}$ with $\delta n_p|_{\zeta=0} = \kappa \bar{n}_b$ and $\frac{\partial \delta n_p}{\partial \zeta}|_{\zeta=0} = 0$ into Eq. (A.7), where $N_p^{(b)}$ and $N_p^{(i)}$ are given by Eqs. (3.7) and (3.9), respectively. $N_p^{(L)} = 0$ has been taken for the laser-seeded case since we are only interested in E_z^{axial} after the laser has diffracted away. Integration over r' then yields

$$\begin{aligned} E_z^{axial} = & - e\lambda k_p^2 \int_0^\zeta d\zeta' \cos(k_p(\zeta - \zeta')) \ln(k_p^2 r_b^2/4) \\ & + e\kappa\lambda k_p \sin(k_p\zeta) \ln(k_p^2 r_{b0}^2/4). \end{aligned} \tag{A.8}$$

Appendix B

Calculation of r_b^1 during linear stage for the modulation instability

To demonstrate how r_b^1 is calculated during the linear stage of the modulation instability (MI), we Laplace transform Eq. (3.22) with $\kappa = 1$ (valid for laser-seeded MI) in both ζ and z to k and s, respectively, yielding

$$s^2 k\widehat{r}_b^1 + \frac{iV_L}{2c} = -\frac{ik_p\omega_\beta^2}{8c^2}\widehat{r}_b^1, \tag{B.1}$$

where we have inserted $\frac{\partial r_b^1}{\partial z}(k, z = 0) = -\frac{iV_L}{2ck}$, the Laplace transform in ζ of the initial condition $\frac{\partial r_b^1}{\partial z}(\zeta, z = 0) = -\frac{iV_L}{2c}$. Solving for $\widehat{r}_b^1$ and inverse Laplace transforming yields

$$r_b = \frac{1}{4\pi^2}\int_C\int_{C'} \frac{iV_L e^{sz+k\zeta}}{2c\left[s^2k + ik_p\omega_\beta^2/(8c^2)\right]}dsdk,$$

where C and C' denote the Bromwich contours in s and k, respectively. Applying the residue theorem to this integral in the k coordinate yields

$$r_b^1 = -\frac{1}{4\pi c}\int_C \frac{V_L e^{\phi}}{s^2}ds, \tag{B.2}$$

where $\phi \equiv sz - \frac{ik_p\omega_\beta^2\zeta}{8c^2s^2}$. We now apply the method of steepest descent to compute the integral in Eq. (B.2). The saddle point s_0 is given by the solution

to the equation $\frac{\partial\phi}{\partial s}|_{s=s_0} = 0$ with the largest positive real value, and is given by

$$s_0 = \left[\frac{\sqrt{3}}{2^{5/3}} - \frac{i}{2^{5/3}}\right] \frac{\tilde{\zeta}^{1/3}\omega_\beta^{2/3}}{c^{2/3}z^{1/3}}. \tag{B.3}$$

The second derivative of ϕ at the saddle point is

$$\frac{\partial^2\phi}{\partial s^2}|_{s=s_0} = \left[\frac{3\sqrt{3}}{2^{1/3}} + \frac{3i}{2^{1/3}}\right] \frac{c^{2/3}z^{4/3}}{\omega^{2/3}\tilde{\zeta}^{1/3}}. \tag{B.4}$$

Eq. (B.2) then becomes

$$r_b^1 = -\frac{V_L e^{\phi|_{s=s_0}}}{4\pi c s_0^2} \int_C e^{\frac{1}{2}(s-s_0)^2 \frac{\partial^2\phi}{\partial s^2}|_{s=s_0}} ds,$$

Deforming the contour C so that it passes through $s = s_0$ and exponentially decays away from $s = s_0$ yields

$$r_b^1 = -\frac{V_L e^{\phi|_{s=s_0}}}{4\pi c s_0^2 \sqrt{-\frac{\partial^2\phi}{\partial s^2}|_{s=s_0}}} \int_{-\infty}^{\infty} e^{-\frac{1}{2}t^2} dt = -\frac{V_L e^{\phi|_{s=s_0}}}{2\sqrt{2\pi} c s_0^2 \sqrt{-\frac{\partial^2\phi}{\partial s^2}|_{s=s_0}}}.$$

Inserting Eqs. (B.3) and (B.4) into this equation yields

$$r_b^1 = \sqrt{\frac{1}{6\pi}} \frac{V_L}{\omega_\beta} \frac{1}{\tilde{\zeta}^{1/2}} e^{\frac{3\sqrt{3}}{4^{4/3}}(\tilde{z}^2\tilde{\zeta})^{1/3} - i\frac{3}{4^{4/3}}(\tilde{z}^2\tilde{\zeta})^{1/3} + i\frac{3\pi}{4}}. \tag{B.5}$$

Appendix C

Separation of fast and slow variables used in harmonic expansion formalism

In this appendix, we study the separation of the ζ dependence of quantities into the slow and fast scales described by the variables $\hat{\zeta}$ and ϕ, respectively. First, we assume an arbitrary function of the form $A(r_b(\breve{\zeta}, z, \phi), r_b(\breve{\zeta}', z, \phi'), \phi, \phi')$, where $\breve{\zeta} \equiv \zeta$, $\phi \equiv k_p\zeta$, $\breve{\zeta}' \equiv \zeta'$, and $\phi' \equiv k_p\zeta'$. Fourier expanding A according to

$$A(r_b(\breve{\zeta}, z, \phi), r_b(\breve{\zeta}', z, \phi'), \phi, \phi') = \sum_{m=-M}^{m=M} \sum_{m'=-M'}^{m'=M'} A_{m,m'}(\breve{\zeta}, \breve{\zeta}', z) e^{i(m\phi + m'\phi')} \tag{C.1}$$

and Taylor expanding the right hand side (RHS) only in $\breve{\zeta}, \breve{\zeta}'$ about $\breve{\zeta} = \hat{\zeta}, \breve{\zeta}' = \hat{\zeta}'$ to first order, we arrive at

$$\begin{aligned} A(r_b(\breve{\zeta}, z, \phi), r_b(\breve{\zeta}', z, \phi'), \phi, \phi') = & \sum_{m=-M}^{m=M} \sum_{m'=-M'}^{m'=M'} e^{i(m\phi + m'\phi')} \times \\ & [A_{m,m'}(\hat{\zeta}, \hat{\zeta}', z) + \frac{\partial A_{m,m'}}{\partial \breve{\zeta}}(\hat{\zeta}, \hat{\zeta}', z)\epsilon(\breve{\zeta}, \hat{\zeta}) + \frac{\partial A_{m,m'}}{\partial \breve{\zeta}'}(\hat{\zeta}, \hat{\zeta}', z)\epsilon(\breve{\zeta}', \hat{\zeta}')]. \end{aligned} \tag{C.2}$$

Here,

$$\epsilon(\breve{\zeta}, \hat{\zeta}) \equiv \breve{\zeta} - \hat{\zeta} \tag{C.3}$$

and the sums are taken over the indices/harmonics of interest (e.g. $M, M' = 1$). Integrating Eq. (C.2) against $\frac{k_p^2}{4\pi^2}\int_{\hat{\zeta}}^{\hat{\zeta}+2\pi/k_p}\int_{\hat{\zeta}'}^{\hat{\zeta}'+2\pi/k_p} d\zeta d\zeta' e^{-i(nk_p\zeta+n'k_p\zeta')}$ yields

$$\frac{k_p^2}{4\pi^2}\int_{\hat{\zeta}}^{\hat{\zeta}+\frac{2\pi}{k_p}}\int_{\hat{\zeta}'}^{\hat{\zeta}'+\frac{2\pi}{k_p}} d\zeta d\zeta' e^{-i(nk_p\zeta+n'k_p\zeta')} A(r_b(\breve{\zeta},z,\phi), r_b(\breve{\zeta}',z,\phi'),\phi,\phi') \\ \approx A_{n,n'}(\hat{\zeta},\hat{\zeta}',z) + \frac{1}{2k_p}\frac{\partial A_{n,n'}}{\partial \breve{\zeta}}(\hat{\zeta},\hat{\zeta}',z) + \frac{1}{2k_p}\frac{\partial A_{n,n'}}{\partial \breve{\zeta}'}(\hat{\zeta},\hat{\zeta}',z). \tag{C.4}$$

In writing this we have assumed that M,M' are sufficiently small that higher order contributions from the RHS of Eq. (C.2) are negligible. If the envelopes satisfy

$$\partial_{\breve{\zeta},\breve{\zeta}} A_{n,n'} \ll k_p A_{n,n'} \tag{C.5}$$

so that they are slowly varying in $\breve{\zeta},\breve{\zeta}'$ on the k_p^{-1} scale, then the dominant ordering of Eq. (C.4) is

$$A_{n,n'}(\hat{\zeta},\hat{\zeta}',z) \approx \frac{k_p^2}{4\pi^2}\int_{\hat{\zeta}}^{\hat{\zeta}+\frac{2\pi}{k_p}}\int_{\hat{\zeta}'}^{\hat{\zeta}'+\frac{2\pi}{k_p}} d\zeta d\zeta' e^{-i(nk_p\zeta+n'k_p\zeta')}\times \\ A(r_b(\breve{\zeta},z,\phi), r_b(\breve{\zeta}',z,\phi'),\phi,\phi'). \tag{C.6}$$

Taylor expanding the kernel in the RHS of Eq. (C.6) in $\breve{\zeta},\breve{\zeta}'$ about $\breve{\zeta}=\hat{\zeta},\breve{\zeta}'=\hat{\zeta}'$ to first order results in

$$A(r_b(\breve{\zeta},z,\phi), r_b(\breve{\zeta}',z,\phi'),\phi,\phi') \approx A(r_b(\hat{\zeta},z,\phi), r_b(\hat{\zeta}',z,\phi'),\phi,\phi') \\ + \frac{\partial A}{\partial r_b}\frac{\partial r_b}{\partial \breve{\zeta}}\epsilon(\breve{\zeta},\hat{\zeta}) + \frac{\partial A}{\partial r_b}\frac{\partial r_b}{\partial \breve{\zeta}'}\epsilon(\breve{\zeta}',\hat{\zeta}'). \tag{C.7}$$

Inserting Eq. (C.7) into Eq. (C.6) and assuming $\partial_{\breve{\zeta}} r_b \ll k_p r_b$ allows us to write

$$A_{n,n'}(\hat{\zeta},\hat{\zeta}',z) \approx \frac{1}{4\pi^2}\int_0^{2\pi}\int_0^{2\pi} d\phi d\phi' e^{-i(n\phi+n'\phi')} A(r_b(\hat{\zeta},z;\phi), r_b(\hat{\zeta}',z;\phi');\phi,\phi'), \tag{C.8}$$

where the semi-colons denote independence of the $\hat{\zeta}$ and ϕ variables from each other. For a function

$$B(r_b(\hat{\zeta}, z, \phi), \phi) = B_0(\hat{\zeta}, z) + \sum_{m=-M, m\neq 0}^{m=M} B_m(\hat{\zeta}, z) e^{im\phi}/2 \tag{C.9}$$

without the primed spatial dependence, the analogous expression to Eq. (C.8) is

$$B_n(\hat{\zeta}, z) \approx \frac{1}{\pi(\hat{\delta}_{n,0} + 1)} \int_0^{\phi} d\phi e^{-in\phi} B(r_b(\hat{\zeta}, z, \phi), \phi). \tag{C.10}$$

$\hat{\delta}_{n,n'}$ is the Kronecker delta function in Eq. (C.10).

Equations (C.8,C.10) imply that the slow and fast variables $\hat{\zeta}$ ($\hat{\zeta}'$) and ϕ (ϕ') can be separated from each other under integration/differentiaion in ζ (ζ'), respectively, so that they are effectively independent of each other. The approach is valid if the harmonic envelopes of A, B, and r_b are slowly varying functions in ζ compared to the scale $\sim k_p^{-1}$.

Bibliography

[1] M. V. Medvedev and A. Loeb, Astrophys. J. **526,** 697 (1999).

[2] A. Gruzinov, Astrophys. J. Lett. **563,** L15 (2001).

[3] R. Schlickeiser and P. K. Shukla, Astrophys. J. Lett. **599,** L57 (2003).

[4] T. Kwan, J. M. Dawson, and A. T. Lin , Phys. Fluids **20,** 581 (1977).

[5] B. Chen *et al.* Astrophys. J. Lett. **763,** L21 (2013).

[6] R. C. Arnold and J. Meyer-ter-Vehn, *Rep. Prog. Phys.* **50,** 559 (1987).

[7] J. H. Nuckolls, *Laser Interaction and Related Plasma Phenomena*, edited by G. H. Miley and H. Hora (Plenum, New York, 1992), Vol. 10, pp. 23-24

[8] M.D. Perry and G. Mourou, Science **264,** 917 (1994); D. Strickland and G. Mourou, Opt. Commun. **56,** 219 (1985).

[9] M. Tabak, J. Hammer *et al.* Phys. Plasmas **1,** 1626 (1994).

[10] L. D. Landau and E. M. Lifschitz, *Electrodynamics of Continuous Media* (Pergamon Press, Oxford, 1960) Chap. 7.

[11] K.V. Starikov, C. Deutsch, Phys. Rev. E. **71,** 026407 (2005).

[12] D. A. Hammer and N. Rostoker, Phys. Fluids **13,** 1831 (1970).

[13] Ya. B. Fainberg, V. D. Shapiro, and V. I. Shevchenko, Sov. Phys. JETP 30, 528 1970 Zh. Eksp. Teor. Fiz. **57,** 966 (1969).

[14] M. Lampe and lP. Sprangle, Phys. Fluids **18,** 475 (1975).

[15] M. E. Dieckmann, B. Eliasson, P. K. Shukla, N. J. Sircombe, and R. O. Dendy, Plasma Phys. Controlled Fusion **48,** B303 (2006).

[16] E. W. Weibel, Phys. Rev. Lett. **2,** 83 (1959).

[17] R. L. Morse and C. W. Nielson, Phys. Fluids **14,** 830 (1971).

[18] R. Lee and M. Lampe, Phys. Rev. Lett. **31,** 1390 (1973).

[19] R. C. Davidson, D. A. Hammer, I. Haber, and C. E. Wagner, Phys. Fluids **15,** 317 (1972).

[20] T. Tajima and J. M. Dawson. Phys. Rev. Lett., **43,** 267 (1979).

[21] L. Tonks and I. Langmuir. Phys. Rev., **33,** 195 (1929).

[22] S. Karsch, J. Osterhoff, and A. Popp *et al.* Nature Phys., **9,** 415 (2007); N. A. Hafz, T. M. Jeong, and I. Choi *et al.* Nature Photonics, **2,** 571 (2008); J. Osterhoff, A. Popp, and Zs. Major *et al.* Phys. Rev. Lett., **101,** 085002 (2008).

[23] W. Leemans, B. Nagler, A. Gonsalves, C. Toth, K. Nakamura, C. Geddes, E. Esarey, C. Schroeder, and S. Hooker, Nature Phys. **2,** 696 (2006).

[24] S. Kneip, S. Nagel, S. Martins, S. Mangles, C. Bellei, O. Chekhlov, R. Clarke, N. Delerue, E. Divall, G. Doucas, K. Ertel, F. Fiuza, R. Fonseca, P. Foster, S. Hawkes, C. Hooker, K. Krushelnick, W. Mori, C. Palmer, K. Phuoc, P. Rajeev, J. Schreiber, M. Streeter, D. Urner, J. Vieira, L. Silva, and Z. Najmudin, Phys. Rev. Lett. **103,** 035002 (2009).

[25] X. Wang, R. Zgadzaj, N. Fazel, Z. Li, S. Yi, X. Zhang, W. Henderson, Y. Chang, R. Korzekwa, H. Tsai, C. Pai, H. Quevedo, G. Dyer, E. Gaul, M. Martinez, A. Bernstein, T. Borger, M. Spinks, M. Donovan, V. Khudik, G. Shvets, T. Ditmire, and M. Downer, Nature Comms., doi:10.1038/ncomms2988 (2012).

[26] Joshi, C. *et al.* Phys. Rev. Lett. **47,** 1285 (1981); Kitigawa, Y. *et al.* Phys. Rev. Lett. **68,** 48 (1992); Nakajima, K. *et al.* in *Advanced Accelerator Concepts, AIP Conference Proceedings* **335,** 145 (AIP Press, 1995).

[27] P. Chen, J. Dawson, R. Huff, and T. Katsouleas, Phys. Rev. Lett. **54,** 693 (1985).

[28] M. Hogan, C. Barnes, C. Clayton, F. Decker, S. Deng, P. Emma, C. Huang, R. Iverson, D. Johnson, C. Joshi, T. Katsouleas, P. Krejcik, W. Lu, K. Marsh, W. Mori, P. Muggli, C. O'Connell, E. Oz, R. Siemann, and D. Walz, Phys. Rev. Lett. **95,** 054802 (2005).

[29] M. J. Hogan, T. O. Raubenheimer, A. Seryi, P. Muggli, T. Katsouleas,

C. Huang, W. Lu, W. An, K. A. Marsh, W. B. Mori, C. E. Clayton, and C. Joshi, *New J. Phys.* **12,** 055030 (2010).

[30] P. Muggli, B. Blue, C. Clayton, S. Deng, F. Decker, M. Hogan, C. Huang, R. Iverson, C. Joshi, T. Katsouleas, S. Lee, W. Lu, K. Marsh, W. Mori, C. O'Connell, P. Raimondi, R. Siemann, and D. Walz, Phys. Rev. Lett. **93,** 014802 (2004).

[31] S. Lee *et al.* Phys. Rev. E **64,** 045501 (2001); C. T. Zhou *et al.* Phys. Plasmas **13,** 092109 (2006); Hogan, M. J. *et al.* Phys. Rev. Lett. **90,** 205002 (2003). Blue, B. E. *et al.* Phys. Rev. Lett. **90,** 214801 (2003).

[32] D. Pritzkau and R. Siemann, Phys. Rev. ST Accel. Beams **5,** 112002 (2002).

[33] H. Braun *et al.* Phys. Rev. Lett. **90,** 224801 (2003).

[34] A. Caldwell, K. Lotov, A. Pukhov, and F. Simon, Nature Phys. **5,** 363 (2009).

[35] K. Lotov, Phys. Rev. ST Accel. Beams **13,** 041301 (2010).

[36] B. K. Vainshtein. *Acta Crystallogr. B*, **47,** 145 (1991).

[37] K. R. Hogstrom and P. R. Almond. Phys. Med. Biol., 51, R455 (2006). D. Doria *et al. AIP Advances*, **2,** 011209 (2012).

[38] R. Ruth, A. Chao, P. Morton, ad P. Wilson, Part. Accel. **17,** 171-189 (1985).

[39] I. Blumenfeld, C. Clayton, F. Decker, M. Hogan, C. Huang, R. Ischebeck, R. Iverson, C. Joshi, T. Katsouleas, N. Kirby, W. Lu, K. Marsh, W. Mori, P. Muggli, E. Oz, R. Siemann, D. Walz, and M. Zhou, Nature (London) **445,** 741 (2007).

[40] W. Lu *et al.* Phys. Plasmas **12,** 063101 (2005).

[41] K. Lotov, Proceedings of the 6^{th} European Particle Acclerator Conf., Stockholm, Sweden, 1998, pp. $806 - 808$.

[42] N. Kumar, A. Pukhov, K. Lotov, Phys. Rev. Lett. **104,** 255003 (2010).

[43] D. Whittum, W. Sharp, S. Yu, M. Lampe, and G. Joyce, Phys. Rev. Lett. **67,** 991 (1991).

[44] D. Whittum, Phys. Fluids B **5,** 4432 (1993).

[45] J. Krall and G. Joyce, Phys. Plasmas **2,** 1326 (1995).

[46] Oleg Polomarov, Adam B. Sefkow and Igor Kaganovich, Gennady Shvets, Phys. Plasmas **14,** 043103 (2007).

[47] W. L. Kruer. *The Physics of Laser Plasma Interactions.* Addison-Wesley, Redwood City, (1988).

[48] I. D. Kaganovich, G. Shvets, E. Startsev, and R. C. Davidson, Phys. Plasmas **8,** 4180 (2001).

[49] R. Keinigs and M. Jones, Phys. Fluids **30,** 252 (1987).

[50] J. Meyer-ter-Vehn, Plasma Phys. Controlled Fusion **43,** A113 (2001).

[51] L. O. Silva, R. A. Fonseca, J. W. Tonge, W. B. Mori, and J. M. Dawson, Phys. Plasmas **9,** 2458 (2002).

[52] L. O. Silva, R. A. Fonseca, J. W. Tonge, W. B. Mori, and J. M. Dawson, Phys. Plasmas **10,** 1979 (2003).

[53] E. A. Startsev and R. C. Davidson, Phys. Plasmas **10,** 4829 (2003).

[54] A. Karmakar, N. Kumar, G. Shvets, O. Polomarov, and A. Pukhov, Phys. Rev. Lett. **101,** 255001 (2008)

[55] T. Taguchi, T. M. Antonsen, Jr., C. S. Liu, and K. Mima, Phys. Rev. Lett. **86,** 5055 (2001).

[56] E. V. Belova, R. C. Davidson, H. Ji, and M. Jamada, Phys. Plasmas **11,** 2523 (2004).

[57] L. Gremillet, G. Bonnaud, and F. Amiranoff, Phys. Plasmas **9,** 941 (2002).

[58] C. K. Birdsall and A. B. Langdon, *Plasma Physics via Computer Simulations* (McGraw-Hill, New York, 1981).

[59] T. Okada, I. Sajiki, and K. Satou, Laser Part. Beams **17,** 515 (1999).

[60] A. Pukhov, Z. M. Sheng, and J. Meyer-ter-Vehn, Phys. Plasmas **6,** 2847(1999).

[61] M. V. Goldman, F. Crary, D. L. Newman, and M. Oppenheim, Phys.Plasmas **7,** 1732 (2000).

[62] M. Honda, J. Meyer-ter-Vehn, and A. Pukhov, Phys. Plasmas **7,** 1302(2000).

[63] J. M. Hill, M. H. Key, S. P. Hatchet, R. R. Freeman, Phys. Plasmas **12,** 082304 (2005).

[64] J. J. Honrubia and J. Meyer-ter-Vehn, Nucl. Fusion **46,** L25L28 (2006).

[65] J. P. Freidberg and T. P. Armstrong, Phys. Fluids **11,** 2669 (1968).

[66] R. C. Davidson, *Physics of Nonneutral Plasmas* (World Scientific, London, 2001).

[67] A. Bret, M.-C. Firpo, and C. Deutsch, Phys. Rev. Lett. **94,** 115002 (2005).

[68] G. Shvets, O. Polomarov, V. Khudik, C. Siemon, I. Kaganovich, Phys. Plasmas **16,** 05603 (2009).

[69] E. M. Lifshitz and L. P. Pitaevskii: *Physical Kinetics* (Pergamon Press, Oxford, 1981) Chap.4.

[70] J. Faure, Y. Glinec, A. Pukhov, S. Kiselev, S. Gordienko, E. Lefebvre, J. Rousseau, F. Burgy, and V. Malka, Nature (London) **431,** 541 (2004).

[71] C. Geddes, C. Toth, J. van Tilborg, E. Esarey, C. Schroeder, D. Bruhwiler, C. Nieter, J. Cary, and W. Leemans, Nature (London) **431,** 538 (2004).

[72] S. Mangles, C. Murphy, Z. Najmudin, A. Thomas, J. Collier, A. Dangor, E. Divall, P. Foster, J. Gallacher, C. Hooker, D. Jaroszynski, A. Langley, W. Mori, P. Norreys, F. Tsung, R. Viskup, B. Walton, and K. Krushelnick, Nature (London) **431,** 535 (2004).

[73] M. Hogan, R. Assmann, F. Decker, R. Iverson, P. Raimondi, S. Rokni, R. Siemann, D. Walz, D. Whittum, B. Blue, C. Clayton, E. Dodd, R. Hemker, C. Joshi, K. Marsh, W. Mori, S. Wang, T. Katsouleas, S. Lee, P. Muggli, P. Catravas, S. Chattopadhyay, E. Esarey, and W. Leemans, Phys. Plasmas, **7,** 2241 (2000).

[74] E. Gschwendtner, C. Bracco, B. Goddard, M. Meddahi, A. Pardons, E. Shaposhnikova, H. Timko, F. Velotti, and H. Vincke, Proceedings of the International Particle Accelerator Conference (IPAC'13/ACFA), Shanghai, 2013, pp. 1253 – 1255.

[75] E. Esarey, J. Krall, and P. Sprangle, Phys. Rev. Lett. **72,** 18 (1994).

[76] P. Muggli, V. Yakimenko, M. Babzien, E. Kallos, and K. Kusche, Phys. Rev. Lett. **101,** 054801 (2008).

[77] S. Hillenbrand, R. Assmann, F. Zimmermann, A. Müller, T. Tückmantel, Proceedings of the International Particle Accelerator Conference (IPAC'11/ACFA), San Sebastián, 2011, pp. 2835 – 2837.

[78] S. Yi, V. Khudik, C. Siemon, and G. Shvets, Phys. Plasmas **20,** 013108 (2013).

[79] T. Antonsen, Jr. and P. Mora, Phys. Rev. Lett. **69,** 2204 (1992).

[80] T. Antonsen, Jr. and P. Mora, Phys. Fluids B **5,** 1440 (1993).

[81] G. Xia, R. Assmann, R. Fonseca, C. Huang, W. Mori, L. Silva, J. Vieira , F. Zimmermann, and P. Muggli, J. Plasma Phy., doi:10.1017/S0022377812000086 (2012).

[82] G. Xia, A. Caldwell, K. Lotov, A. Pukhov, R. Assmann, and F. Zimmermann, Proceedings of the International Particle Accelerator Conference (IPAC'10/ACFA), Kyoto, 2010, pp. 4392 – 4394.

[83] C. Schroeder, C. Benedetti, E. Esarey, F. Gruner, and W. Leemans, Phys. Rev. Lett. **107,** 145002 (2011).

[84] A. Pukhov, N. Kumar, T. Tckmantel, A. Upadhyay, K. Lotov, P. Muggli, V. Khudik, C. Siemon, and G. Shvets, Phys. Rev. Lett. **107,** 145003 (2011).

[85] C. Birdsall and A. Langdon, *Plasma Physics via Computer Simulations* (McGraw-Hill, New York, 1981).

[86] K. Lotov, Phys. Plasmas **5,** 785 (1998).

[87] D. Haberberger, S. Tochitsky, and C. Joshi, Opt. Express **18,** 17 (2010).

[88] M. Polyanskiy, I. Pogorelsky, and V. Yakimenko, Opt. Express **19,** 7717 (2011).

[89] I. Pogorelsky, M. Babzien, K. Kusche, I. Pavlishin, V. Yakimenko, C. Dilley, S. Gottschalk, W. Kimura, T. Katsouleas, P. Muggli, E. Kallos, L. Steinhauer, A. Zigler, N. Andreev, D. Cline, and F. Zhou, Laser Physics **16,** 2 (2006).

[90] George B. Arfken , Hans J. Weber, and Frank E. Harris. *Mathematical Methods for Physicists, Seventh Edition: A Comprehensive Guide.* New York: Academic Press, 2012.

[91] M. Ammosov, N. Delone, and V. Krainov, Sov. Phys. JETP **64,** 6 (1970).

[92] E. Lee and R. Cooper, Part. Accel. **7,** 83 (1976).

[93] K. Lotov, Phys. Plasmas, **18,** 024501 (2011).

[94] E. Esarey, P. Sprangle, M. Pilloff, and J. Krall, J. Opt. Soc. Am. B **12,** 9 (1995).

[95] C. Schroeder, C. Benedetti, E. Esarey, F. Grüner, and W. Leemans, Phys. Plasmas, **19,** 010703 (2012).

[96] E. Backhaus, J. Wurtele, Phys. Plasmas **7,** 4729 (2000).

[97] C. Siemon, V. Khudik, S. A. Yi, A. Pukhov, and G. Shvets, Phys. Plasmas **20,** 103111 (2013).

[98] R. Bonifacio, C. Maroli, and N. Piovella, Optics Communications **68,** 5 (1988).

[99] G. Moore, Nucl. Instr. and Meth. **A239** (1985) 19.